

# **Single optical microfibre-based modal interferometer**

## **Dissertation**

zur  
Erlangung des Doktorgrades (Dr. rer. nat.)  
der  
Mathematisch-Naturwissenschaftlichen Fakultät  
der  
Rheinischen Friedrich-Wilhelms-Universität Bonn

vorgelegt von

**Konstantin Karapetyan**

aus  
Moskau

Bonn 2012



Angefertigt mit Genehmigung  
der Mathematisch-Naturwissenschaftlichen Fakultät  
der Rheinischen Friedrich-Wilhelms-Universität Bonn

1. Gutachter: Prof. Dr. Dieter Meschede  
2. Gutachter: Prof. Dr. Stephan Schlemmer

Tag der Promotion: 18. Oktober 2012

Erscheinungsjahr: 2012



# Abstract

In this thesis, I report on the experimental investigation and the computer simulation of optical microfibre-based modal interferometers. An optical microfibre (OMF) can be produced from a commercial single-mode optical fibre by a tapering process consisting in simultaneous heating and pulling the fibre. OMFs have attracted much attention in the recent years due to high light concentration, a strong evanescent field around the OMF waist, and convenience of use thanks to their fibre-coupled nature. It makes them a promising element for both basic research and sensing applications.

Interferometers based on OMFs extend possible application areas to dispersive sensing. In a single-OMF modal interferometer (SOMMI), the two interferometer arms share the same path, and interference occurs between two transverse modes excited in the down-taper and recombined in the up-taper.

During my work, I have produced OMF samples, characterized them, and used them as SOMMIs. To verify the OMF shape, different approaches have been implemented, including a light scattering method and a newly developed optical harmonic generation-based diameter measurement method [1]. For actual verification of the SOMMI performance, a simple post-production procedure, based on the stretch-interferometry, was realized. In this stretch-test, the experimental samples showed high contrast and very good signal-to-noise ratio making them suitable for sensing applications. Additionally, they were tested using spectral interferometry in air.

Furthermore, I have designed and produced SOMMI samples specifically for interferometry in liquids and tested them as a refractive index sensor. Exhibiting a characteristic achromatic fringe, SOMMIs are a promising tool for the absolute refractive index measurement. In this experiment, a sensitivity of 3000 to 4000 nm per refractive index unit was measured. This is the highest sensitivity observed in non-birefringent OMF-based sensors so far.

I have also developed a computer model of OMFs and SOMMIs. While the calculation methods for light propagation simulation in usual optical fibres are well established, simulation of OMFs demands many questions to be answered. The main challenge here is the calculation of the taper regions, where the fibre diameter varies from the standard diameter of a commercial fibre of 125 µm to the diameter of the OMF waist of several hundred nanometres. Together with the diameter, the light-guidance regime changes from the weak guidance in the

untapered fibre to the strong guidance in the waist, requiring different models to be combined. To the best of my knowledge, I have created the first reliably working software code for automatic calculation of all guided modes supported by tapered fibres [2]. I have then used this code to create computer models for stretch- and spectral-interference in SOMMIs. The experimental results confirm the validity of these models.

Some results reported in this thesis have been published as:

1. Wiedemann, U., Karapetyan, K., Dan, C., Pritzkau, D., Alt, W., Irsen, S. & Meschede, D. Measurement of submicrometre diameters of tapered optical fibres using harmonic generation. *Optics Express* **18**, 7693 (2010).
2. Karapetyan, K., Alt, W. & Meschede, D. *Optical fibre toolbox for Matlab, version 2.1* [[www.mathworks.com/matlabcentral/fileexchange/27819](http://www.mathworks.com/matlabcentral/fileexchange/27819)] (2011).
3. Garcia-Fernandez, R., Alt, W., Bruse, F., Dan, C., Karapetyan, K., Rehband, O., Stiebeiner, A., Wiedemann, U., Meschede, D. & Rauschenbeutel, A. Optical nanofibers and spectroscopy. *Appl. Phys. B* **105**, 3–15 (2011).

To my family.  
Dla mojej Kasi



# Acknowledgements

I would like to express my sincere gratitude to people who have helped me during this project.

All our samples were fabricated using the fibre pulling machine in the group of Arno Rauschenbeutel. “Production” trips to Mainz and Vienna were not only necessary for the work, but also really enjoyable thanks to the wonderful people and atmosphere in this group.

I am grateful to Gilberto Brambilla for inviting me to visit his group and perform some experiments in ORC, Southampton. Discussions with Gilberto and his colleagues Tim Lee, Yongmin Jung, and Peter Horak during and after this trip have especially helped in building the theoretical model of microfibres.

John Wooler from Fibrecore Ltd., Southampton, generously provided us with many fine details of fibre manufacturing.

High-quality SEM measurements could be performed thanks to Stephan Irsen from Research Center CAESAR, Bonn. During sample preparation and measurements, Angelika Sehrbrock has helped us a lot.

Ganz herzlich bedanke ich mich bei allen Mitarbeitern der mechanischen Werkstatt, as well as the whole “support team” of our institute: Annelise von Rudloff-Miglo, Fien Latumahina, Ilona Jaschke, Dietmar Haubrich, and Friedrich Ernst.

The results reported in this thesis could not have been achieved without the joint work with my wonderful team-mates Fabian Bruse, Cristian Dan, Dima Pritzkau, and Uli Wiedemann. Uli was not only my colleague, but also a continuous supporter from my very first hour in Bonn.

Throughout my time in Bonn, but especially in the last two years, when I switched to investigation of interferometers, Wolfgang Alt was my helpful advisor in all aspects of experimental, theoretical, and even programming work.

Successful work is impossible without the creative and joyful atmosphere in the research group. And I am fortunate to have not only spent the last five years in the group of Prof. Meschede, but also to have made many good friends here, including Andreas Steffen, Tobias Kampschulte, René Reimann, Wolfgang, Uli, Dima, and hopefully many others.

Of course, nothing of this would have been possible at all if Prof. Meschede did not invite me to come to Bonn and take part in this exciting project.

I thank my friends Dagmar Broemme, Boris Banchevsky, and Sergei Zhukovsky and my whole family, especially my beloved Kasia and my brother Daniel, for their support during my time in Germany, in particular in the not so easy periods.

# Contents

<b>Introduction</b>	<b>xiii</b>
<b>Abbreviations</b>	<b>xv</b>
<b>1 Single optical microfibre modal interferometer</b>	<b>1</b>
1.1 Optical microfibres (OMFs) . . . . .	1
1.1.1 How to make an OMF . . . . .	2
1.1.2 Light guidance in optical fibres and microfibres . . . . .	3
1.1.3 Fibre modes . . . . .	4
1.1.4 Fundamental mode evolution in OMF . . . . .	7
1.2 Single OMF modal interferometer (SOMMI) . . . . .	10
1.2.1 Mode coupling . . . . .	10
1.2.2 Mode interference . . . . .	13
1.2.3 Evanescent field and phase velocity of the two modes in the waist . . . . .	13
<b>2 Computer simulation</b>	<b>15</b>
2.1 What needs to be calculated . . . . .	15
2.2 Problems of available software . . . . .	17
2.3 Mathematical model of light propagation in OMF . . . . .	18
2.3.1 Dielectric cylindrical waveguide—two-layer model . . . . .	19
2.3.2 Taper regions—three-layer model . . . . .	24
2.3.3 Choosing right model for each OMF region . . . . .	30
2.3.4 Mode coupling . . . . .	31
2.3.5 Critical angle theory . . . . .	33
2.4 Optical Fibre Toolbox (OFT) . . . . .	35
2.4.1 What OFT can do . . . . .	35
2.4.2 Example: Application to diameter measurement based on harmonic generation . . . . .	35
2.5 SOMMI simulation . . . . .	38
2.5.1 Cylinder interferometer . . . . .	38
2.5.2 Spectral interferometry . . . . .	39
2.5.3 Stretch-interferometry . . . . .	41
2.5.4 Actual SOMMI shape . . . . .	44

2.6 Summary . . . . .	49
<b>3 Samples</b>	<b>51</b>
3.1 Production . . . . .	51
3.1.1 Optical fibre tapering . . . . .	51
3.1.2 Pulling machine . . . . .	52
3.1.3 Optical fibre type selection . . . . .	53
3.1.4 Target sample shape . . . . .	54
3.1.5 Sample shape verification . . . . .	60
3.2 Stretch-interferometry . . . . .	69
3.2.1 Setup . . . . .	69
3.2.2 Experiment . . . . .	69
3.2.3 Results and analysis . . . . .	70
3.3 Handling . . . . .	73
3.3.1 Fibre holder design . . . . .	74
3.3.2 Using samples in experiments . . . . .	76
3.4 Conclusions . . . . .	78
<b>4 Spectral interferometry</b>	<b>81</b>
4.1 Optical setup . . . . .	81
4.2 Automated spectrum acquisition . . . . .	82
4.3 Spectrum analysis . . . . .	82
4.3.1 Characteristic shape: simulation . . . . .	82
4.3.2 Characteristic shape: experiment . . . . .	83
4.3.3 Data processing . . . . .	85
4.3.4 Use of zero-dispersion point for diameter determination . . . . .	86
4.4 Spectral interferometry in air . . . . .	87
4.5 Interferometry in liquids . . . . .	89
4.5.1 Setup . . . . .	90
4.5.2 Test liquids . . . . .	92
4.5.3 Temperature variation . . . . .	93
4.5.4 Sample design . . . . .	93
4.5.5 Results and analysis . . . . .	95
4.6 Conclusions . . . . .	97
<b>5 Summary and outlook</b>	<b>99</b>
5.1 Pulling machine . . . . .	100
5.2 Sample shape . . . . .	101
5.3 Dispersion measurement of atoms and molecules . . . . .	102
5.4 Simulation . . . . .	102
<b>Appendix A Guided mode solutions</b>	<b>103</b>
A.1 Two-layer waveguide . . . . .	103
A.1.1 Scalar approximation (LP modes) . . . . .	103

A.1.2	Vector solution . . . . .	104
A.2	Three-layer fibre . . . . .	104
A.2.1	Scalar approximation (LP modes) . . . . .	104
A.2.2	Vector solution . . . . .	104
A.3	Anisotropic fibre . . . . .	105
A.4	Model applicability . . . . .	105
<b>Appendix B</b>	<b>Algorithm description</b>	<b>107</b>
B.1	Search for guided modes . . . . .	107
B.2	Tracing the dispersion curve . . . . .	108
<b>Appendix C</b>	<b>OMF samples</b>	<b>109</b>
<b>Appendix D</b>	<b>Fibre holder</b>	<b>111</b>
D.1	Fixing a sample in the holder . . . . .	111
D.2	Transportation and storage . . . . .	113
<b>Appendix E</b>	<b>Sample 204 in Cargille liquids</b>	<b>115</b>
<b>Bibliography</b>		<b>117</b>



# Introduction

People have been progressing in their attempts to manipulate propagation of light for more than 2500 years,\* and have achieved significant success on the way. Today we can transfer single photons over dozens of kilometres using optical fibres [4] and perform almost magic by producing invisibility cloaks using photonic crystals [5].

Light usually propagates either inside an optical material—as in fibres, prisms, and photonic crystals—or in the space between optical elements such as lenses and mirrors. From this point of view, *optical microfibres* fill the gap: Light follows a microfibre, which can be bent or curled, as with usual fibres. At the same time, it remains open for interaction with the surrounding medium, almost like a free-space beam.

\* \* \*

Until the 1960s, optical fibres were only used for illumination and technical and medical imaging, because high absorption losses were making any glass element thicker (longer) than a few dozens of centimetres useless [6]. In 1966, in their Nobel prize-winning paper [7], Kao and Hokcham predicted that glass fibres can have very small absorption losses. The modern era of fibre optics began in 1970, when Corning researchers made Kao’s theoretical prediction a reality.

In the early days of fibre optics, light was guided in glass threads surrounded by air or a low refractive index liquid—i.e. by total internal reflection at the outer surface of the fibre. Already in the 1950s, it became obvious that the light-guiding core of the fibre should be surrounded by a transparent low-refractive-index cladding, to minimize the influence of the outer medium on light propagation. The core was made almost as large as the cladding, to maximize the imaging resolution and the power efficiency of devices [6]. In their paper, Kao and Hokcham have not only considered losses in the fibre material, but also thought of the optimal conditions to guide light. They suggested that it was actually beneficial to reduce the diameter of the core relative to the cladding: in a very thin—just a few wavelengths in diameter—core surrounded by a cladding of almost the same refractive index, light can only propagate in the fundamental

---

\*The first lenses were probably produced by the Assyrians, such as the famous Nimrud lens.

transverse mode. This ensures a high data transmission rate (used in telecommunication) and an excellent output beam quality, due to which these fibres are commonly used in research labs.

Usually, propagating light should be “protected” from any disturbances, therefore it is transported deep inside the fibre. The standard cladding diameter is 125  $\mu\text{m}$ , about 20...40 times larger than the core. However, for many applications such as signal routing and energy splitting, as well as for basic research it is of obvious interest to gain physical access to propagating light and make it interact with surroundings. Ideally, this zone of interaction should be restricted, leaving a “normal” fibre optimized for guidance at both ends of the interaction region. This idea leads to *fibre tapering*, which is a local reduction of the fibre diameter [8].

Tapering is performed by simultaneously heating and carefully stretching of a fibre. The fibre gets thinner but continues to guide light. Even when tapering is as drastic as from 125  $\mu\text{m}$  down to  $\sim 0.5 \mu\text{m}$ , tapered fibres can have almost 100 % transmission [9].

Such microfibres have a number of interesting properties. Due to the very small diameter and a high refractive index step at the surface (between glass and air), they concentrate guided light into a small transverse area, thereby increasing intensity and providing for such effects as harmonic and supercontinuum generation at low peak power [10–12]. Also, depending on the diameter, more than half of the light can propagate in the evanescent field around the fibre. This makes such microfibres useful for a number of applications, ranging from light coupling between fibres [13] to sensing [14] to probing atomic fluorescence [15] to atom trapping [16]. In sensing, the strong light concentration around the microfibre provides for a very high sensitivity [17].

Dispersive sensing is one more application area for optical microfibres. It can be used for off-resonant and therefore non-absorbing sensing, refractive index measurement, and non-destructive monitoring of light-sensitive objects such as organic molecules. Microfibre-based interferometers can be significantly smaller than their fibre-less counterparts. They also combine the convenience of fibre-coupled devices with the high sensitivity of microfibres. Interferometers can contain a microfibre in one arm [18], in both arms [19], or can actually be built with just a single microfibre, the two interferometer arms being represented by two different transverse guided modes [20]. Interferometers of the latter type promise the most compact devices [21] and can be easily manufactured at the current level of technology. They are the subject of the present thesis.

# Abbreviations

EVE	eigenvalue equation
HE/EH	hybrid fibre modes
LP	linearly polarized (mode)
OFT	Optical Fibre Toolbox [2]
OMF	optical microfibre
OSA	optical spectrum analyser
SEM	scanning electron microscope/microscopy
SHG	second harmonic generation
SOMMI	single OMF-based modal interferometer
TE	transverse electric (mode)
THG	third harmonic generation
TM	transverse magnetic (mode)
UV	ultraviolet
ZDW	zero-dispersion wavelength



# 1

## CHAPTER

# Single optical microfibre modal interferometer

In this chapter, I introduce OMFs and the subject of this project—single-microfibre modal interferometer—without mathematics. The rigorous theoretical treatment is given in Chapter 2, where I describe the computer simulation of our interferometers.

## 1.1 Optical microfibres

Microfibre and nanofibre, ultrathin optical fibre, tapered optical fibre, photonic nanowire—these and many other names met in the literature are all used for the same optical element—a dielectric light waveguide with one part (called *waist*) having transverse dimensions on the scale of the wavelength of guided light and a much larger length. Usually, microfibres have a circular symmetry, though some groups have tried to use polarization-maintaining fibres of different geometries [22, 23]. In this project, only circularly symmetric fibres are considered.

The large variety of names is explained partly by the fact that these elements have attracted wide interest only recently, and no name has been commonly accepted yet. On the other hand, depending on the exact design and application, there is a desire to emphasize different aspects of physics and engineering of these elements.

At both ends the waist is connected to a usual optical fibre (typical diameter 125  $\mu\text{m}$ ) with the so called *tapers*—relatively long conical regions with a slowly changing diameter (Fig. 1.1). The ends of the OMF, where it can be spliced to another optical fibre or where a free-space beam can be coupled in or out of the OMF, are called *pigtails*.

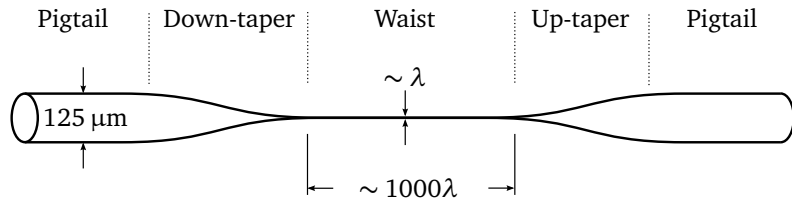


**Figure 1.1:** Tapered optical microfibre.

Because the wavelength of light in optical research usually ranges from hundreds of nanometres to a few micrometres, we will call this optical element a *tapered optical microfibre* or just an *optical microfibre* (OMF).

The main idea behind an OMF is the following. In a usual optical fibre, light is completely confined inside glass. It makes it possible to handle fibres easily, bend them, collect them in cables. Light travels inside the fibre, unperturbed. This explains their wide use, but at the same time makes it impossible to conduct any light-matter interaction experiments. In the OMF waist, where the fibre is very thin, light propagates to a large extent *outside* the fibre, in the evanescent field, forming a sort of a light rod with a diameter, larger than the diameter of the waist. In practice, more than half of the light power can propagate outside the fibre. As long as light does not “touch” anything, it can propagate along the waist practically without losses, over an arbitrary distance. In this region, it is open for interaction with the surrounding. Also, the whole power of the beam coupled into the fibre is concentrated here in a small transverse area. Therefore light intensity in the waist can be very high, thereby increasing the efficiency of any interaction.

### 1.1.1 How to make an OMF

The beauty of OMFs is that they are very easy to produce—at least in theory. One takes a usual\* commercial optical fibre (fused silica waveguide of  $125\text{ }\mu\text{m}$  diameter coated with a  $250\text{ }\mu\text{m}$  diameter plastic coating), removes the coating, and fixes the bare fibre to two coaxial translation stages. Then these stages pull the fibre at the ends while at the same time its central part is heated with a flame, a laser, or an electrical heater (Fig. 1.2). This process may be optimized to obtain various final shapes but the general idea remains that simple: heat and stretch. One can in fact achieve most of the nice properties of OMFs with a very simple and cheap setup already, though high performance OMFs require very high quality stages and heat source as well as an accurate model and a sophisticated computer control of the pulling process.

---

\*In the scope of this work, a “usual” or a “standard” optical fibre relates to untapered, commercially available optical fibres, from which our samples are made.

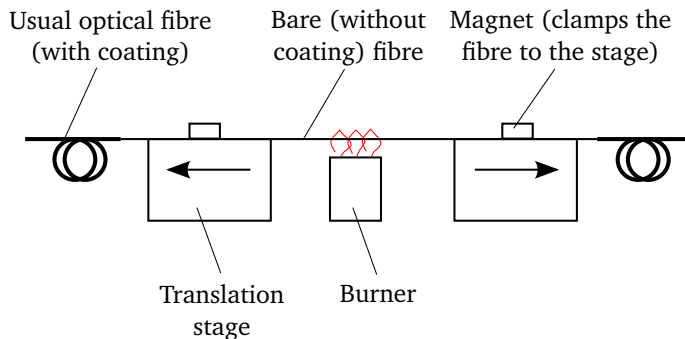


**Figure 1.2:** Making OMF: an optical fibre is thinned down (tapered) by heating and stretching.

### 1.1.2 Light guidance in optical fibres and microfibres

The unprocessed (untapered) pigtails of a microfibre are just a standard optical fibre. Although a large variety of optical fibres exist, OMFs are usually fabricated from single-mode fibres with simple cylindrical core and cladding. The core diameter varies among different fibre types depending on the design wavelength, and is typically on the order of 5...10  $\mu\text{m}$ . On the contrary, the cladding diameter is standardized, the most common diameter being 125  $\mu\text{m}$  (Fig. 1.3a).

Both the core and the cladding are made from fused silica, i.e. a high-purity glass. To achieve light guidance in the fibre, the core should have a slightly higher refractive index than the cladding. Therefore the core or the cladding are doped. The refractive index difference between the core and the cladding is typically on the order of just 0.005 refractive index units (compare to the refractive index of silica of 1.45) [24]. This small refractive index step\* is sufficient to ensure guidance of light by the total internal reflection at the core-cladding interface.

Having a standard fibre at both ends of the microfibre means that it can be directly connected to standard fibre optics components and instruments. It ensures simple experimental setup and makes OMFs a promising tool in applications outside research labs.

When a fibre is tapered, its core-cladding structure remains unchanged and only the diameter decreases. This means that in the waist, the fibre has the micrometre-diameter cladding and the core, which is still about 10...20 times thinner ( $\sim 100\text{ nm}$ ). Because the wavelength of light is on the order of a micrometre, light does not “see” the very thin core and is thus guided by the cladding (Fig. 1.3b).

Although both the untapered pigtails and the waist may well guide light, it may not be the case for the tapers. If the taper is steep, the total internal reflection

---

\*There are step-index and gradient-index optical fibres. OMFs are usually made from the step-index fibres, probably because they are cheaper and because larger variety of step-index fibres can be found in the market than of the gradient-index ones.

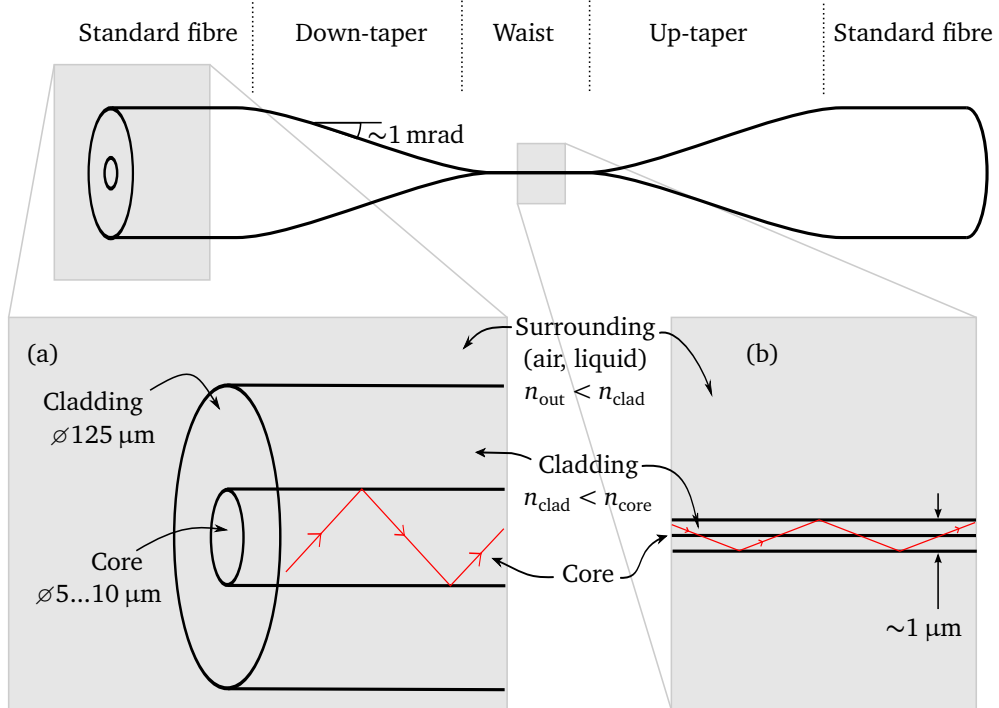


**Figure 1.3:** Light guidance in (a) the standard optical fibre and (b) in the microfibre waist. In a standard fibre, light is guided in the core due to the total internal reflection at the core-cladding interface. The refractive index step between the core and the cladding is about 0.35 %. In the microfibre waist, the core vanishes and light is guided by the total internal reflection between the cladding and the surrounding medium (refractive index step on the order of 10...40 %).

condition may be violated and light will be partially or completely lost [25]. Therefore the tapers are made shallow, with the slope angle on the order of milliradians [26]. Taking into account the initial fibre diameter and the diameter of the waist of 125  $\mu\text{m}$  and 1  $\mu\text{m}$  respectively, we end up with the (each) taper length of a few centimetres.

### 1.1.3 Fibre modes

An optical fibre is a waveguide, and light travels through it in the form of *guided modes*, each having its specific characteristic transverse field distribution and propagation constant. Figure 1.4 shows the transverse intensity distribution of the lowest modes guided in the untapered fibre. Note that for the sake of illustration I have simulated 750 nm light modes in a Corning SMF-28 fibre. This is a standard telecom fibre designed to operate at the wavelength above 1300 nm, where it is single-mode. Therefore at 750 nm it supports (i. e. can guide) more

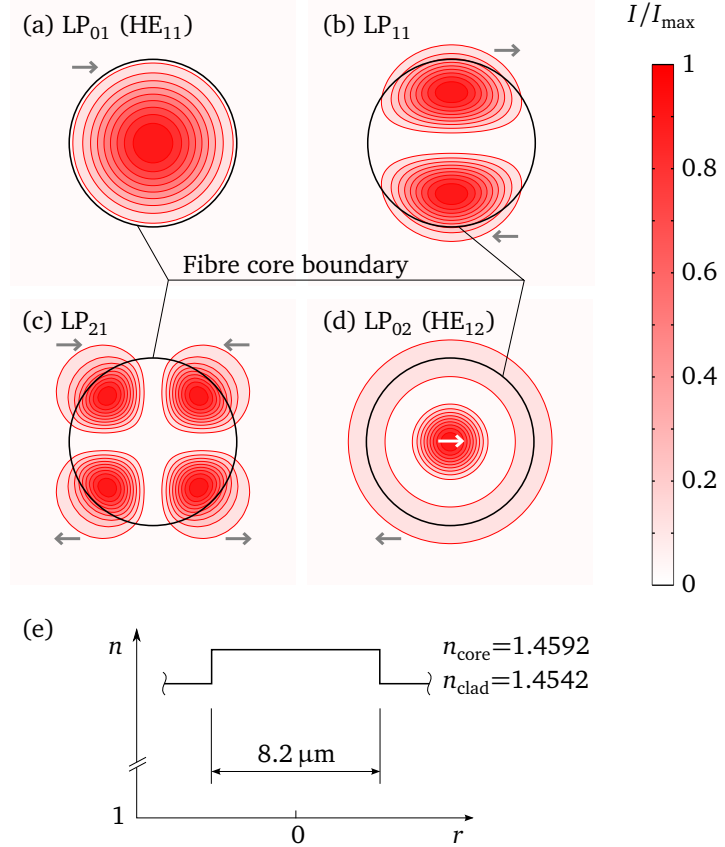


**Figure 1.4:** Intensity distribution of the lowest modes of untapered fibre. Simulated for SMF-28 fibre (core diameter  $8.2 \mu\text{m}$ ,  $n_{\text{clad}}=1.4542$  (pure silica),  $n_{\text{core}}=1.4592$  (Ge-doped silica)) at 750 nm. Arrows indicate the polarization direction within each spot. (a)–(d) First four LP modes. (e) Refractive index profile. This and all other simulation plots in this work were calculated using the Optical Fibre Toolbox for Matlab [2] described in chapter 2.

than one mode.

**Linearly polarized and vector modes** When speaking of guided modes, two different notations are used: the so called linearly polarized modes (LP) and the hybrid (HE/EH) and transverse (TE/TM) modes. The LP waveguide modes are the solutions of Maxwell's equations in the so called weak guidance limit. It is observed when the refractive index step between the waveguide layers is  $\Delta n \ll 1$ . In this case, the light wave propagates almost like in the bulk material, in particular it can be linearly polarized and its electric  $\mathbf{E}$  and magnetic  $\mathbf{H}$  field strength vectors are practically orthogonal to the propagation direction. The lowest order, or fundamental, mode is denoted by LP<sub>01</sub>, then follow LP<sub>11</sub>, LP<sub>21</sub>, LP<sub>12</sub> etc.

A completely different situation occurs when the refractive index step of the guiding surface is large. By solving Maxwell's equations, it turns out that, in general, all six field components  $E_{x,y,z}$  and  $H_{x,y,z}$  are non-zero. Depending on the exact relation between different components, the modes are then denoted as HE, EH, TE, and TM.

Thus, the LP modes are the approximation of the exact HE/EH/TE/TM solutions. In the LP approximation, Maxwell's equations can be solved using scalar mathematics, and therefore these modes are sometimes called scalar modes. The rigorous solution requires vector calculations, therefore the HE/EH/TE/TM modes are called vector modes.

The two modes we mainly care about in the scope of this work are the  $HE_{11}$  and  $HE_{12}$  modes, to which, in the scalar approximation, correspond the  $LP_{01}$  and  $LP_{02}$  modes. The  $LP_{11}$  and  $LP_{21}$  modes correspond to a bunch of vector modes each, meaning that in the scalar approximation some of the vector modes become degenerate in the propagation constant (Tab. 1.1; see also Fig. 2.5 on page 24).

**Table 1.1:** Degeneracy of vector modes [27, p. 154].

LP modes	Vector modes
$LP_{0m}$	$HE_{1m}$
$LP_{1m}$	$TE_{0m}, TM_{0m}, HE_{2m}$
$LP_{(l>1)m}$	$HE_{(l+1)m}, EH_{(l-1)m}$

**Mode guidance** The modes are orthogonal to each other. Therefore, once excited, they can propagate along the fibre without intermodal power transfer, as long as the fibre properties remain unchanged.

The number of modes supported by a cylindrical waveguide scales with the V-parameter [28]:

$$V = \frac{\pi d}{\lambda} \sqrt{n_{in}^2 - n_{out}^2},$$

where  $d$  is the waveguide diameter,  $\lambda$  the wavelength of light,  $n_{in}$  and  $n_{out}$  the refractive indices of the materials inside and outside the cylinder. From this equation it is clear that the number of modes supported by the fibre core is lower, at the same wavelength, than the number of modes supported by the cladding because of a much larger cladding diameter and a much higher refractive index step (see Fig. 1.5).

Usually, optical fibres are operated in the core-guidance regime, meaning that light is coupled into the core and guided by the total internal reflection at the core-cladding interface. The fibres are designed such that the evanescent field of the propagating wave never reaches the outer surface of the cladding.

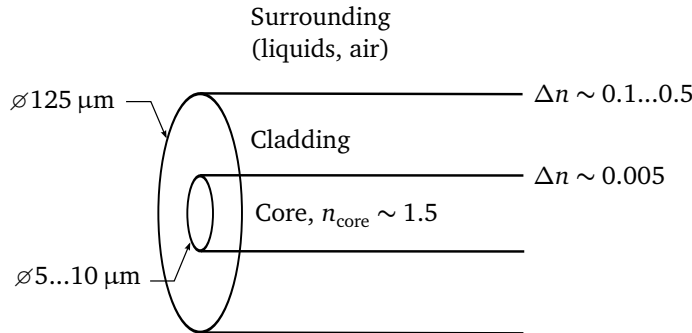


**Figure 1.5:** Refractive index steps in a typical optical fibre.

#### 1.1.4 Fundamental mode evolution in OMF

Let's now consider what happens to a light mode propagating from the untapered pigtail into the waist (Fig. 1.6). Unlike in the example above (Fig. 1.4), we now consider the actual fibre often used in our experiments (Fibercore SM800). It is a single-mode (can only guide the fundamental  $\text{HE}_{11}$  mode) fibre for wavelengths above 800 nm.

We assume a slow change of diameter in OMF tapers, with the taper slope on the order of 1 mrad. In this case, the fundamental mode, excited in the input pigtail, will propagate through the whole OMF adiabatically: no power will be transferred to other modes, guided or radiation. The solutions of Maxwell's equations in each point along a tapered waveguide are very close to the solutions for a cylindrical waveguide of the corresponding (local) diameter. This hold for taper angles upto, at least, 100 mrad [29]. Therefore we can consider each cross-section of the fibre independently.

Figure 1.6(a) shows the normalized intensity distribution  $I/I_{\max}$  in the untapered part of the fibre. As the fibre diameter starts decreasing, the tiny core-cladding refractive index step “cannot keep” the light inside the small core, and the mode field expands into the cladding. In the untapered fibre, with the core diameter of  $4 \mu\text{m}$ , the mode field diameter (MFD, diameter encompassing 86 % of propagating power) is  $5.7 \mu\text{m}$ . For a thinner fibre with a  $3 \mu\text{m}$  core it is already  $7.2 \mu\text{m}$ . That is the core decreases and the MFD increases. This goes on until the field starts “feeling” the boundary between the cladding and the surrounding. The much higher refractive index step of the outer boundary (see Fig. 1.5) can compress the field further. Figures 1.6(c) and (d) demonstrate that between the fibre diameters of 20 and  $5 \mu\text{m}$  the amount of power inside the fibre practically does not change. Finally, at still smaller diameters (Fig. 1.6e and f), even the strongly guiding outer boundary cannot “keep” the field inside any more and a considerable part of the total power starts propagating outside the fibre, in the evanescent field.

This illustration reveals several interesting properties of OMFs. The field,

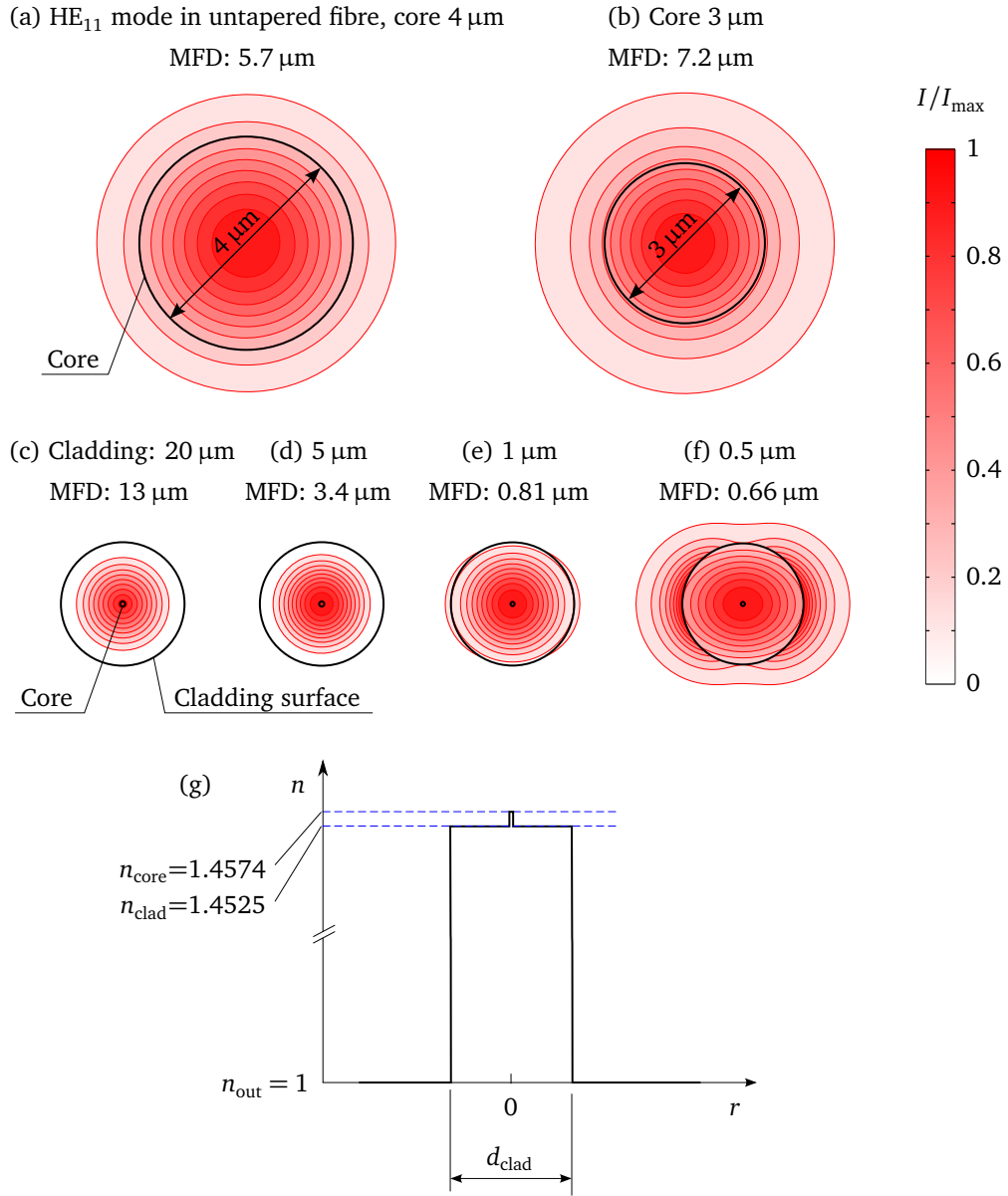


**Figure 1.6:** (a)–(f) Variation of the normalized intensity of the HE<sub>11</sub> mode with fibre diameter. (g) Refractive index profile. Note: plots (a) and (b) are not to scale to plots (c)–(f). In plots (c)–(f) the cladding diameter is shown constant to better show the mode expansion relative to the fibre. The actual mode field is compressed (note MFD). Fibre: Fibercore SM800 (core 4 μm, cladding 125 μm, NA=0.12). Wavelength: 850 nm.

coupled into the input pigtail, is transversely compressed, leading to the increase of intensity. The effective area of the HE<sub>11</sub> mode in Fig. 1.6(f) is 74 times smaller than in Fig. 1.6(a). The actual losses in our OMF samples are below 5 %, which means that the intensity of the field increases by about a factor of 70.

Another, not so obvious effect, is the increase of intensity *outside* the fibre, in the surrounding medium. Figure 1.7 shows the dependence of the intensity (azimuthally averaged) at the surface of the fibre. For very small diameters, even the strongly guiding cladding-surrounding surface does not confine light any more, the mode field expands and eventually becomes infinitely large for  $d = 0$ , leading to zero intensity everywhere.

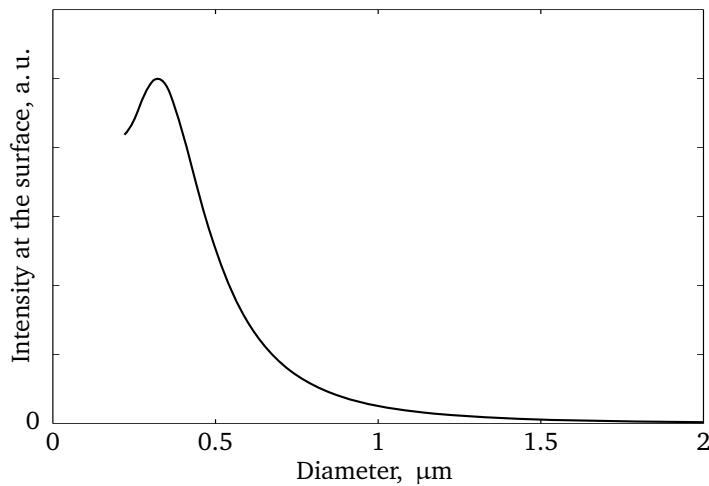


**Figure 1.7:** Intensity just outside the fibre (HE<sub>11</sub> mode at 750 nm, silica fibre in air).

At the maximum intensity point in Fig. 1.7, the light intensity around the OMF is similar to that in the focal point of a tightly focussed free-space beam. However, unlike the free-space beam after the focal point, the fibre mode does not rapidly expand but remains confined and guided by the OMF waist. The waist can theoretically be infinitely long, and practically it is much longer (millimetres) than the depth of focus in case of tight free-space focusing (on the order of a wavelength, i.e. microns). This creates a unique situation of “infinite focus” providing

- high light intensity
- over large length
- in free space around the fibre

and setting excellent conditions for light-matter interaction experiments. The most straightforward way of using microfibres is putting some absorbing material

on or around the waist, shine white light into the input end and observe the spectrum at the output end. Due to the high intensity and the long interaction length, this approach is very suitable for high-sensitivity absorption spectroscopy [17].

## 1.2 Single OMF modal interferometer (SOMMI)

To extend OMF application to dispersive sensing, one needs to convert it into an interferometer. For this, a reference arm is needed in addition to the probe arm. The input beam should be split into two arms by a beam splitter, light should propagate in the two arms independently, then be recombined in a beam recombiner, and finally the interference result should be observed at one or two output ports. For example, a Mach-Zehnder type interferometer is shown in Fig. 1.8.

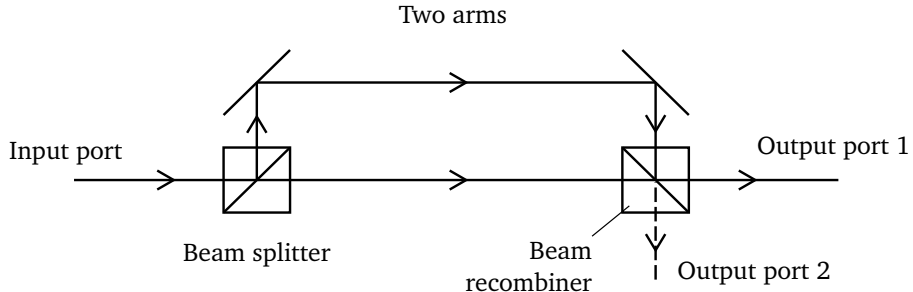


Figure 1.8: Mach-Zehnder interferometer.

Three types of OMF-based interferometers were proposed: with one OMF in the probe arm only [18], with OMFs in both arms [19], and with both arms combined in a single OMF and represented by two different transverse modes [20]. This work is devoted to the last type, which is most compact, easiest to manufacture, and has shown the highest sensitivity among these three types so far [23].

A single OMF-based modal interferometer (SOMMI) is schematically shown in Fig. 1.9. The input pigtail is single-mode and supports only mode 1. In the down-taper, the guidance regime changes from the core-guidance to the cladding-guidance, and the fibre becomes multimode. Provided that the down-taper has a proper shape, some energy of mode 1 can be coupled to mode 2, and the two modes will then propagate along the waist. In the up-taper, the two modes interfere, and the resulting mode 1 is guided out by the output single-mode pigtail. The power remaining in mode 2 is lost, since the output pigtail does not guide it.

### 1.2.1 Mode coupling

The fundamental  $HE_{11}$  mode can obviously play the role of mode 1 in Fig. 1.9. Then some other transverse fibre mode is needed to work as mode 2. This mode should be excited in the down-taper (mode splitting) and interfere with the  $HE_{11}$

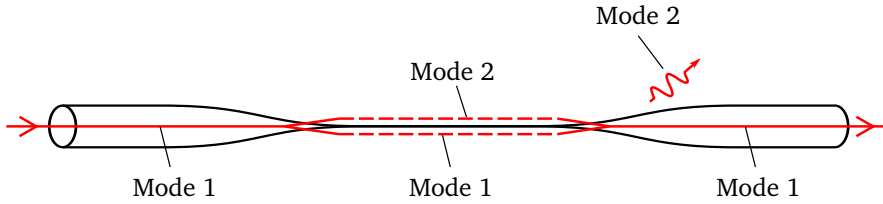


**Figure 1.9:** Single OMF-based modal interferometer. In the down-taper, the mode of the input pigtail is split into two modes of the waist. In the up-taper, the modes interfere.

in the up-taper (mode recombination). Mode splitting and recombination require mode coupling—a process, in which some power is transferred from one propagating mode to another.

In a translation-invariant cylindrical waveguide, different transverse modes are orthogonal, meaning that their overlap is zero and no coupling can occur between them. However, in tapers, the translation invariance is violated, and the modes can actually couple. If the waveguide is rotationally symmetric, which is the case for conical tapers, only modes of the same rotational symmetry can be coupled. For example, modes  $\text{HE}_{11}$  ( $\text{LP}_{01}$ ) and  $\text{HE}_{12}$  ( $\text{LP}_{02}$ ) in Fig. 1.4 on page 5 are of the same rotational symmetry, while mode  $\text{LP}_{11}$  is not. Therefore mode  $\text{HE}_{11}$  can only be coupled to the  $\text{HE}_{12}$  mode (and higher  $\text{HE}_{1m}$  modes), but not to the  $\text{LP}_{l>0,m}$  modes.

The second condition needed for two modes to get coupled is phase-matching. Different modes propagate along the fibre at a different phase velocity, which also changes with the fibre diameter. Figure 1.10(a) shows the dependence of  $c/v_{\text{phase}}$  (where  $c$  is the speed of light in vacuum, and  $v_{\text{phase}}$  the phase velocity) on the fibre diameter for modes  $\text{HE}_{11}$  and  $\text{HE}_{12}$ . The two curves never intersect. Therefore, in a constant diameter-waveguide no energy transfer will occur between the two modes, whatever the fibre diameter.

In the region where the two curves approach each other (around  $d \approx 40 \mu\text{m}$ ), the mode beat length between increases. If some power is transferred from mode  $\text{HE}_{11}$  to mode  $\text{HE}_{12}$  and then the two curves get apart again, mode coupling will have occurred. From this it is intuitively clear, that the steeper the taper slope (i. e. the quicker the modal curves go apart from each other after having come close) the more probable it is that the modes will get coupled. And vice versa, for very shallow tapers, beating will always prevent coupling. Mode propagation without coupling is called *adiabatic*, and mode propagation with coupling is called *non-adiabatic*. One can then speak of adiabatic and non-adiabatic tapers. An interferometer requires non-adiabatic tapers, while usual sensing applications benefit from adiabatic OMFs [3].

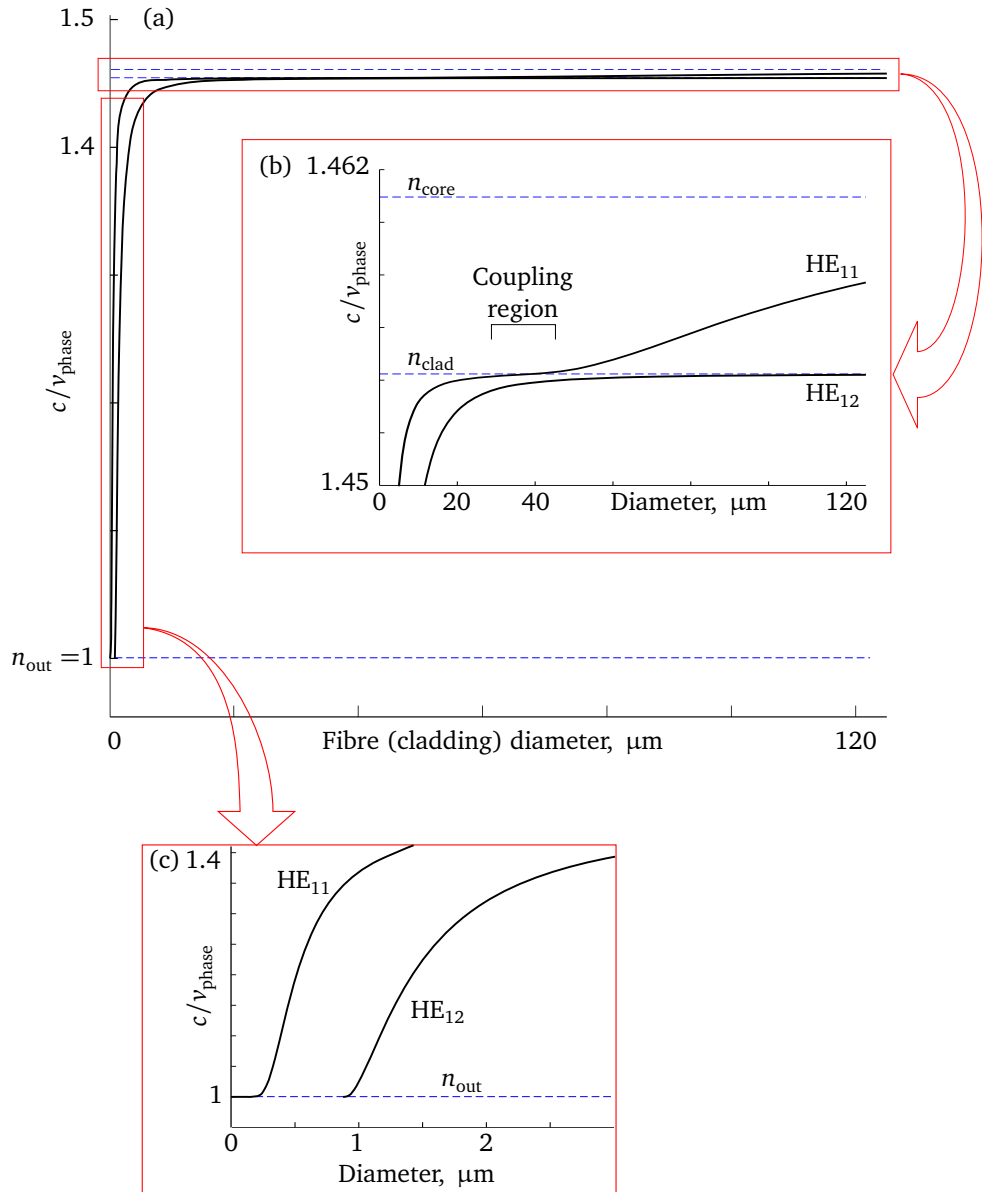


**Figure 1.10:** Phase velocity ( $c$  is the speed of light in vacuum) dependence on the local fibre diameter  $d$  for the  $\text{HE}_{11}$  and  $\text{HE}_{12}$  modes. The dashed lines indicate the material refractive indices of the core, the cladding, and the outside medium. (a) Mode dispersion in the whole OMF, from 125  $\mu\text{m}$  pigtailed down to sub-micrometre waist. (b) Vertically zoomed region of large diameters. For diameters  $< 125 \mu\text{m}$ , the  $\text{HE}_{12}$  curve is always below  $n_{\text{clad}}$  indicating that this mode is not guided by the single-mode core. Around 40  $\mu\text{m}$ , the modal curves approach each other providing the opportunity for mode coupling. (c) Horizontal zoom of the waist region. To guide both interfering modes, the waist should be thicker than  $\sim 1 \mu\text{m}$ . (Calculated for an SM800 fibre in air, at 750 nm.)

### 1.2.2 Mode interference

Once the fundamental mode  $\text{HE}_{11}$  of the input pigtail is split into the  $\text{HE}_{11}$  and  $\text{HE}_{12}$  modes in the down-taper, these two modes can propagate further along the fibre adiabatically, because of the large phase mismatch everywhere outside the coupling region (see Fig. 1.10c). If the tapers are adiabatic beyond the mode splitting region and the waist is thick enough to guide the  $\text{HE}_{12}$  mode (mode  $\text{HE}_{11}$  is always guided), the two modes will propagate until they reach the coupling region in the up-taper. (The up-taper is usually symmetric to the down-taper.) There the modes again couple to each other.

Depending on the phase relation between the modes, this second coupling can result in constructive or destructive interference for the  $\text{HE}_{11}$  mode. The output pigtail of the OMF can only guide the  $\text{HE}_{11}$  mode out, the  $\text{HE}_{12}$  mode being lost in the up-taper. Thus, the power of the output signal depends on the phase relation between the two modes, and the OMF becomes an interferometer.

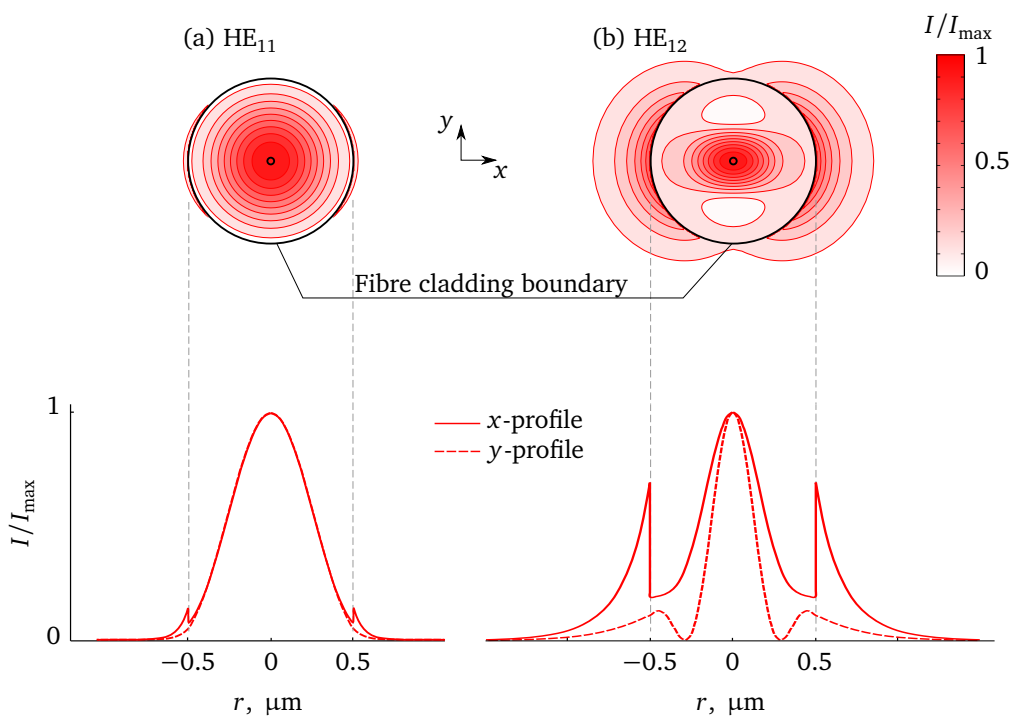
### 1.2.3 Evanescent field and phase velocity of the two modes in the waist

Figure 1.11 shows the intensity distribution of the  $\text{HE}_{11}$  and  $\text{HE}_{12}$  modes in a  $1\text{ }\mu\text{m}$  diameter fibre waist. As much as 60 % of  $\text{HE}_{12}$  power propagates around the fibre, in the evanescent field. For  $\text{HE}_{11}$ , it is just over 3 %. This physical situation leads to two effects.

Firstly, the refractive index of the surrounding material influences the  $\text{HE}_{12}$  mode much stronger than the  $\text{HE}_{11}$  mode. Therefore, the interference result strongly depends on the dispersion of the surrounding. A SOMMI can therefore act as a refractive index sensor or be used for dispersive sensing of such species as atoms and molecules.

Secondly, because a lot of power of the  $\text{HE}_{12}$  mode propagates around the fibre, the mode “sees” more air than glass, and thus its phase velocity is close to that in air (see Fig. 1.10c). The situation is completely different for the  $\text{HE}_{11}$  mode, which almost completely “fits” inside the fibre; its phase velocity is thus close to that in bulk glass. As the result, although the two modes pass the same physical path between splitting and recombination in the tapers, they experience different phase accumulation. If the length of the SOMMI is being changed (e.g. by stretching it), the phase accumulation changes differently for the two modes, and the interference result depends on the fibre elongation. Thus, a SOMMI can act as a stretch sensor. It can be used, for example, as the strain sensors in wind turbines, which are made from fibreglass and for which fibre sensors are therefore a natural choice.

In this work, I consider both of these types of interference.



**Figure 1.11:** Intensity distribution of (a)  $HE_{11}$  and (b)  $HE_{12}$  modes in and around a silica microfibre waist in air. Portion of power guided outside the fibre: (a) 3.3 %, (b) 60 %. Note: plot (b) is *not* the same as 1.6(f), though it looks similar. Figure 1.6 shows the evolution of the single  $HE_{11}$  mode with the fibre diameter. Here, plot (b) shows a higher  $HE_{12}$  mode at the same fibre diameter as plot (a). (SM800 fibre, 750 nm, waist diameter 1  $\mu\text{m}$ , horizontal polarization.)

# 2

## CHAPTER

# Computer simulation

The goal of computer simulation is to theoretically understand in detail how OMFs work to be able to design samples and to analyse measurement results. One of our first experimental achievements was the development of a method to measure the diameter of the OMF waist using optical harmonic generation [1]. This method also required the simulation of guided modes in OMFs. Finally, taking into account the complexity of the calculations and the total number of samples we have produced for all our experiments (more than 200), it proved to be inefficient to each time perform calculations in a semi-manual mode employed by many other groups. We have therefore created a software toolbox capable of performing all the needed calculations in the automatic mode [2].

### 2.1 What needs to be calculated

The modal interferometer response depends on the phase relation between the two propagating modes at the recombination point. Therefore we need to know the full phase evolution of each of the excited modes along the whole interferometer, starting at the down-taper, along the waist, and ending in the up-taper.

For our harmonic generation-based method of OMF diameter measurement, we need to calculate the so called phase-matching condition—a set of OMF parameters providing a constant phase relation between the fundamental and harmonic waves at given wavelengths. For efficient harmonic generation, it is also important to maximize the overlap between the field distributions of the fundamental and harmonic modes.

Thus, we need the full information about the phase and the amplitude of the modes propagating in the OMFs.

A light wave, propagating in an optical fibre, can be described mathematically by defining its electric  $\mathbf{E}(\mathbf{r}, t)$  and magnetic  $\mathbf{H}(\mathbf{r}, t)$  field distributions, where  $\mathbf{r}$  and  $t$  are the position in space and the time.  $\mathbf{E}$  and  $\mathbf{H}$  are treated similarly, therefore in this text I speak of  $\mathbf{E}$  only, while still taking  $\mathbf{H}$  into account in all calculations.

If the optical axis of the fibre coincides with the coordinate axis  $z$ , we can define the electric field of a propagating mode as

$$\mathbf{E}(\mathbf{r}, t) = \mathbf{E}_{\text{tr}}(\mathbf{r}) \exp(i\omega t - i\beta z). \quad (2.1)$$

Here  $\mathbf{E}_{\text{tr}}(x, y, z)$  is the transverse field distribution,  $\beta$  the propagation constant (waveguide analogue of the free-space wavenumber  $k$ ), and  $\omega$  the angular frequency of light. If the characteristic length of the  $z$ -dependent change of the fibre diameter is large compared to the wavelength of light (e.g. for our samples it's millimetres compared to hundreds of nanometres), then in Eq. (2.1) we have split the fast oscillating  $z$ - and  $t$ -dependent terms from the slowly varying transverse field distribution  $\mathbf{E}_{\text{tr}}$ .

$\mathbf{E}_{\text{tr}}$  and  $\beta$  are found by solving the wave equation derived from Maxwell's equations for the case of a cylindrical dielectric waveguide [30, 31]. As the result, one obtains an eigenvalue equation (EVE)\* for  $\beta$ , which has to be solved numerically. When  $\beta$  has been found, the field distribution  $\mathbf{E}_{\text{tr}}$  is calculated analytically.

If  $\beta$  is imaginary, Eq. (2.1) describes a so called *lossy*, or *radiation* mode—a mode, which is a correct solution of Maxwell's equations but which cannot be guided by the waveguide. Physically, the power of this mode is quickly lost from the waveguide due to radiation as the wave propagates along the waveguide. We are not interested in such modes and will therefore only consider the real solutions of EVEs.

The propagation constant  $\beta$  is connected to the phase velocity  $v_{\text{phase}}$  of the propagating wave:

$$\beta = \frac{2\pi}{\lambda} n_{\text{eff}}, \quad v_{\text{phase}} = \frac{c}{n_{\text{eff}}}, \quad (2.2)$$

where  $n_{\text{eff}}$  is the *effective refractive index* of the mode,  $c$  the speed of light in vacuum. Note that  $n_{\text{eff}}$  plays the same role for a waveguide mode, as the material refractive index is playing for a wave propagating in a bulk medium: it slows down the wave-front (and decreases the wavelength).

Thus, to fully describe a propagating wave in a fibre, one needs to calculate the field distribution  $\mathbf{E}_{\text{tr}}$  and the propagation constant  $\beta$  or the effective refractive index  $n_{\text{eff}}$  for the corresponding guided mode. The phase evolution of the mode as it propagates along the fibre is given by its propagation constant.

If the fibre diameter is changing (this is exactly the case in the tapers of our samples) or the measurements are performed with a broadband light source (as

---

\*Actually, a set of EVEs for different symmetries of the field distribution. Each equation is numbered with index  $l$  and each solution of a specific EVE is indexed with  $m$ . The found mode then has two indices  $(l, m)$ .

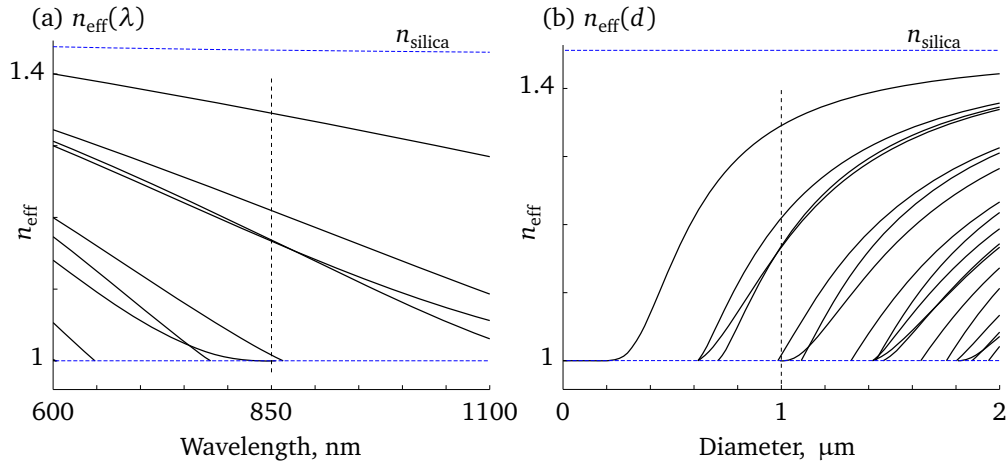


**Figure 2.1:** Mode dispersion diagram: effective refractive index of the guided modes vs. (a) wavelength of light and (b) tapered fibre diameter. Each curve corresponds to a specific guided mode. The number of curves at each wavelength (diameter) gives the number of modes guided by the fibre at that wavelength (diameter). The results are shown for a silica waveguide in air. (a) Diameter 1  $\mu\text{m}$ . (b) Wavelength 850 nm. The vertical dashed lines mark the points, corresponding to the other plot, respectively: 850 nm in (a) and 1  $\mu\text{m}$  in (b).

in some of my interferometry experiments), one has to calculate  $\beta$  for each set of wavelength-diameter pairs. One then speaks of the so called mode dispersion diagrams (Fig. 2.1).

## 2.2 Why we cannot use available waveguide simulation software

To solve the eigenvalue equations, we need some sort of a computer program. Traditionally, programs dealing with waveguides have been designed for one of the two very complex tasks: (1) finding the modes of arbitrary-shape waveguides defined by a full 3D distribution of the refractive index, and (2) simulating wave propagation in an arbitrarily complex optical system. For us, the first solution is not interesting since the general shape of all fibre modes is well-known analytically. We do not want to find it again (a very time-consuming task), we just need to find the propagation constant.

The second approach, simulation of the wave propagation, is based on one of the three methods:

1. The scalar diffraction theory, used in large optical systems (dimensions much larger than the wavelength of light). This method is not applicable to our samples having diameters down to less than the wavelength.

2. The full vector solution of Maxwell's equations using the finite elements numerical method. This approach allows to solve any optical problem and is successfully used for small-scale optical systems. However it is prohibitively slow and extremely memory-expensive in case of OMFs with their centimetre-scale length.
3. The mode expansion method based on the known analytical solutions of the wave equation. In an optical fibre, this method is the only applicable method of the three. However it requires continuous calculation of the field distributions along the fibre and is therefore much slower than the simple solving of the eigenvalue equation. The advantage of this method over our approach is that it inherently calculates mode transformation in case of non-adiabatic transitions in the fibre.

As the outcome of this situation, all the groups working in the field of tapered optical fibres, to the best of my knowledge, are writing their own codes to solve the EVEs and find  $\beta$ . There is no ready-to-use software tool to accomplish this task. That's why we had to create our own one.

While doing so, I have been able to implement an almost completely automatic calculation: one “assembles” a program for each task from the provided functions in a LEGO-manner, and then the calculation happens automatically. This is a useful feature because we typically need to solve the EVE for many different fibre diameters or wavelengths. We also need to repeat the calculations for each new type of fibre (core/cladding ratio and materials) as well as for each new material of the fibre surrounding. Therefore, manual tuning of the starting points, which is a common procedure I have seen in other groups, or verification of the calculation results become prohibitively time-consuming operations.

## 2.3 Mathematical model of light propagation in OMF

Our samples consist of the unprocessed pigtails (commercial optical fibre), two taper sections with varying diameter, and a waist. The unprocessed parts and the waist have a constant (along the fibre axis) diameter and therefore the modes in these parts are relatively easy to calculate. These parts are also most interesting in terms of the OMF guiding properties:

- The input unprocessed part determines, which modes can be delivered from a light source to the waist.
- The waist is the part where light is open to interaction with the surrounding and also where it usually has the highest intensity; this is where light-matter interaction occurs primarily.
- The unprocessed output end determines what can be seen by the detector at the output.

The tapers should be properly designed to transfer light from the input pigtail to the waist and from the waist to the output pigtail. Being made from the same commercial fibre as the pigtails, the taper also has similar properties. At the same time, modes in the tapers, where the fibre diameter and thus the guiding properties are constantly changing, should be calculated in a different manner. I start with the calculation of the cylindrical input, output, and waist parts and consider the taper regions afterwards.

### 2.3.1 Dielectric cylindrical waveguide—two-layer model

#### 2.3.1.1 Unprocessed parts of OMF

The unprocessed pigtails consist of a cylindrical core (diameter  $\sim 5 \mu\text{m}$ ) surrounded by a cylindrical cladding (125  $\mu\text{m}$  diameter). The protective plastic coating of the fibre (250  $\mu\text{m}$  diameter) is always removed before producing the tapered samples; therefore I ignore it in the model. The cladding is thus surrounded by air, vacuum, or some other medium.

The core is made from a material with a slightly higher refractive index than the one of the cladding. This makes light guidance in the fibre core possible due to total internal reflection.

Commercial fibres are designed in such a way that light is completely confined in the region close to the core and does not reach the cladding surface. For example, the Fibercore SM800 fibre\* primarily used in our experiments has the *mode field diameter* (diameter encompassing 86 % of guided power) of 5.6  $\mu\text{m}$  [32]. Since the cladding diameter is 125  $\mu\text{m}$ , no light even “touches” the fibre surface. Be it not the case, light would be lost due to absorption or scattering in the coating.

As a result, when calculating light modes in the unprocessed part of the fibre, we can ignore the presence of the surrounding, be it air, vacuum, liquid or anything else—light just does not “see” it. The fibre can then be considered as a glass rod (core) surrounded by an infinite glass cladding with a slightly lower refractive index and, hence, modelled considering only these two layers (the core and the cladding).

The solution of Maxwell’s equations in a two-layer dielectric cylindrical system is well known [30, 33]. The eigenvalue equation for  $\beta$  is [31, Eq. (B-11)]†

$$\left( \frac{J'_l(ha)}{haJ_l(ha)} + \frac{K'_l(qa)}{qaK_l(qa)} \right) \left( \frac{n_1^2 J'_l(ha)}{haJ_l(ha)} + \frac{n_2^2 K'_l(qa)}{qaK_l(qa)} \right) - l^2 \left[ \left( \frac{1}{qa} \right)^2 + \left( \frac{1}{ha} \right)^2 \right]^2 \left( \frac{\beta}{k_0} \right)^2 = 0, \quad (2.3)$$

---

\*Its specifications are given in Tab. 3.1 on page 54.

†There is a typo in  $K'$  argument the equation in the book:  $ha$  instead of  $qa$ . It can be checked by comparison with [30, Tab. 12-4 on p. 253].

where

$$\begin{aligned} h^2 &= n_1^2 k_0^2 - \beta^2, \\ q^2 &= \beta^2 - n_2^2 k_0^2, \end{aligned}$$

$J$  is the Bessel function of the first kind,  $K$  the modified Bessel function of the second kind,  $a$  the radius of the waveguide,  $n_1$  and  $n_2$  the material refractive indices of the inner and outer layers,  $k_0 = 2\pi/\lambda_0 = \omega/c$  the vacuum wave number,  $l$  the azimuthal mode index, which is present in the field components in the term (cf. Eq. (2.1))

$$\exp[i(\omega t + l\phi - \beta z)].$$

For each azimuthal mode index  $l > 0$ , Eq. (2.3) can have several roots numbered  $(l, k)$ . Each root  $\beta_{lk}$  corresponds to a separate transverse mode. These modes are called *hybrid* and have a characteristic feature that both their electric and magnetic vectors have non-zero components parallel to the direction of propagation  $z$ . For a given index  $l$ , the modes with the magnetic  $z$ -component larger than the electric one (these modes are called the HE modes) alternate with the ones with a larger electric  $z$ -component (called EH): the lowest-order mode is  $\text{HE}_{l1}$ , then follow  $\text{EH}_{l1}$ ,  $\text{HE}_{l2}$  and so on (see Fig. 2.2). The second mode index is usually marked with  $m$ . Thus the root number  $k$  corresponding to a particular mode can be calculated as  $k = 2m + 1$  for HE modes and  $k = 2m$  for EH modes.

If  $l = 0$ , we have a special case of transverse electric and transverse magnetic modes. They have the zero  $z$ -component of the electric or magnetic fields and are called  $\text{TE}_{0m}$  and  $\text{TM}_{0m}$  respectively. The EVEs for these modes look simpler [31, Eq. (B-17)]:

$$\frac{J_1(ha)}{haJ_0(ha)} + \frac{K_1(qa)}{qaK_0(ha)} = 0, \quad (2.4)$$

$$\frac{J_1(ha)}{haJ_0(ha)} + \frac{n_2^2 K_1(qa)}{n_1^2 qaK_0(ha)} = 0, \quad (2.5)$$

and  $m$  is just a root number.

If the refractive index step at the guiding interface (where total internal reflection occurs) is small,  $\Delta n_{12} \ll 1$ , one speaks of a weakly-guiding fibre, and the linearly polarized (LP) modes are a valid approximation. The EVE in this case is [31, p. 131]:

$$ha \frac{J_{l+1}(ha)}{J_l(ha)} - qa \frac{K_{l+1}(qa)}{K_l(qa)} = 0.$$

This solution is derived from the scalar wave equation. Therefore the LP modes are sometimes called scalar modes.

Using the EVEs, one can calculate the mode dispersion (versus wavelength or core diameter) of a typical fibre. As an example, let's consider the plot  $n_{\text{eff}}$  vs. wavelength calculated for a Corning SMF-28\* fibre in air (Fig. 2.3). Untapered,

---

\*For SMF-28 specs see Sec. 3.1.3 on page 53.

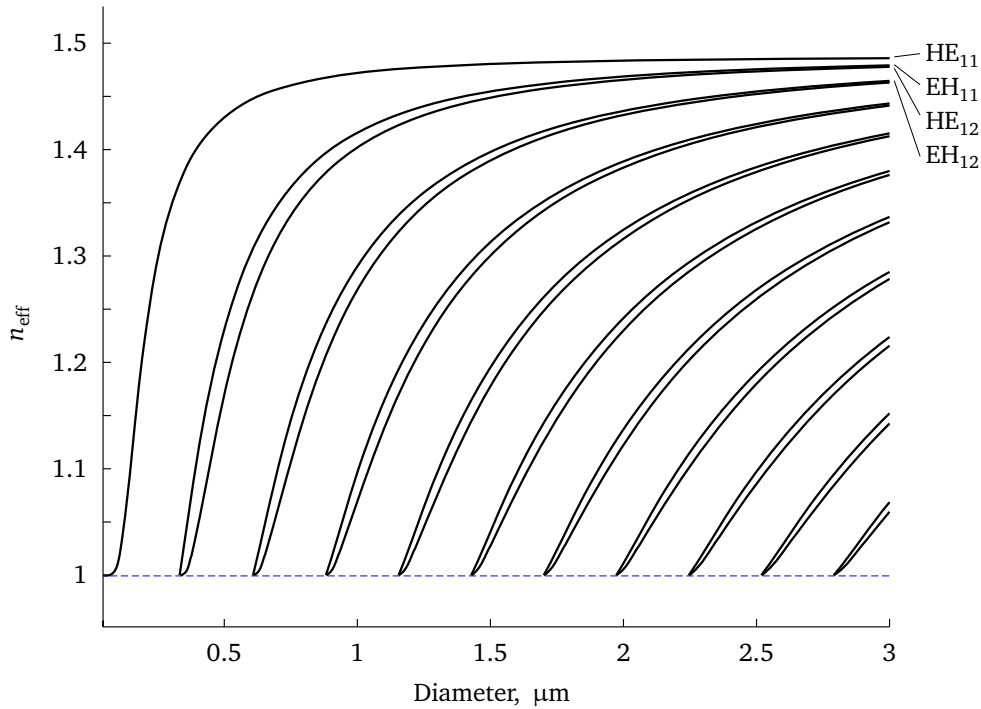


**Figure 2.2:** First order ( $l = 1$ ) hybrid (HE and EH) modes in the waist. (Silica in air, 300 nm.)

this fibre is weakly-guiding, therefore the LP-approximation is valid. At 600 nm, this fibre supports four LP modes:  $\text{LP}_{01}$ ,  $\text{LP}_{11}$ ,  $\text{LP}_{21}$ , and  $\text{LP}_{02}$ . Their  $n_{\text{eff}}$  is confined between the refractive index of the core (Ge-doped fused silica) and the cladding (pure fused silica). With the increase of the wavelength, the higher modes experience the cutoff—first the  $\text{LP}_{02}$  and  $\text{LP}_{21}$  and then the  $\text{LP}_{11}$ . Above 1300 nm, just the  $\text{LP}_{01}$  mode is guided. This is the design wavelength range of the SMF-28 fibre: it is single-mode at the telecom wavelengths of 1310 and 1550 nm. The vertical dashed line marks the point, for which the field distributions in Fig. 1.4 (page 5) was calculated.

Electric and magnetic field distributions of HE, EH, TE, and TM modes are also known and can be calculated once the value of  $\beta$  has been found from Eqs. (2.3)–(2.5). The corresponding equations are quite lengthy, therefore they are referenced in appendix A. As an example, the light intensity distribution of the four lowest LP-modes shown in Fig. 2.3 was shown in chapter 1 (Fig. 1.4 on page 5).

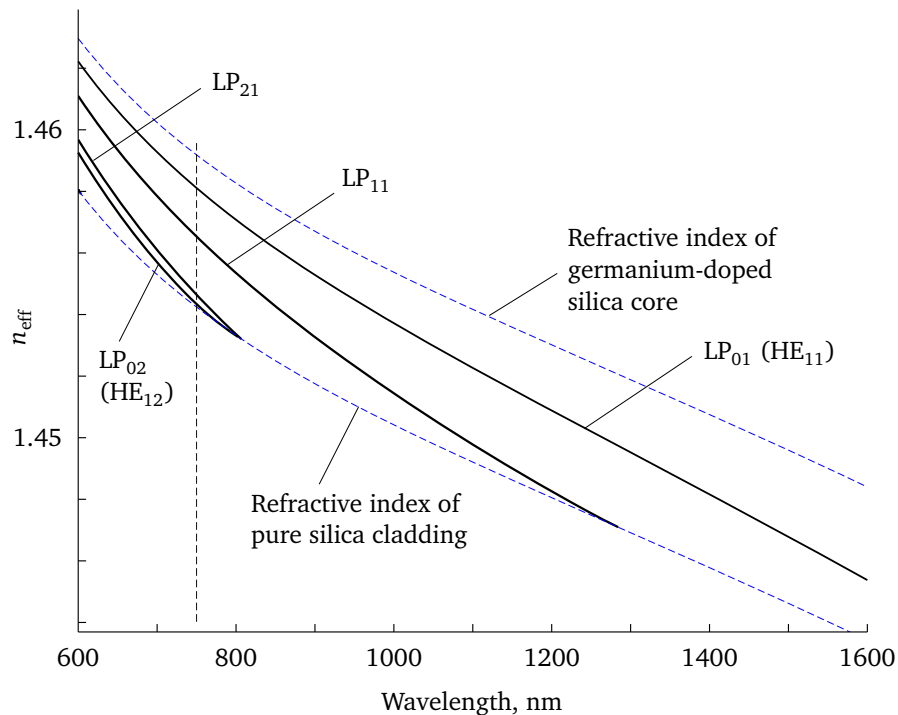


**Figure 2.3:** Mode dispersion in an untapered SMF-28 fibre. The four solid curves correspond to the four modes shown in Fig. 1.4. The vertical dashed line corresponds to the wavelength of 750 nm for which Fig. 1.4 was calculated. The dashed curves denote the material refractive index of the core and the cladding. Note that unlike in Fig. 2.1(a) plotted for the air cladding, here the cladding refractive index depends on the wavelength.

### 2.3.1.2 OMF waist

OMF samples are produced in such a way that the core-cladding structure of the fibre is continuously maintained, down to the sub-micrometre diameter of the cladding. As the result, in the waist a sample has the same core/cladding diameter ratio as it was in the original fibre.

The waist of our samples is always produced from single-mode commercial fibres, which have a typical core diameter of about  $4\dots5\text{ }\mu\text{m}$ . Thus the core/cladding diameter ratio is about 1/25. The waist diameter of the samples usually ranges from 0.5 to 3 wavelengths, depending on the application. Therefore the core diameter in the waist ( $\sim 20\dots100\text{ nm}$ ) is much smaller than the wavelength of light ( $\sim 700\dots1500\text{ nm}$ ). Taking also into account that the refractive indices of the core and the cladding are almost equal, the core in the waist region plays no role in light guidance. Light is guided by the total internal reflection at the cladding-surrounding interface (*cladding-guidance*.) Therefore, the calculation of the waist modes can be performed using the same two-layer

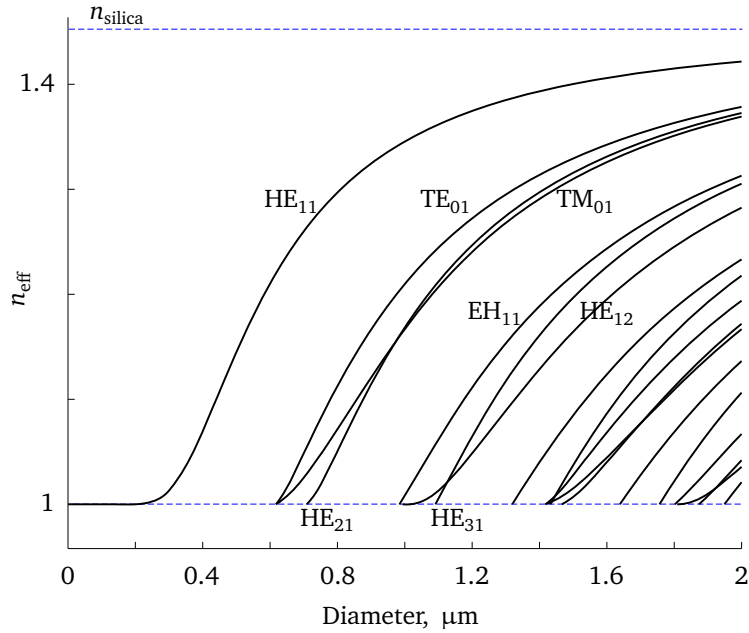


**Figure 2.4:** Mode dispersion in the OMF waist. (Silica in air, 850 nm.)

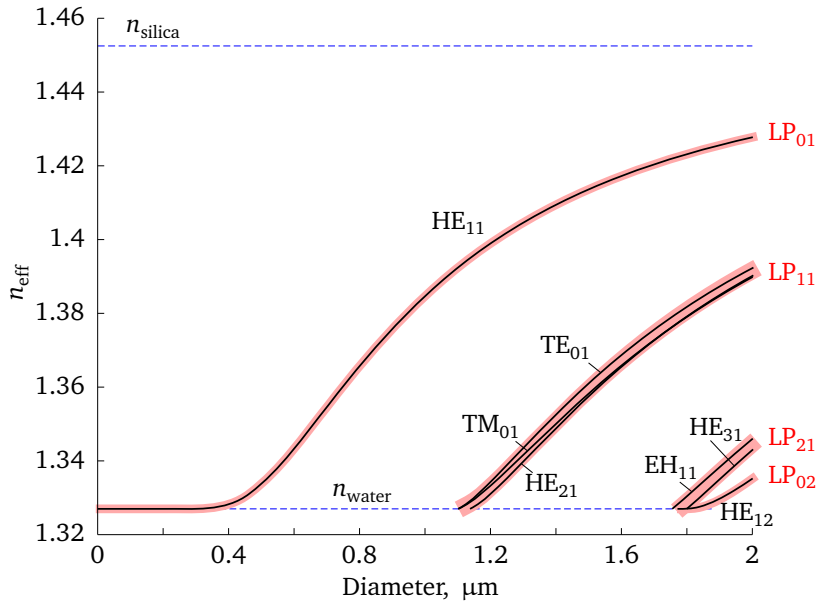
model as the one used for the unprocessed thick fibre, with the cladding playing the role of the core and the surrounding medium working as an infinite cladding.\*

Figure 2.4 shows the dependence of the effective refractive index of different guided modes in the waist depending on its diameter. The effective refractive index of all guided modes lies between the material refractive indices of the cladding (fused silica,  $n_{\text{clad}} = 1.452$ ) and the surrounding (air,  $n = 1$ ). With increasing diameter, all modes tend to “fit” inside the waveguide, and thus their effective refractive index approaches  $n_{\text{clad}}$ . And vice versa, for a very thin waveguide, the mode propagates more or less in air, and therefore its effective refractive index approaches unity.

Due to a high refractive index step at the cladding-air interface, a relatively thin fibre of 2  $\mu\text{m}$  diameter supports a lot of modes (compare to just four modes guided at 600 nm by an SMF-28 fibre, which has an 8  $\mu\text{m}$  core, Fig. 2.3). As the diameter decreases, the modes experience the cut-off. Below the diameter of 0.6  $\mu\text{m}$ , the waveguide is single-mode, i. e. the only mode that can be guided is the fundamental  $\text{HE}_{11}$  mode.

Consider also the three modes, which experience the cut-off just above 0.6  $\mu\text{m}$  ( $\text{TE}_{01}$ ,  $\text{TM}_{01}$ ,  $\text{HE}_{21}$ ). In a weakly guiding fibre, they are degenerate in the propagation constant and correspond to a single  $\text{LP}_{11}$  mode. However in a strongly

\*I have compared the calculation results obtained with such two-layer and the full three-layer—core-cladding-surrounding—models: This simplification for the waist does not introduce any noticeable error.



**Figure 2.5:** Mode dispersion in the waist immersed in water. Due to the small refractive index step between silica and water, the modes are almost degenerate in  $n_{\text{eff}}$ , unlike in Fig. 2.4. Pink curves indicate the correspondence between the HE/EH/TE/TM and LP modes. (Silica in water, 850 nm.)

guiding fibre they are not degenerate any more, and the three curves are clearly distinct. The same happens with the EH<sub>11</sub> and HE<sub>31</sub> modes corresponding to the LP<sub>21</sub> mode.

For comparison, Fig. 2.5 shows the very same diagram but this time the fibre is immersed in water. The refractive index step between water ( $n = 1.327$ ) and silica ( $n = 1.452$ ) is much smaller than the step between silica and air. Therefore the waist in water is not “so strongly” guiding, and the dispersion curves come closer to each other. Pink curves mark the correspondence between the HE/EH/TE/TM and LP modes.

In the rest of this thesis, I will use the vector mode notation (HE, EH, TE, TM) when talking about individual modes independently from the LP-approximation validity (so for both the weak- and the strong-guidance cases). I will use the LP-notation only where I need to emphasize that the solution is obtained in the scalar approximation.

### 2.3.2 Taper regions—three-layer model

Using the equations from the previous section, we can calculate any needed parameters of the light modes propagating in the untapered parts and in the waist. Now we connect these regions.

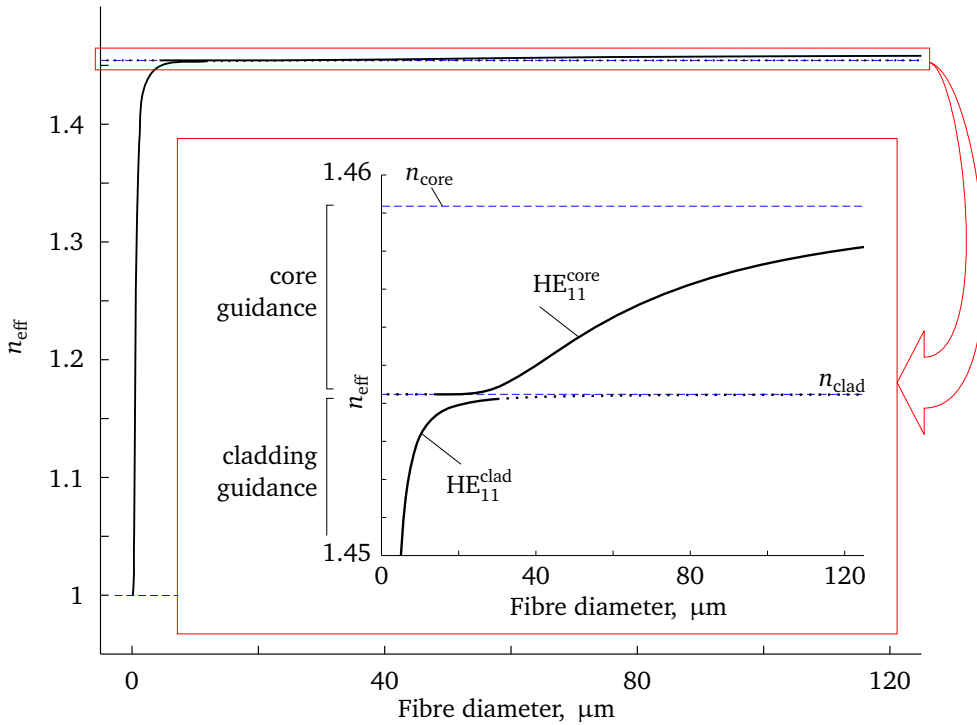


**Figure 2.6:** Mode dispersion in pigtails and in the waist. The two-layer solution fails near  $n_{\text{eff}} = n_{\text{clad}}$ .

To illustrate the task, let's consider the plot  $n_{\text{eff}}$  vs. fibre diameter for the fundamental  $\text{HE}_{11}$  mode, calculated using Eq. (2.3) for the thick part and for the waist (Fig. 2.6).<sup>\*</sup> On the left end of the diagram, the fibre diameter is so small that the core plays no role in the light guidance. The effective refractive index lies between the material indices of the cladding and the surrounding. On the right side, to the contrary, the fibre is so thick that light remains confined by the core and is not influenced by the fibre surrounding. Its effective refractive index is determined by the indices of the core and the cladding. The two-layer model is applicable in both of these cases.

However between these two regions the two-layer model fails. In Fig. 2.6, the curves of the core- and cladding-guided modes do not meet. The effective refractive index of the core-guided mode is always above the material refractive index of the cladding  $n_{\text{clad}}$ , while the  $n_{\text{eff}}$  of the cladding-guided mode is always below it. The reason for this fault of the two-layer models is the following. When we go from left to right and approach the fibre (cladding) diameter of

<sup>\*</sup>The EVEs are derived for a cylindrical, translation invariant (along  $z$ ) waveguide. Therefore, strictly speaking, they cannot be applied to a waveguide with the varying diameter. However, provided that the diameter variation with  $z$  is slow enough, this solution is still valid. This was shown by comparing the theory with the experiment for taper angles up to at least 100 mrad [29].

about  $20\dots 30\text{ }\mu\text{m}$ , the core diameter increases to a value, comparable to the light wavelength (about  $1\text{ }\mu\text{m}$ ). So we cannot ignore the core any more. At the same time, the fibre diameter is still small enough for the evanescent field around the core to reach the surface of the cladding. Therefore we should take into account all three layers: the core, the cladding, and the surrounding of the fibre.

### 2.3.2.1 Mathematical model

The mathematical model for the three-layer system is not as well-known as the two-layer one. The derivation of the two-layer eigenvalue equation is quite long and cumbersome [30, 33], and the one for three layers is almost unreasonably hard. That's why, to the best of my knowledge, the groups working in the field of tapered optical microfibres have been either using the full numerical calculation [34, 35] or significantly simplifying the task and using approximations [36].

Still, the eigenvalue equations for the three-layer system were published several times by researchers involved in fibre sensors [37–43], the first papers dating back to the 1980s. Unfortunately, these papers have remained more or less unnoticed. Even within this series of publications, the work done in 1982 by Monerie [38] is basically repeated in 1994 by Henry [40]. Just a few weeks ago yet another publication appeared, again deriving what Monerie published thirty years ago [44]. This can be partly explained by the fact that information, that a paper deals with the three-layer model, is not always “visible” from the abstract or the title and thus is not always found when people need it. Also, for some unfortunate coincidence, the most important of these papers, were not, until recently, returned by the search engines of the publishers.

There is also another severe problem: most of these publications contain typos. Taking into account that a full set of equations needed to calculate vector modes takes about five pages [41, 43], it is practically impossible to spot a mistake, not only for the reader but also for the authors. It is also very difficult to simply program all these equations without introducing further mistakes. Therefore it took quite some time to implement the working three-layer model, and I will shortly describe it here.

### 2.3.2.2 Implementation

The first publication I was able to find was the English translation of a Russian paper back to 1976 [37]. The authors give the exact equations for the electric and magnetic fields, however they derive the eigenvalue equation only in the approximation of a small refractive index step (weak guidance). This approximation is valid for the core-cladding interface, where the refractive index step is on the order of 0.5 %, and is therefore of interest for the so called double-cladding fibres. In 1982, the results for weakly guiding three-layer fibres, in a somewhat simpler, easier to use form, were published by Monerie [38]; I implemented his equations in our toolbox [2].

The Monerie solution cannot be used in the tapers and in the waist, because of the high refractive index step at the outer OMF surface (cladding-surrounding). The first accessible publication with the exact three-layer eigenvalue equation is the one by Tsao et al. from 1989 [39]. This paper contains the eigenvalue equation for the HE and EH modes as well as for the simpler TE and TM modes. Unfortunately, the authors did not try to solve the derived equation for the hybrid modes themselves (having explained it by the complexity of the required numeric calculations) and have used the equations for the TE mode in the examples. I have programmed all the equations from the paper but the one for the HE/EH mode does not have any roots.\* Probably it is due to a typo in the paper or even a mistake in the derivation [46].

In 1997, Erdogan again publishes the eigenvalue equation for the hybrid modes [41]. He follows the Tsao approach and derives an equation for the cladding-guided modes. There were several typos in the published paper, and in 2000 the errata were published [42].

Thus, we have a working three-layer solution for each part of OMF:

Mode type	$n_{\text{eff}}$	Solution	Figure
HE/EH	$< n_{\text{clad}}$	Erdogan	2.7(a)
HE/EH	$> n_{\text{clad}}$	Monerie	2.7(b)
TE/TM	both	Tsao	2.8

Figure 2.7 shows the vector two-layer, Erdogan, and Monerie solutions in the (a) waist and (b) in the taper. Figure 2.8 shows the solutions for the TE and TM modes.

---

\*The same result was then received independently by T. Lee from ORC in Southampton [45].

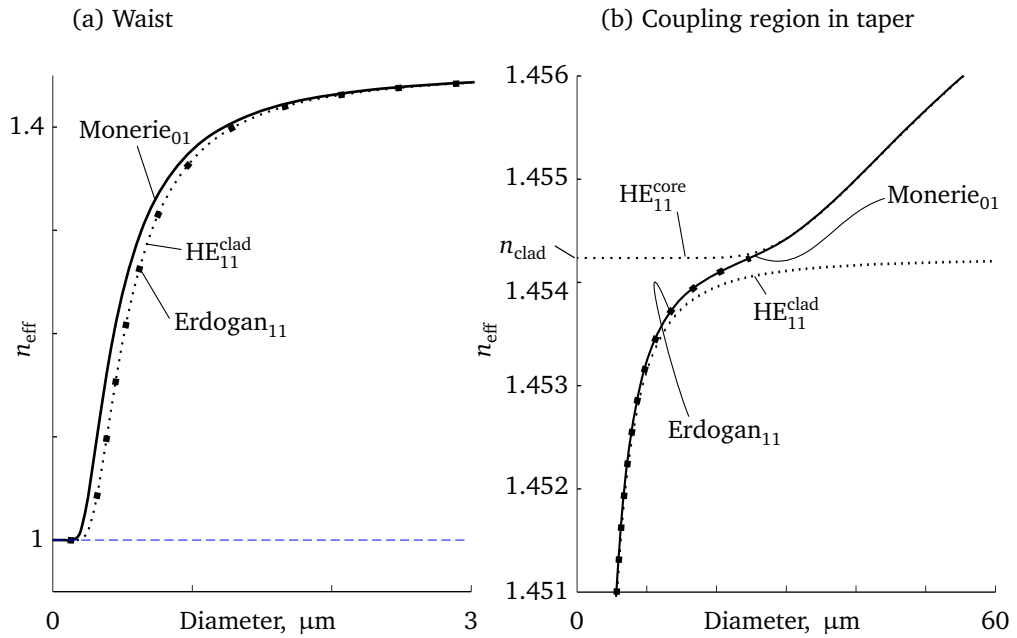


**Figure 2.7:** Vector two-layer (thin dotted line) and Erdogan (thick dotted) solutions for HE<sub>11</sub> mode and Monerie solution for LP<sub>01</sub> mode (solid). (a) In the waist, where the refractive index step is high and the fibre is strongly guiding, the scalar Monerie solution strongly deviates from the vector solutions. The Erdogan solution here matches the two-layer vector solution. (b) In the thick part of a sample, the fibre is weakly guiding: the field is mostly confined inside the fibre and the refractive index step “seen” by the field is the small core-cladding step. Therefore the scalar Monerie solution (solid line) matches the two-layer vector solutions (thin dotted) above and below  $n_{\text{clad}}$  and closes the gap between them near  $n_{\text{clad}}$ . In this weak guidance regime, the Erdogan solution (thick dots) matches the Monerie solution but only works in the cladding-guidance regime ( $n_{\text{eff}} \leq n_{\text{clad}}$ ). (SMF-28 fibre, 750 nm.)

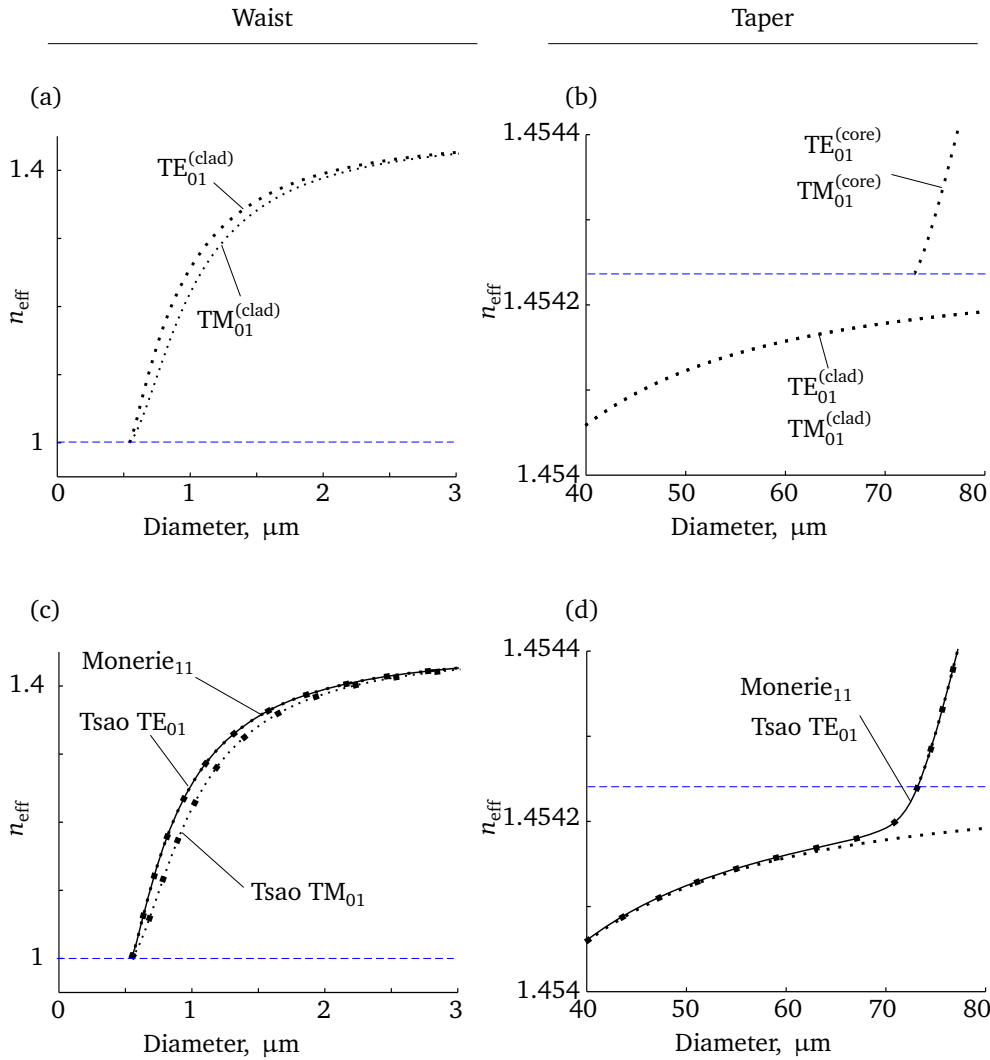


**Figure 2.8:** Two-layer and Tsao solutions for  $\text{TE}_{01}$  and  $\text{TM}_{01}$  modes and Monerie solution for  $\text{LP}_{11}$  mode. (a), (b) Two-layer models in the waist and in the taper. (c), (d) Three-layer models in comparison to the two-layer models. (SMF-28 fibre, 750 nm.)

### 2.3.3 Choosing right model for each OMF region

Figure 2.9 and Tab. A.1 on page 106 summarize the applicability of different models for each OMF region. For the hybrid modes, as long as the fibre diameter is large enough and  $n_{\text{eff}} > n_{\text{clad}}$ , the weak guidance approximation is valid and we can use the Monerie solution. With decrease of the fibre diameter, the mode guidance changes to the cladding guidance ( $n_{\text{eff}} < n_{\text{clad}}$ ) and we can switch to the Erdogan solution. The mismatch between the two solutions at the border point ( $n_{\text{eff}} = n_{\text{clad}}$ ) is less than  $10^{-6}$ ; this is a cross-check of the Monerie and Erdogan solutions in the gap, where they have deviated from the two-layer solutions. For the TE and TM modes, we can use the Tsao solution both in the core- and the cladding-guidance regimes.

Note that although the three-layer solutions work fine not only in the tapers but also in the waist and in the untapered fibre, it makes sense to use the much simpler two-layer solutions there, for the sake of performance.

For eigenvalue and field formulae for all models, see appendix A.

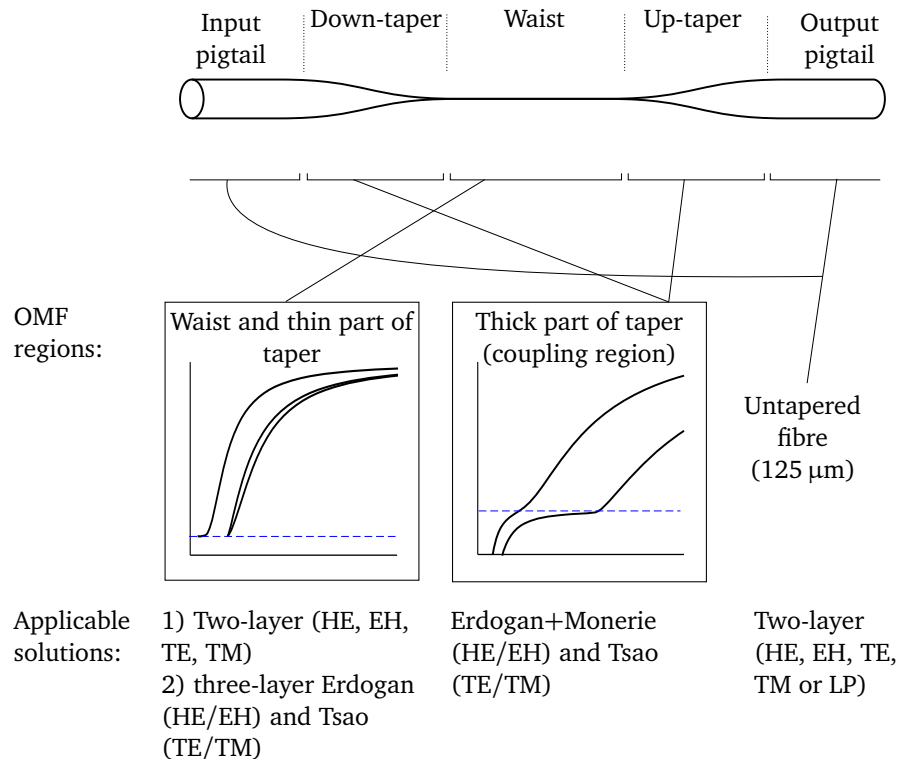


**Figure 2.9:** Mathematical models for different OMF parts.

### 2.3.4 Mode coupling

The theory explained until now is sufficient to calculate the parameters of the guided modes in an OMF at any given diameter. If we consider the actual propagation of a wave along an OMF, we can face two different cases. One is the adiabatic mode propagation, when the power within a given mode is conserved along the whole OMF. For SOMMI, we are interested in another one—the non-adiabatic propagation—when the HE<sub>11</sub> mode of the input pigtail is split into the HE<sub>11</sub> and HE<sub>12</sub> modes in the down-taper. This splitting (and recombination in the up-taper) is governed by mode coupling.

Calculation of mode coupling can be done based on the coupled local mode theory [30, Chap. 28]. The pre-requisite for applicability of this theory is that the parameters of the waveguide (e.g. the fibre diameter) do not change rapidly along the fibre. As shown in [25, 29], mode coupling in tapers as steep as 160 mrad can be adequately modelled using this approach. In our experiments, tapers had a slope of 1...60 mrad, so this model should work as well.

#### 2.3.4.1 Coupling equations

Mode coupling means that the power and the phase of one mode depends on those of the other modes. The exact field  $\mathbf{E}(x, y, z)$  in the fibre can be written in the form

$$\begin{aligned}\mathbf{E}(x, y, z) &= \sum_j [b_j(z) + b_{-j}(z)] \mathbf{e}_j(x, y, \beta_j(z)), \\ \mathbf{H}(x, y, z) &= \sum_j [b_j(z) + b_{-j}(z)] \mathbf{h}_j(x, y, \beta_j(z)),\end{aligned}$$

where  $\mathbf{e}$  and  $\mathbf{h}$  are the normalized amplitudes of the individual orthogonal modes,  $j$  the mode number (among all modes considered),  $\beta_j(z)$  the local mode propagation constant. Since the fibre parameters vary with  $z$ , the propagation constant  $\beta$  also depends on  $z$ . The complex factors  $b$  describe the amplitude and the phase of the forward ( $b_{+j}$ ) and backward ( $b_{-j}$ ) propagating modes, in each point along the fibre axis  $z$ , i.e.

$$b_{\pm j}(z) = a_{\pm j}(z) \exp \left[ \pm i \int_0^z \beta_j(z) dz \right],$$

where  $a$  is the amplitude.

The equations for  $b_j(z)$  can be derived by substituting Eqs. (2.6) into Maxwell's equations [30, Chap. 31 and Eq. (28-2)]:

$$\begin{aligned}\frac{db_j}{dz} - i\beta_j b_j &= \sum_l [C_{jl} b_l + C_{j,-l} b_{-l}], \\ \frac{db_{-j}}{dz} - i\beta_j b_{-j} &= \sum_l [C_{-j,l} b_l + C_{-j,-l} b_{-l}],\end{aligned}$$

where  $C_{jl}$  are the coupling coefficients [30, Eq. (28-4)]

$$C_{jl} = \frac{k}{4} \sqrt{\frac{\epsilon_0}{\mu_0}} \frac{1}{\beta_j - \beta_l} \int_{A_\infty} \mathbf{e}_j^* \cdot \mathbf{e}_l \frac{\partial n^2}{\partial z} dA, \quad j \neq l, \quad C_{jj} = 0, \quad (2.7)$$

and  $A_\infty$  is the infinite cross-section.

By definition, if there is no coupling to the backwards propagating modes (no reflection in the fibre),  $C_{j,-l} = 0$  and  $C_{-j,l} = 0$  for any  $j$  and  $l$ . Furthermore, since in a SOMMI only two modes—HE<sub>11</sub> and HE<sub>12</sub>—are excited, we end up with a system of just two differential equations:

$$\frac{db_1}{dz} - i\beta_1 b_1 = C_{12} b_2, \quad (2.8a)$$

$$\frac{db_2}{dz} - i\beta_2 b_2 = C_{21} b_1. \quad (2.8b)$$

### 2.3.4.2 Coupling coefficients $C$

In this work I consider only the step-index fibres, so the refractive index is constant within the core and within the cladding and changes only at the interface. Thus  $\partial n^2 / \partial z$  in Eq. (2.7) equals zero everywhere except at the core-cladding and cladding-surrounding interfaces. If we ignore the cladding-surrounding interface (because the evanescent field of the low-order modes in the surrounding region at the diameters, at which the coupling occurs, is very small\*), we can consider the cladding to be infinitely large and describe the fibre as [30, Eq. (28-11)]:

$$n^2(r, z) = n_{co}^2 [1 - 2\Delta H(r - \rho(z))],$$

or, alternatively, as

$$\frac{1}{n^2(r, z)} = \frac{1}{n_{co}^2} \left[ 1 + \frac{2\Delta}{1 - 2\Delta} H(r - \rho(z)) \right],$$

where  $\Delta = (n_{co}^2 - n_{cl}^2)/2n_{co}^2$  is the so called fibre profile height parameter,  $2\rho(z)$  the  $z$ -dependent fibre core diameter,  $H$  the Heaviside step function ( $H(x) = 1$  if  $x > 0$ ,  $H(x) = 0$  otherwise). The integrand in Eq. (2.7) can be written as

$$\mathbf{e}_j^* \mathbf{e}_l \frac{\partial n^2}{\partial z} = \left( e_{\phi j}^* e_{\phi l} + e_{zj}^* e_{zl} \right) \frac{\partial n^2}{\partial z} - \left( n^2 e_{rj}^* \right) \left( n^2 e_{rl} \right) \frac{\partial}{\partial z} \left( \frac{1}{n^2} \right).$$

(Note that  $e_\phi$ ,  $e_z$  and  $n^2 e_r$  are continuous across the interface, unlike  $e_r$ .) Finally, with

$$\frac{\partial n^2}{\partial z} = -2n_{co}^2 \Delta \delta(r - \rho) \frac{d\rho}{dz}$$

---

\*Taking into account a very good matching of the theoretical and experimental results obtained with this theory [25, 29], this assumption does not introduce any significant error.

and

$$\frac{\partial}{\partial z} \left( \frac{1}{n^2} \right) = \frac{2n_{co}^2 \Delta}{n_{co}^2 n_{cl}^2} \delta(r - \rho) \frac{d\rho}{dz},$$

we obtain from Eq. (2.7)

$$C_{jl} = -\frac{k}{2} \sqrt{\frac{\epsilon_0}{\mu_0}} \frac{n_{co}^2 \Delta}{\beta_j - \beta_l} \frac{\rho d\rho}{dz} \times \int_0^{2\pi} \left[ e_{\phi j}^{c.c.} e_{\phi l} + e_{zj}^{c.c.} e_{zl} + \left( \frac{n^2}{n_{co}^2} e_{rj}^{c.c.} \right) \left( \frac{n^2}{n_{cl}^2} e_{rl} \right) \right]_{r=\rho(z)} d\phi, \quad j \neq l. \quad (2.9)$$

If  $\Delta$  is very small ( $\ll 1$ ), we have the case of a weakly guiding fibre, the longitudinal field components  $e_z$  vanish, the transverse components  $e_r$  and  $e_\phi$  are both continuous across the interface, and the last equation can be rewritten as [30, Eq. (28-13)]

$$C_{jl} = \frac{k}{2} \sqrt{\frac{\epsilon_0}{\mu_0}} \frac{n_{co}^2 \Delta}{\beta_j - \beta_l} \frac{\rho d\rho}{dz} \int_0^{2\pi} (\mathbf{e}_{tj} \cdot \mathbf{e}_{tl})_{r=\rho(z)} d\phi, \quad j \neq l, \quad (2.10)$$

where the subscript  $t$  means “transverse”.

### 2.3.4.3 Coupling calculation

To calculate the coupling coefficients according to Eq. (2.9) or (2.10), we should use the three-layer model described in Sec. 2.3.2. The two-layer model cannot correctly describe the mode field behaviour when the effective refractive index of a mode gets close to the refractive index of the cladding material.

In practice, we need mode coupling calculation to design an optimal taper shape: to split power between the HE<sub>11</sub> and HE<sub>12</sub> modes in the 1:1 ratio to maximize interference contrast. Equations (2.8) should be solved numerically and, to achieve appropriate accuracy, it takes many hours. Although I have created the first draft of the corresponding code, I have not had time to debug it yet. Therefore I do not give the simulation results for mode coupling here. On the other hand, as will be explained in chapter 3, the reproducibility of our manufacturing procedure is not very high and leads to a different OMF shape each time a sample is pulled. Therefore it does not make much sense to numerically optimize the taper shape with a high precision. Instead, the tapers were designed using the approximate critical angle theory and tested interferometrically. Of course, in the future the manufacturing reproducibility should be improved and the optimal shape found theoretically and verified experimentally.

### 2.3.5 Critical angle theory

To design the tapers, a nice practical solution is provided by the critical angle theory [25, 47].

A critical angle is a taper slope angle, which approximately defines the borderline between the regions of coupling and no coupling of two chosen modes. That means that if the local taper slope  $\Omega$  is much less than the critical angle  $\Omega_{\text{critical}}$  calculated for two specific modes, there will be no coupling between these modes at this point; if  $\Omega \gg \Omega_{\text{critical}}$ , the modes are coupled. The value of  $\Omega_{\text{critical}}$  is derived from the length-scale criterion—an assumption, that if the taper is (locally) much longer than the beat length between the two modes, there will be no coupling between them. From this follows the condition [25, Eq. (4)]

$$\Omega_{\text{critical}}(z) = \frac{d(z)}{2} \frac{\Delta\beta(d)}{2\pi} = \frac{d(z)}{2} \frac{\Delta n_{\text{eff}}(d)}{\lambda},$$

where  $\Delta\beta$  is the propagation constant difference between the two modes,  $\Delta n_{\text{eff}}$  the corresponding effective refractive index difference,  $d$  the local taper (fibre cladding) diameter,  $\lambda$  the vacuum wavelength. Since  $n_{\text{eff}}$  depends on the local fibre diameter, which changes along the taper, we end up with a delineating curve for each couple of modes. Figure 2.10 shows such curves for the three lowest  $\text{HE}_{1m}$  modes. The details on how this diagram is used for actual sample design will be given in chapter 3.

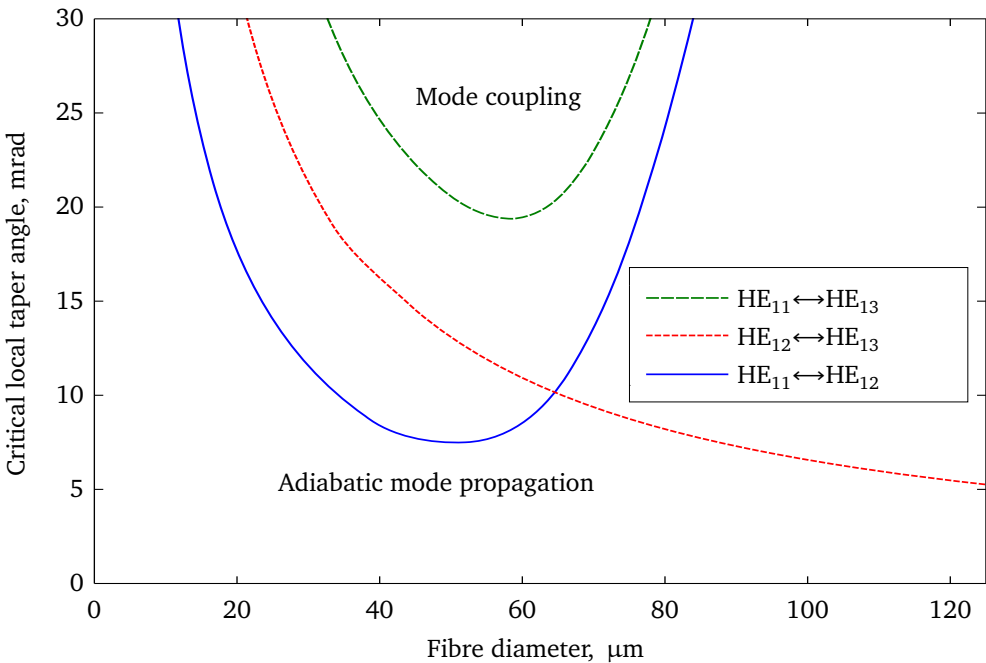


**Figure 2.10:** The delineating curves show the local taper angle required to avoid or achieve coupling between two modes: adiabaticity within the corresponding couple of modes is observed if the angle value is much below the curve. (SM800 fibre in air, 850 nm.)

## 2.4 Computer implementation—Optical Fibre Toolbox (OFT)

The computer realization of the above models should be able to perform, basically, two tasks:

- find the guided modes, i. e. find out how many roots the corresponding EVE has in total for a given configuration and determine all these roots;
- “trace” each modal curve  $n_{\text{eff}}$  vs.  $d$  or  $\lambda$  within a given range of diameters or wavelengths.

Several aspects of this problem are to be taken into account. The EVEs can only be solved numerically, and therefore, having found a root, the program cannot determine, to which mode it corresponds until all guided modes have been found. At the same time, the program does not know in advance how many roots there should be in total, so it should somehow make sure it has not missed any. Finally, in some areas the modal curves lie very close to each other. Special care should be taken to avoid numerical hops from one curve to another during tracing. All these issues were successfully resolved and a fast adaptive algorithm was created. The main ideas are described in appendix B. The whole procedure was realized as the Optical Fibre Toolbox for Matlab (OFT) [2]. Our experience of more than three years of regular use of this code shows that it is sufficiently robust and applicable in the real working conditions.

### 2.4.1 What OFT can do

OFT’s basic functionality allows finding guided modes of a given fibre within a given range of parameters (wavelength or fibre diameter) and trace the dispersion curves for hybrid, TE and TM modes of two-layer step-index fibres as well as the modes of the three-layer structures according to the Monerie, Erdogan and Tsao solutions.

The toolbox can also calculate field distributions ( $E$  and  $H$ ) and the amount of power guided inside the fibre and in the evanescent field. It can also automatically find phase-matching points in multiple-harmonic dispersion diagrams.

### 2.4.2 Example: Application to diameter measurement based on harmonic generation

To give an example of practical use of OFT, I briefly describe here its application in our microfibre diameter measurement method. The physical principles and experimental part of the method are described in detail in [1].

Light, coupled into the untapered end of a sample, is guided mainly in the core, which has a diameter of about  $5 \mu\text{m}$ . The waist of some of our samples is as small as  $0.5 \mu\text{m}$  in diameter, i. e. 10 times smaller. Therefore, when the

mode gets from the thick part into the waist, it gets transversely compressed by a factor of about 100. Accordingly, its intensity increases by a factor of 100. This leads to efficient nonlinear interaction between light and the material of the fibre in the waist—fused silica. Fused silica has a small third-order nonlinearity [48]. Therefore third-harmonic light is generated as the wave propagates through the waist.

Moreover, despite the inversion symmetry of bulk fused silica, which results in  $\chi_{(2)} = 0$ , second-harmonic generation was observed even in untapered fibres [49]. It can be explained by breaking the symmetry at the defects in the fibre [50, p. 367]. In OMFs, with their high light intensity at the surface, the surface effect plays a significant role too [50, p. 344].

In order for the harmonic generation process to be effective, the phase-matching condition should be fulfilled. This means, that the phase velocities of the initial (pump) and third-harmonic waves should be equal or, equivalently,

$$n_{\text{eff},\omega} = n_{\text{eff},3\omega}. \quad (2.11)$$

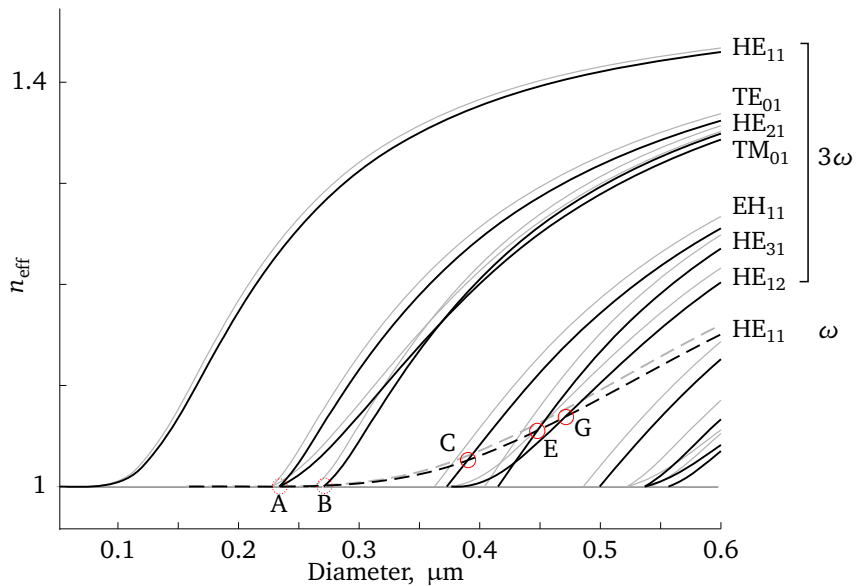
In a bulk isotropic material, this is never the case due to material dispersion: refractive indices of the same material at different frequencies are different. However, the modal dispersion of the fibre modes can compensate this effect.

Figure 2.11 shows the modal dispersion  $n_{\text{eff}}(d)$  diagram for the pump and the third harmonic. Clearly, the curves of the fundamental HE<sub>11</sub> modes of the  $\omega$  and  $3\omega$  waves do not intersect, so there is no chance of fulfilling condition (2.11). However, the curve of the fundamental mode of the pump wavelength does intersect those of the higher third-harmonic modes (points A, B etc.). Thus if the fibre diameter is equal, for example, to  $d_C$ , the second harmonic *can* in fact be generated.

If the pump wavelength is different, the modal diagram looks similar but the curves are all slightly shifted (gray curves in Fig. 2.11). Therefore the phase-matching condition is also fulfilled at slightly different fibre diameter values. This is shown graphically in Fig. 2.12. We can thus conclude, that efficient second-harmonic generation can only occur, if the fibre diameter matches in a special way the pump wavelength.

Our measurement technique is then very simple. We take a sample that should be measured, couple light from a tunable laser into it and, while continuously changing the wavelength, observe the signal at the output. The peak of the third-harmonic response occurs when the phase-matching wavelength is reached. Finally, from Fig. 2.12, we determine the fibre diameter.

To plot the phase-matching diagram in Fig. 2.12, the dispersion diagrams should first be plotted for several wavelengths. For a different fibre, these diagrams should be calculated again. Using the OFT, we can build each dispersion diagram and automatically find intersection points within approximately a minute, and thus the whole process becomes fast enough to be used in real work.



**Figure 2.11:** Modal dispersion for pump (dashed line) and third harmonic waves. Black curves: 1000 nm, gray: 975 nm. Waveguide: silica-in-air. Circles mark the automatically found phase-matching points, dotted circles—points with zero overlap.

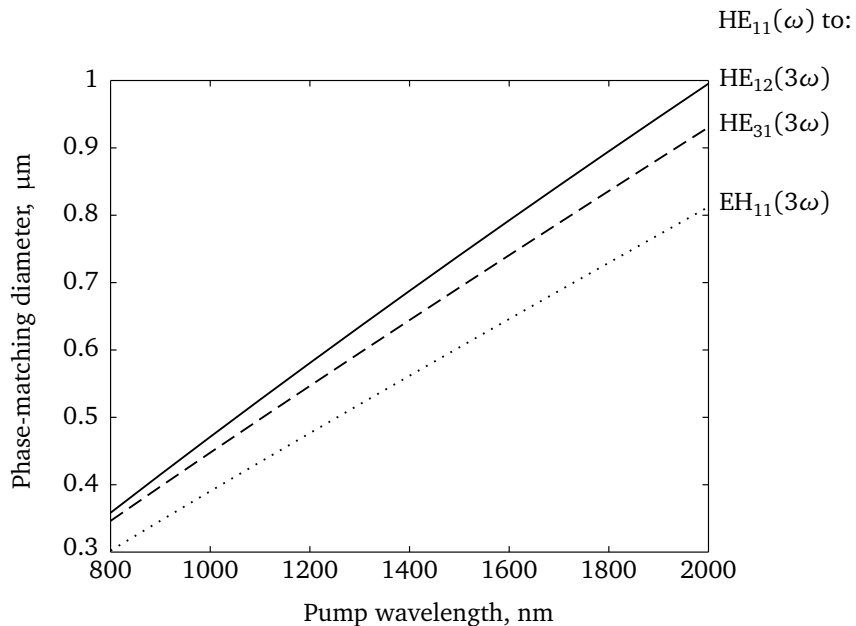


**Figure 2.12:** Phase-matching diameter vs. wavelength for third-harmonic generation. Largest overlap integral is observed for phase-matching between  $\text{HE}_{11}$  mode of the pump light and  $\text{HE}_{12}$  (solid line),  $\text{HE}_{31}$  (dashed) and  $\text{EH}_{11}$  (dotted) modes of the third-harmonic light. (Silica in air.)

## 2.5 SOMMI simulation

With the developed OMF model, we can now proceed to the simulation of a single optical microfibre modal interferometer. The goal of this simulation is to calculate the expected output signal for interferometers of different shape and materials of the fibre core, cladding, and surrounding.

### 2.5.1 Cylinder interferometer

Quick summary of what was said in the previous sections.

SOMMIs have one input port and one output port—the single-mode untapered pigtails of the tapered OMF samples. The two interferometer arms are represented by the two transverse modes propagating between the tapers. The down-taper plays the role of a beam splitter, the up-taper—of a beam recombiner.

Mode splitting is based on mode coupling in abrupt tapers: the power guided into the taper in some mode does not remain in this mode throughout the taper but is coupled to other modes. Due to the symmetry reasons, the  $HE_{11}$  mode of the single-mode pigtails couples only to the modes of the same symmetry ( $HE_{12}$ ,  $HE_{13}$  etc.). By appropriate design of the tapers, it is possible to minimize coupling to the  $HE_{13}$  mode, and thus all power will be split only between the  $HE_{11}$  and  $HE_{12}$  modes.

The pigtails and the waist of an OMF can be treated as cylinders. Tapers have conical shape, but can be approximately represented as a number of short cylinders of different diameters (standard approach to numeric integration). Therefore let's consider a cylindrical waveguide of length  $L$ , in which two modes propagate: 1 and 2. Let these modes have the corresponding effective refractive indices  $n_1$  and  $n_2$ , equal amplitudes  $A = 1$  and the same vacuum wavelength  $\lambda$ . Finally let the original (at the beginning of the cylinder) phases of the modes be  $\varphi_1$  and  $\varphi_2$

At the end of the cylinder, each mode has the phase (cf. Eq. (2.1) on page 16)

$$\frac{2\pi}{\lambda}n_{\text{eff}}L + \varphi - \omega t.$$

The two modes interfere, and the intensity at the output as a function of the wavelength  $\lambda$  and the cylinder length  $L$  is

$$\begin{aligned} I = \langle E^2 \rangle_t &= \left\langle \left[ A \sin \left( \frac{2\pi}{\lambda} L n_2 + \varphi_1 - \omega t \right) + A \sin \left( \frac{2\pi}{\lambda} L n_1 + \varphi_2 - \omega t \right) \right]^2 \right\rangle_t \\ &= \left[ 2A \cos \left( \frac{\pi}{\lambda} L (n_1 - n_2) + \varphi_1 - \varphi_2 \right) \right]^2 \times \\ &\quad \times \left\langle \sin^2 \left( \frac{\pi}{\lambda} L (n_1 + n_2) + \varphi_1 + \varphi_2 - 2\omega t \right) \right\rangle_t \\ &= 4 \cos^2 \left( \frac{\pi}{\lambda} L \Delta n_{\text{eff}} + \Delta \varphi \right) \times 0.5 = \end{aligned}$$

$$= 1 + \cos\left(\frac{2\pi}{\lambda}L\Delta n_{\text{eff}} + \Delta\varphi\right) = 1 + \cos(\phi),$$

or, in the normalized form,

$$I \sim 0.5 + 0.5 \cos(\phi) = 0.5 + 0.5 \cos\left(\frac{2\pi}{\lambda}L\Delta n_{\text{eff}} + \Delta\varphi\right). \quad (2.12)$$

Here  $\phi$  is the phase of the interference signal,  $\Delta n_{\text{eff}}(\lambda, d) = n_1(\lambda, d) - n_2(\lambda, d)$  the difference between the effective refractive indices of the two interfering modes, and  $\Delta\varphi$  the phase difference between them at the beginning of the cylinder. If the mode amplitudes are not equal, the signal will remain of the same shape but the contrast will be reduced.

If we consider interference in just one cylinder and want to know the frequency of the fringes but not the absolute phase (which is usually the case in interferometry), we can assume  $\Delta\varphi = 0$ . If, for numerical calculation, we consider an OMF split into many sequential cylinders, then  $\Delta\varphi$  is the phase difference at the end of the previous cylinder.

Eq. (2.12) is the main equation used in this work to calculate the interference signal.

### 2.5.2 Spectral interferometry

Spectral interferometry assumes a constant SOMMI shape and a variable wavelength, and can be implemented experimentally with a very simple setup: A broadband light source, e. g. a white lamp, is coupled to one pigtail of the sample. A spectral detector, such as a spectrometer or an optical spectrum analyser, is coupled to another pigtail and the intensity vs. wavelength is measured.

The wavelength range should be chosen such that the input and output pigtails remain single-mode: The shortest wavelength in the design range should be above the cut-off of the first higher mode ( $TE_{01}$ ); then only the fundamental  $HE_{11}$  mode will be guided. For example, in Fig. 2.13(a) on the following page, the cut-off of the  $TE_{01}$  mode (belonging to the  $LP_{11}$  bunch) is at 627 nm, so the working spectral range of the interferometer will from 627 nm upwards.

For the interferometer to work, the second interfering mode,  $HE_{12}$ , should be guided through the waist, from the splitting point in the down-taper to the recombination point in the up-taper. The  $HE_{12}$  mode can be guided in the waist up to some cut-off wavelength (in analogy to the cut-off of  $TE_{01}$  in the pigtauls): see Fig. 2.13(b), where the cut-off of the  $HE_{12}$  mode is at 1106 nm. In the up-taper, the two modes will couple and thus recombine, and the  $HE_{11}$  mode will be guided out by the output pigtail. The power left in the  $HE_{12}$  mode after interference will be lost because the output pigtail is single-mode.

To simulate this experiment, we need to calculate Eq. (2.12) for different wavelengths. The wavelength appears in this equation not only directly in  $2\pi/\lambda$  but also in the effective refractive index, through the material and mode dispersion. The wavelength dependence of the effective refractive indices of both

propagating modes and thus the interference signal can be straightforwardly calculated using OFT.

If we ignore the tapers for now, the interference between the  $\text{HE}_{11}$  and  $\text{HE}_{12}$  modes in the waist will result in the output signal (power in the  $\text{HE}_{11}$  mode in the output pigtail) looking as shown in Fig. 2.13(c).

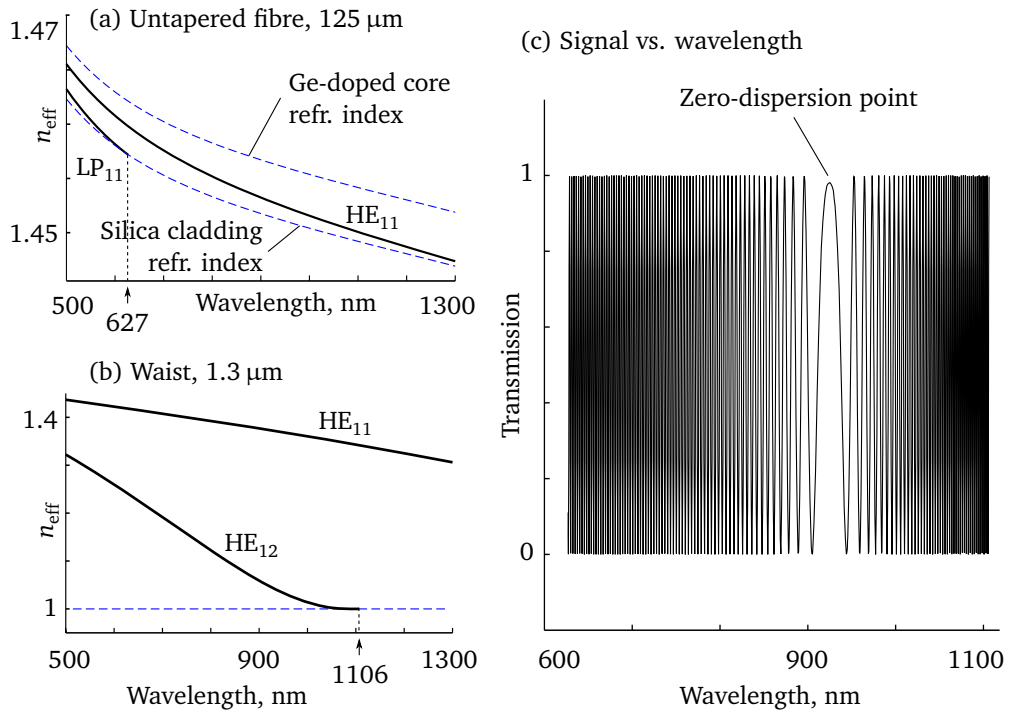


**Figure 2.13:** Theoretical spectral response of a cylinder SOMMI. (a) Guiding properties of the untapered fibre SM800. Fundamental mode  $\text{LP}_{01}$  (weak-guidance analogue of  $\text{HE}_{11}$ ) is guided everywhere, while the first higher mode  $\text{LP}_{11}$  experiences the cut-off at 627 nm. (b) Guiding properties of the 1.3  $\mu\text{m}$  diameter waist. The second interferometer mode  $\text{HE}_{12}$  is cut-off at 1106 nm. (c) Normalized interference signal between 627 and 1106 nm,  $L = 1 \text{ mm}$ .

Note that unlike in a usual white-light interferometer, where the frequency of the fringes remains constant, in a SOMMI it varies strongly due to the strong modal dispersion in the fibre. The signal even exhibits a characteristic zero-dispersion, or achromatic fringe, which was first described for vector modes in tapered fibres by Lacroix et al. [20]. This zero-dispersion point is a very nice feature because it allows for absolute interferometric measurements, just like the achromatic fringe in a usual white-light interferometer. However, unlike in a usual interferometer, here we can nicely observe not only the zero-dispersion fringe, but also many fringes to the left and to the right from it.

### 2.5.2.1 Refractive index sensor

A broadband SOMMI can be used as a refractive index sensor. If all geometrical parameters of the OMF are fixed and only the refractive index of the surrounding medium is changing (for example, by immersing the SOMMI into different liquids), we can calculate the wavelength of the zero-dispersion point vs. the external refractive index. Figure 2.14 shows such dependence for a cylindrical interferometer (tapers ignored). The theoretical sensitivity in this case is  $2500 \dots 5100 \text{ nm/RIU}^*$ . To compare, higher sensitivity for similar sensors has been reported so far only for sensors based on nonlinear processes in photonic crystal fibres or birefringence and requiring very specific specially manufactured fibres [23, 51]. Clearly, to achieve high sensitivity in practice, it is necessary to measure the position of the zero-point very precisely. Therefore it is also interesting that the evolution of the zero-point phase, which is easier to measure, goes at the rate of  $6300 \text{ rad/RIU}$  (at  $n = 1.3$ ) and can be used to measure the relative change of refractive index with even higher precision.

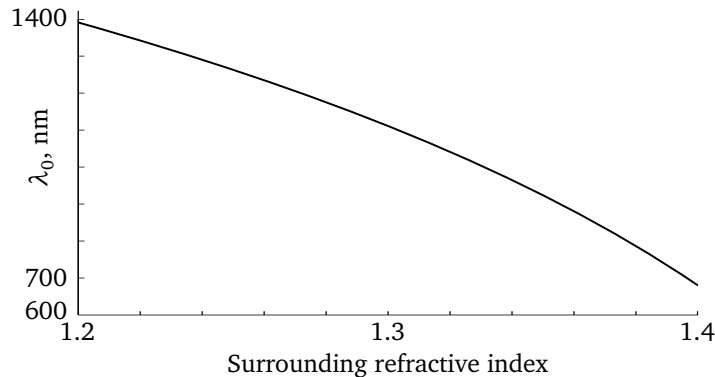


**Figure 2.14:** Zero-point wavelength vs. surrounding refractive index for a cylinder interferometer. Simulated for a silica rod of  $2.5 \mu\text{m}$  diameter in a non-dispersive surrounding.

### 2.5.3 Stretch-interferometry

Another type of interferometry takes place when the wavelength  $\lambda$  is fixed and the length  $L$  between the splitting and recombination points is being changed. This can be experimentally done by using a laser diode as a light source and pulling a sample at two ends. This method was used to test the SOMMI samples after manufacturing.

We assume for now that stretching influences the phase accumulation only along the waist, i. e. we again ignore the tapers.

---

\*Refractive index unit.

When a cylinder waveguide is stretched, three processes occur. First, the path  $L$  travelled by both modes between splitting and recombination increases. Second, due to the Poisson effect, the waveguide gets thinner. Third, due to the photoelastic effect, the material refractive index changes.

The change of  $L$  directly changes the interference result according to Eq. (2.12). The influence of the other two effects requires some closer consideration.

### 2.5.3.1 Poisson effect

If a fibre is stretched by  $\varepsilon = \Delta L/L$ , its contraction in the transverse direction is determined, for a short elongation, by

$$\Delta d = -d\nu\varepsilon$$

or, for larger elongations, by

$$\Delta d = -d \left( 1 - \frac{1}{(1 + \varepsilon)^\nu} \right), \quad (2.13)$$

where  $\nu$  is the fused silica Poisson ratio equal to 0.17 [52–54]. For example, for  $d = 1 \mu\text{m}$ ,  $L = 5 \text{ mm}$ ,  $\Delta L = 50 \mu\text{m}$ , the diameter change is  $\Delta d = -0.0017 \mu\text{m}$ . In OFT, formula (2.13) is used.

The change of the fibre diameter directly leads to the change of  $\Delta n_{\text{eff}}$  according to the mode dispersion diagram (see Fig. 2.1(b) on p. 17) and, since the mode curves  $n_{\text{eff}}(d)$  can be calculated using OFT, the Poisson effect can be readily taken into account.

### 2.5.3.2 Photoelastic effect

Optical fibres, from which our samples are made, are isotropic. A tapered fibre is also isotropic because the slow heat-processing during tapering removes any strain introduced by pulling. However, when a cold fibre is stretched, the axial and transverse refractive indices become different, due to the photoelastic effect. The change in the optical indicatrix is [55]:

$$\Delta \left( \frac{1}{n^2} \right)_i = \sum_{j=1}^6 p_{ij} \epsilon_j,$$

where  $\epsilon$  is the strain vector and  $p_{ij}$  the components of the photoelastic tensor. In the absence of shear,  $\epsilon_4 = \epsilon_5 = \epsilon_6 = 0$ . For stretching in the  $z$ -direction, the strain vector is therefore [56]

$$\epsilon_j = \begin{bmatrix} -\nu\varepsilon \\ -\nu\varepsilon \\ \varepsilon \\ 0 \\ 0 \\ 0 \end{bmatrix}.$$

Therefore we need only to consider the  $i, j = 1, 2, 3$  elements of the strain-optic tensor for a homogeneous isotropic material [55]:

$$p_{ij} = \begin{bmatrix} p_{11} & p_{12} & p_{12} \\ p_{12} & p_{11} & p_{12} \\ p_{12} & p_{12} & p_{11} \end{bmatrix},$$

where  $p_{11} = 0.121$  and  $p_{12} = 0.270$  are the Pockels elastooptic coefficients [54]. Therefore the change in the optical indicatrix is

$$\begin{aligned} \Delta \left( \frac{1}{n^2} \right)_{x,y} &= -\nu \epsilon (p_{11} + p_{12}) + \epsilon p_{12}, \\ \Delta \left( \frac{1}{n^2} \right)_z &= -2\nu \epsilon p_{12} + \epsilon p_{11}. \end{aligned}$$

Taking into account

$$\Delta \left( \frac{1}{n^2} \right)_i = -\frac{2\Delta n_i}{n^3},$$

we obtain

$$\Delta n_{x,y} = -0.5n^3(p_{12} - \nu(p_{11} + p_{12}))\epsilon, \quad (2.14)$$

$$\Delta n_z = -0.5n^3(p_{11} - 2\nu p_{12})\epsilon, \quad (2.15)$$

ending up with two different refractive indices for transverse and axial components of the electric field.

The interfering modes  $\text{HE}_{11}$  and  $\text{HE}_{12}$  are hybrid modes, with the non-vanishing  $z$ -component. Therefore, to calculate their propagation in a stretched cylinder, we have to consider this induced anisotropy. The solution for this problem was derived by Tonning [57] and implemented in OFT (Sec. A.3).

### 2.5.3.3 Simulation algorithm and results

Calculation is performed in the following order:

1. For a given initial interferometer length  $L$  and elongation  $\Delta L$ , using Eq. (2.13), calculate the corrected diameter of the fibre in the stretched state.
2. Using Eq. (2.14) and (2.15), calculate the refractive index correction for the waveguide material in the stretched state.
3. For the new material refractive indices and diameter, calculate  $\Delta n_{\text{eff}}$  for the two interfering modes using the Tonning solution.
4. Calculate the output signal phase  $\phi = (2\pi/\lambda)(L + \Delta L)\Delta n_{\text{eff}}$ .
5. Repeat for the next  $\Delta L$ .

In figure 2.15, the dots correspond to the results of such calculation for a  $\phi 1.5 \mu\text{m} \times 2 \text{ mm}$  waist. All dots in Fig. 2.15(a) lie on a straight line (solid line), which indicates that for small elongation the process is linear. I have also shown the result of calculation with the photoelastic (dotted line) and both effects (dashed line) ignored. Apparently, in this case the photoelastic effect almost compensates the Poisson effect.

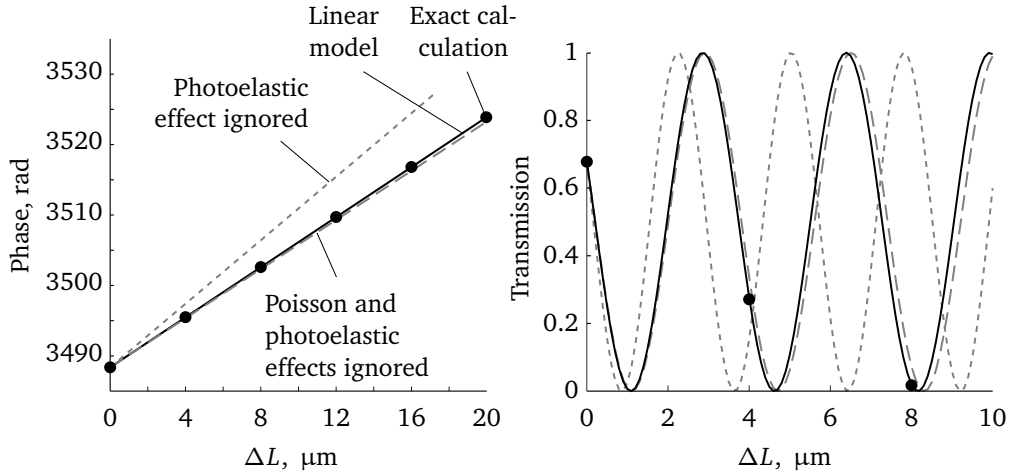


**Figure 2.15:** Simulated stretch-interference signal. Big dots: exact numerical solution with Poisson and photoelastic effects taken into account. Solid line: linear model. Dashed line: Poisson and photoelastic effects are ignored ( $\Delta n_{\text{eff}}$  independent of  $\Delta L$ ). Dotted line: Poisson effect taken into account, photoelastic effect ignored. ( $\phi 1.5 \mu\text{m} \times 2 \text{ mm}$ , fused silica in air, 850 nm.)

For comparison, Fig. 2.16 shows the phase calculated for a thicker waveguide:  $\phi 5 \mu\text{m} \times 2 \text{ mm}$ . In this case, the photoelastic effect is considerably smaller than the Poisson one.

#### 2.5.4 Actual SOMMI shape

Until now, the SOMMI simulation was performed with the tapers ignored. In this section I explain how they are taken into account. I consider the tapers, which are linear everywhere except when the fibre diameter  $d = 2r$  gets so small that the condition

$$\frac{\Omega, \text{ mrad}}{r, \mu\text{m}} < 0.3 \quad (2.16)$$

is violated. ( $\Omega$  is the slope angle.) If it is, then the slope angle is limited by  $\Omega = 0.3r$ , i. e. the slope decreases with the fibre diameter. Equation (2.16) is the limiting condition used by the pulling machine, with which we have produced our samples [58]. It is applied to prevent fluctuations of the sample shape observed otherwise [26]. Figure 2.17 shows such a taper.

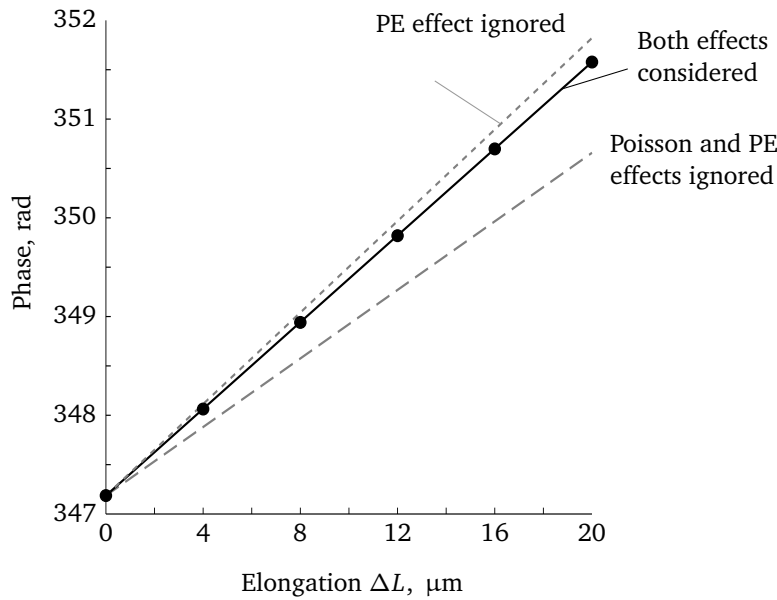


**Figure 2.16:** Simulated stretch-interference signal. Same as Fig. 2.15(a) but for  $\phi 5 \mu\text{m} \times 2 \text{ mm}$ .

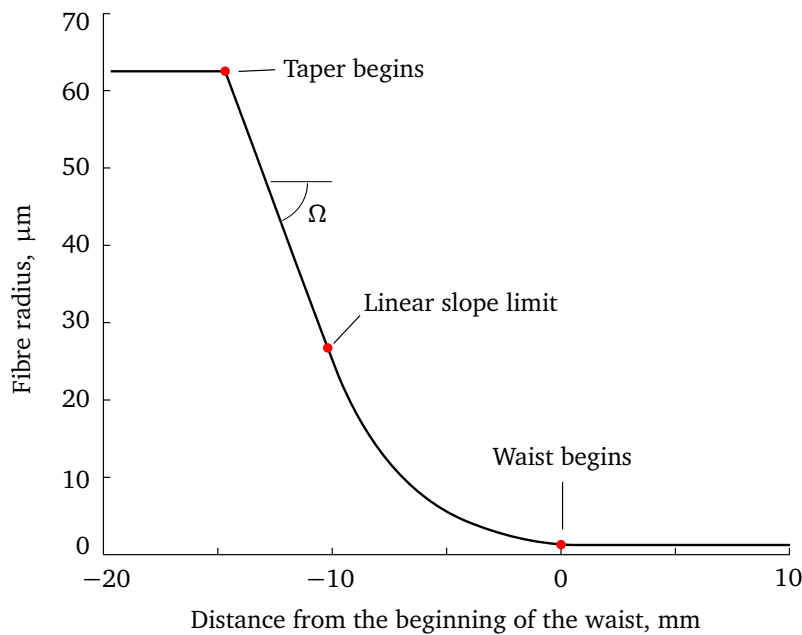


**Figure 2.17:** Linear taper with 8 mrad slope. Dots mark the borders of different regions. The slope limit is reached at the radius of  $26.7 \mu\text{m}$ .

### 2.5.4.1 Numerical approach

To simulate a SOMMI with such a shape, both the variation of the wavelength and of the diameter have to be taken in account. In analogy to Eq. (2.12), the interference signal here is

$$I(\lambda) = \frac{1}{2} + \frac{1}{2} \cos(\phi) = \frac{1}{2} + \frac{1}{2} \cos\left(\frac{2\pi}{\lambda} \int_L \Delta n_{\text{eff}}(\lambda, d(z)) dz\right) \quad (2.17)$$

To calculate Eq. (2.17) numerically, I split the whole tapered fibre into cylindrical sections (Fig. 2.18) with diameters  $d_i$  ( $i$  increases with diameter, and I consider just the down-taper and the first half of the waist, for the symmetry reasons). For each cylinder,  $\Delta n_{\text{eff}}$  is calculated and then multiplied by the length of

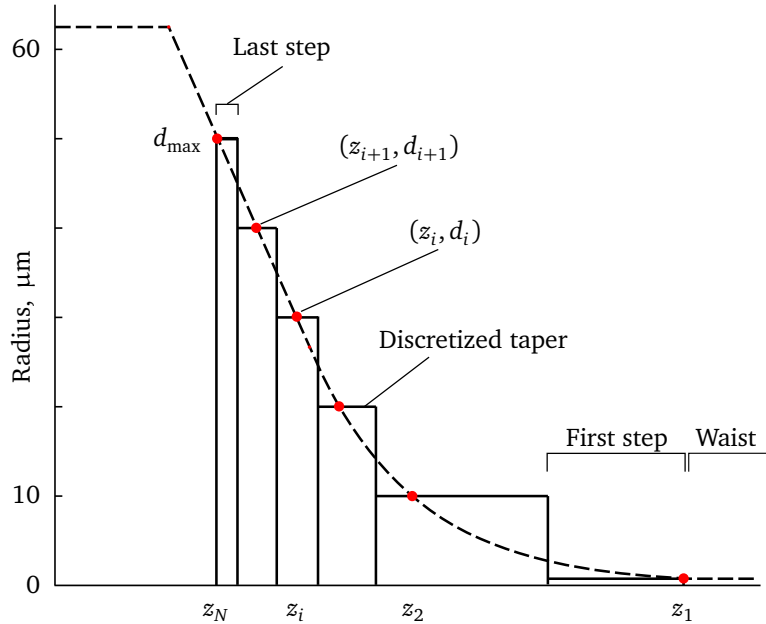


**Figure 2.18:** Discretisation of the taper shape. Discretisation parameters:  $\Delta d = 10 \mu\text{m}$ ,  $d_{\max} = 50 \mu\text{m}$ .

the cylinder. The latter is calculated as follows: for a point  $i$ , the cylinder extends from the center between the points  $i - 1$  and  $i$  to the center between the points  $i$  and  $i + 1$ . Thus for all cylinders except the first and the last ones,

$$\phi_i = \frac{2\pi}{\lambda} \Delta n_{\text{eff}}(d_i) \left( \frac{z_{i-1} + z_i}{2} - \frac{z_i + z_{i+1}}{2} \right) = \frac{2\pi}{\lambda} \Delta n_{\text{eff}}(d_i) \frac{z_{i-1} - z_{i+1}}{2}.$$

For the first cylinder,

$$\phi_1 = \frac{2\pi}{\lambda} \Delta n_{\text{eff}}(d_1) \frac{z_1 - z_2}{2}$$

and for the last one

$$\phi_N = \frac{2\pi}{\lambda} \Delta n_{\text{eff}}(d_N) \frac{z_{N-1} - z_N}{2}.$$

After adding all cylinders up, we obtain

$$\phi = \frac{2\pi}{\lambda} \sum_{i=1}^{N-1} \frac{\Delta n_{\text{eff}}(d_i) + \Delta n_{\text{eff}}(d_{i+1})}{2} (z_i - z_{i+1}), \quad (2.18)$$

where  $N$  is the number of the discretization points. Equation (2.18) is the well-known trapezoidal rule for numerical integration.

This simulation takes hours because, to achieve acceptable precision, we need to calculate mode dispersion for a lot of diameters. This should then be repeated for each surrounding material, in which we may put our samples. And, of course, the calculation should be done anew for each sample shape.

For the spectral interferometry, the process can be sped up if the diameters are chosen in a special way. First, I define a constant diameter discretization step  $\Delta d$  (numerical analysis has shown, that the step of  $0.1 \mu\text{m}$  is sufficient to achieve sufficient accuracy in both the spectral and the stretch-interferometry). Then, I define a discretization grid, which starts at  $d = 0$ , i. e.

$$\frac{d_i}{\Delta d} \text{ is integer.}$$

Finally, I calculate values  $z_i$ , corresponding to these  $d_i$  for the taper shape of a specific sample.

This means that for any sample shape the  $d$ -grid is always the same, and only the cylinder lengths vary. Therefore I can pre-calculate  $\Delta n_{\text{eff}}(\lambda)$  for all points  $d_i$  for each fibre-surrounding material combination and then re-use these values for samples of any shape. The only value which should be calculated for each sample is  $\Delta n_{\text{eff}}(d_{\text{waist}})$ .

For the stretch interferometry, this simple method is not applicable. According to the Hook's law, the relative elongation of each elementary cylinder is proportional to its length and inversely proportional to the area of cross-section. Therefore, since the length of the cylinders is not known a priori, it is impossible to precalculate  $\Delta n_{\text{eff}}$ . However, it is still possible to calculate the  $\Delta n_{\text{eff}}(d, \varepsilon)$  function for many diameters and for many relative elongations and then use a two-dimensional interpolation to find the right  $\Delta n_{\text{eff}}$  for each cylinder after taking the Poisson and photoelastic effects into account. Thus, again, tapers of any shape can be simulated quickly.

#### 2.5.4.2 Optimal $\Delta d$ and $d_{\text{max}}$

**Spectral interferometry** To find an optimal step  $\Delta d$ , I have calculated  $\lambda_0(d_{\text{max}})$  (Fig. 2.19). The resulting value with tapers taken into account (835 nm) is com-

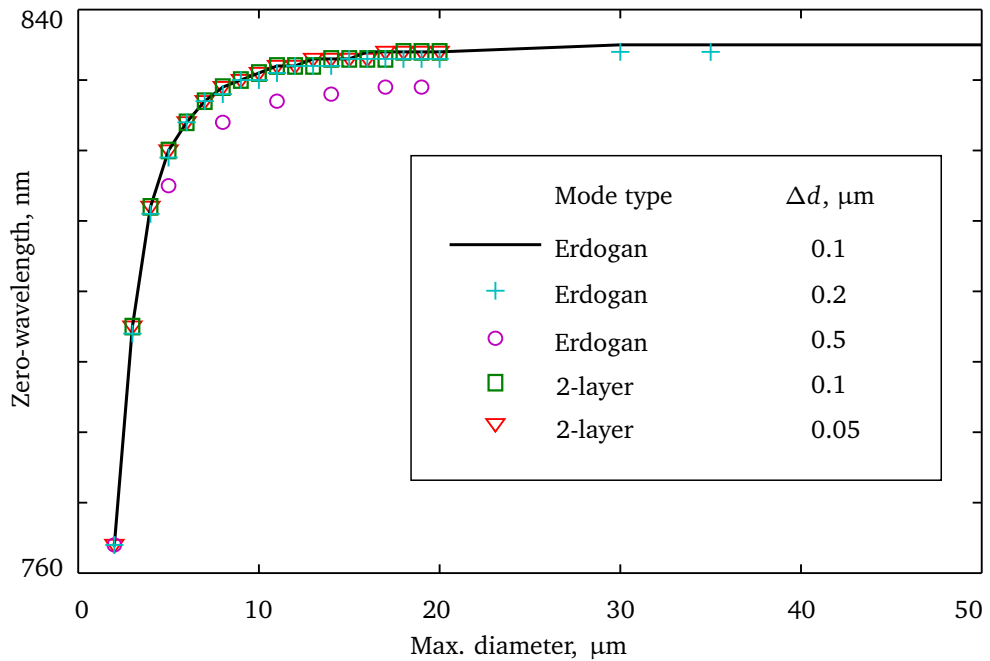


**Figure 2.19:** Zero-dispersion wavelength (see Fig. 2.13b) vs. maximum considered diameter value and diameter step. With only the waist ( $\phi 2 \mu\text{m}$ ) taken into account, all data sets coincide at the wavelength of 764 nm. With taking a larger and larger part of tapers into account, the zero-dispersion wavelength increases and saturates at 835 nm when the maximum considered taper diameter reaches 30  $\mu\text{m}$ . At  $d_{\max} = 20 \mu\text{m}$ , the zero-wavelength is 834 nm. For the diameter steps of 0.05 and 0.1  $\mu\text{m}$ , both the two- and three-layer models give the same results. Step 0.2  $\mu\text{m}$  results in a 1 nm error. Step 0.5  $\mu\text{m}$  gives the error of up to 5 nm. Simulated for SM800 fibre in the Cargille 1.35 liquid, taper slope angle 16 mrad, waist  $\phi 2 \mu\text{m} \times 3 \text{ mm}$ .

pletely different from the value without tapers (764 nm), which shows that tapers cannot be ignored in this calculation. However it is not necessary to calculate the whole tapers up to 125  $\mu\text{m}$  because the influence of the large diameter sections is negligible (the result “saturates” after  $d_{\max} = 30 \mu\text{m}$ ). The diameter step size of 0.1  $\mu\text{m}$  seems to be optimal and ensures the error of  $< 1 \text{ nm}$ . Comparison of the two- and three-layer models shows that the two layer model can be used with keeping the error  $< 1 \text{ nm}$ . For even better accuracy (if the measurement error is below 1 nm), the three-layer models should be used.

**Stretch-interferometry** The same procedure was repeated for stretch-interference, this time the figure of merit was the frequency of the interference fringes (Fig. 2.20). As the convergence criterion I used the frequency error of  $0.01 \text{ rad}/\mu\text{m}$ , which is about 0.3 % of the absolute frequency value. Again, the  $\Delta d = 0.1 \mu\text{m}$  and  $d_{\max} = 30 \mu\text{m}$  can be taken as the diameter step and maximum diameter values.

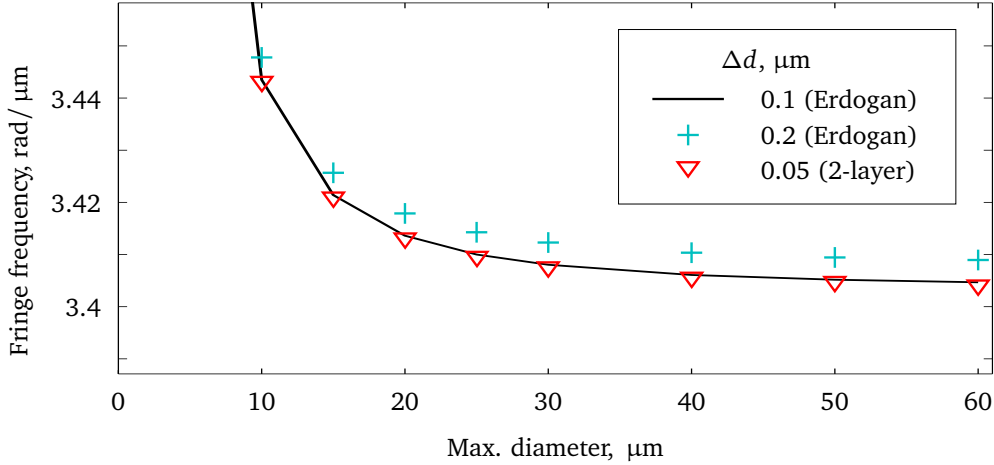


**Figure 2.20:** Fringe frequency (see Fig. 2.15b) vs. maximum considered diameter value and diameter step. At the waist diameter of  $1.5 \mu\text{m}$  all data sets coincide at the frequency of  $4.41 \text{ rad}/\mu\text{m}$ . The frequency decreases with  $d_{\max}$  and saturates at  $3.40 \text{ rad}/\mu\text{m}$  when the maximum considered taper diameter reaches  $40 \mu\text{m}$ . At  $d_{\max} = 20 \mu\text{m}$ , the frequency is  $3.41 \text{ rad}/\mu\text{m}$ . For the diameter steps of  $0.05$  and  $0.1 \mu\text{m}$ , the simulation gives the same results to  $0.001 \text{ rad}/\mu\text{m}$ . For the step of  $0.2 \mu\text{m}$ , the difference is about  $0.004$ . Simulated for SM800 fibre in air, taper slope angle  $16 \text{ mrad}$ , waist  $\varnothing 1.5 \mu\text{m} \times 3 \text{ mm}$ , wavelength  $852 \text{ nm}$ , absolute elongation  $5 \mu\text{m}$ .

## 2.6 Summary

In this chapter I have presented the methods for calculation of the guided modes in usual fibres, OMFs, and SOMMIs. Depending on the guidance regime, different models have to be used. In particular, the three-layer model used to simulate taper modes was one of the central topics of my theoretical work. The developed algorithms have been used for calculation of the phase-matching condition in our OMF waist diameter measurement method [1] as well as for simulation of the spectral and stretch-interference signals of SOMMIs.

All the developed models have been implemented as the Optical Fibre Toolbox and published with the open source code as [59] (version 1) and [2] (version 2). Since the publication of the first version two years ago, OFT was downloaded more than 1500 times.



# 3

## CHAPTER

# Samples

In this chapter I describe manufacturing, characterization and handling of OMF and SOMMI samples.

## 3.1 Production

### 3.1.1 Optical fibre tapering

Micrometre-scale diameter glass fibres were first produced and studied in the 19th century [60, 61], however they were inappropriate for optical applications due the high losses in glass itself. It was only in 1970 that, following the discovery of Kao and Hockham [7], Corning managed to produce the first optical fibre with sufficiently low attenuation for telecom purposes. This also raised interest to research aimed on creating more fibre-based devices than just optical transmission elements.

Fibre tapers were used to couple light between two fibres (fibre couplers) as well as to excite light propagation in the cladding and then couple it back to the core. However such tapers need neither a high shape uniformity, nor a very small diameter.

In 1985, the first paper mentioning an optical fibre tapered down to  $10\text{ }\mu\text{m}$  was published [62]. The research of small-diameter fibre tapers immediately followed [20, 39, 63]. However the shape quality of these OMFs (produced simply by flame-heating and pulling a commercial fibre) was still not high enough, leading to high losses.

For efficient light-matter interaction it is important to be able to make the fibre waist as long and as constant in diameter as possible. For fine control of light propagation it is also critical to control the shape of the tapers. In 1992, Birks and Li have developed a theory of fibre tapering and experimentally verified it using the “flame-brushing” technique [64–66]. In this method, a fibre is pulled

by two translation stages while at the same time being heated by a flame moving back and forth under the fibre, thereby imitating a varying flame length. They managed to achieve excellent control over the waist and taper shape, which was important for such applications as the directional couplers and the fibre beam expanders. However the diameter of the waist was on the order of dozens of micrometres.

In 2003, Tong et al. proposed a rather complicated method of drawing high quality subwavelength-diameter fibres [67]. Finally, in 2004, Brambilla et al. for the first time reported a successful production of a low-loss sub-micrometre-diameter fibre using the flame-brushing technique [9]. This flame-brushing method with its modifications employing various types of heat sources (gas flame, electrical microheater, laser-heated sapphire furnace) is the one usually used nowadays around the world to produce high-quality (sub)micrometre-diameter tapered fibres.

There are also alternative methods based on fibre etching or polishing [68, 69]. As such, they yield OMFs of lower optical quality than fibre pulling [70] and are therefore rarely used today. However, polishing provides additional control over the waist shape and can be used in combination with tapering as for example in [23].

### 3.1.2 Pulling machine

To manufacture our samples, we have used the fibre pulling machine developed and built in our group a few years ago [26] and currently belonging to the group of Arno Rauschenbeutel (Fig. 3.1). Its primary parts are two computer-controlled translation stages, stacked on top of each other, and an oxygen-hydrogen burner. Two steel plates with precision V-grooves are fixed on top of the stages. The grooves are aligned coaxially to each other and parallel to the axis of motion of the stages. The fibre to be pulled is clamped in these V-grooves with strong magnets and thus is aligned relative to the stages.

The bottom (translator) stage is moving left and right and the burner is stationary. The top stage (stretcher) is continuously pulling the fibre while the bottom stage is moving the whole fibre left and right imitating the movement of the flame. In comparison to the original flame-brushing design of Birks [66], this variant offers a simpler construction (due to the fixed burner) and lower air flow influence on the flame (the flame is not moving).

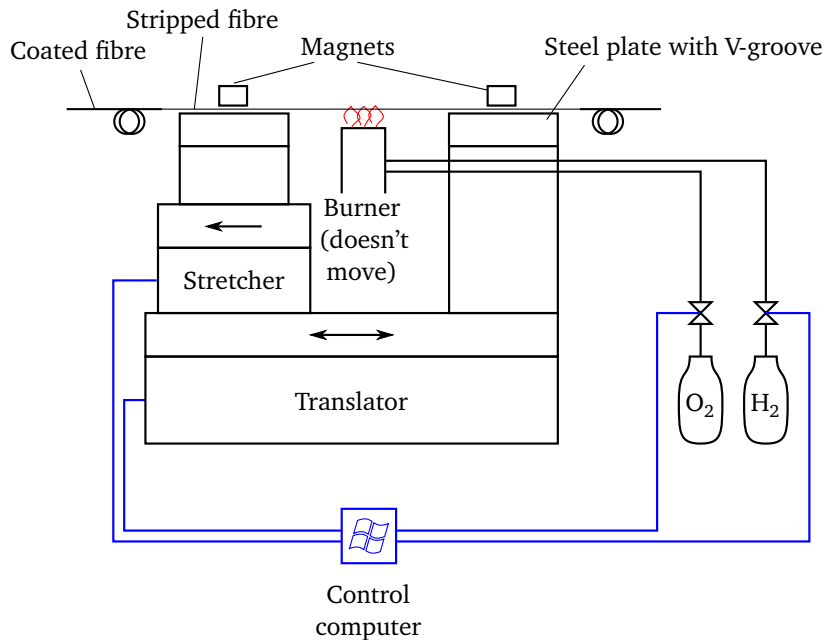


**Figure 3.1:** Pulling setup. Computer-controlled translator stage moves the fibre back and forth above the ultraclean oxygen-hydrogen flame while, at the same time, the second stage stretches it.

### 3.1.3 Optical fibre type selection

The fibre, used for tapering, should satisfy the requirements to the pigtails (be transparent and single-mode in the design wavelength range) and at the same time be suitable for tapering, i. e. withstand heating above the softening point without losing its guiding properties.

Since the research in our group is to a large extent concentrated around the caesium atoms, having the resonance wavelengths of 852 nm and 894 nm, we have various equipment for this wavelength region, including a tunable laser for 850–1050 nm. Therefore, the default wavelength region for this project was also chosen to be 800–1100 nm. A suitable fibre for this wavelength range is the SM800 fibre produced by Fibercore Ltd. Its properties are listed in Tab. 3.1.

During tapering, a stripped (with the coating removed) fibre is heated close to the glass softening point (about 1600 °C). The materials of the core and the cladding should be suitable for such heating. The SM800 fibre has a pure fused silica cladding and a germanium-doped silica core. These materials survive the heating well.

As an example of a different behaviour, the Nufern S630-HP fibre, which is a single-mode fibre for shorter wavelengths, has a pure silica core and a fluorine-doped cladding. Fluorine is a volatile element and tends to evaporate from the fibre during heating. As the result, the core-cladding refractive index van-

**Table 3.1:** Properties of the Fibercore SM800 optical fibre. [32]

Design wavelength	830 nm
Cut-off wavelength	660–800 nm
Numerical aperture	$0.12 \pm 0.02$ [24]
Mode field diameter	$5.6 \mu\text{m}$
Attenuation	< 5 dB/km
Fibre diameter	$125 \pm 1 \mu\text{m}$
Core diameter	$4 \mu\text{m}$ [24]
Core-cladding concentricity	< 1 $\mu\text{m}$
Coating diameter	$245 \mu\text{m} \pm 5\%$
Coating material	Acrylate [24]

ishes in the tapered region and the fibre loses its guiding properties. Such a fibre is thus unsuitable for making tapered fibres by heating.

During this project, we also produced OMFs for longer wavelengths, around 1500 nm. For this, a perfect starting point is the standard telecommunication fibre SMF-28 from Corning Inc., designed for the telecommunication wavelengths of 1310 and 1550 nm. It has practically the same technical specifications as SM800 except for the larger core diameter— $8.2 \mu\text{m}$ —and the cut-off wavelength of 1260...1280 nm [71, 72].

### 3.1.4 Target sample shape

For each SOMMI sample, we need to decide on the taper shape and the waist diameter and length. In this chapter, I only discuss samples to be used in air, therefore I will describe the in-air design. The very same approach is then used for in-liquid SOMMIs in chapter 4.

#### 3.1.4.1 Waist diameter

Initially (in the untapered input pigtail) all light power is contained in the fundamental  $\text{HE}_{11}$  mode. In the taper, the  $\text{HE}_{11}$  mode can be coupled to higher modes of the same symmetry, i. e.  $\text{HE}_{1m}$  modes. Thus, the modes  $\text{HE}_{12}$ ,  $\text{HE}_{13}$  etc. can be excited while EH, TE, TM and  $\text{HE}_{lm}$  (with  $l \neq 1$ ) can not.

The interferometer modes are the  $\text{HE}_{11}$  and  $\text{HE}_{12}$  ones. Therefore we should avoid excitation of the  $\text{HE}_{13}$  and higher  $\text{HE}_{1m}$  modes by the proper design of the taper. However, the manufacturing imperfection can still lead to excitation of the wrong modes.

In Fig. 3.2, I show the three modes in question (black curves). The gray curves correspond to all other modes, which can be guided in a fibre of this diameter range. If the fibre symmetry is violated (e. g. by slight misalignment

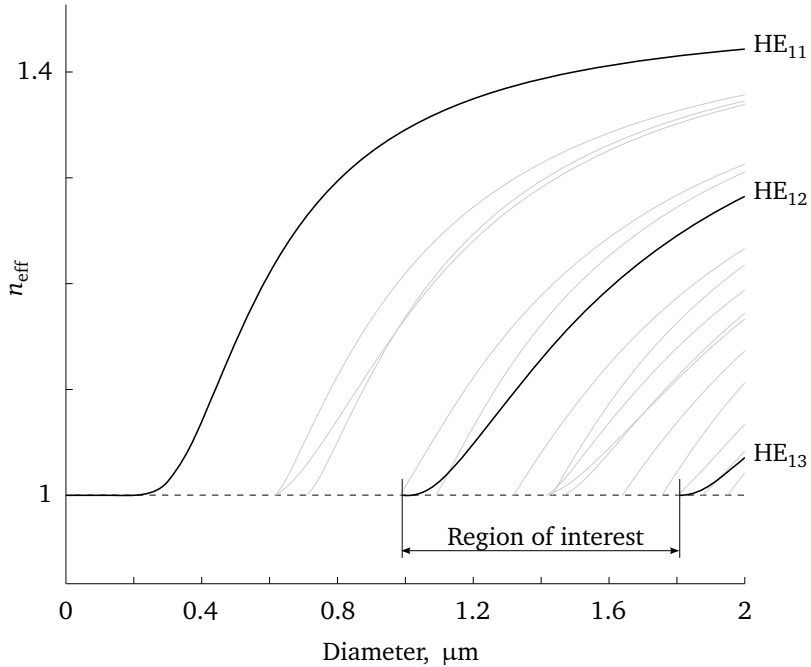


**Figure 3.2:** Interferometer modes. Initially (in the untapered input part of the fibre) all energy is in  $\text{HE}_{11}$  mode. In the tapers,  $\text{HE}_{11}$  mode is coupled to  $\text{HE}_{12}$ . The waist should have the diameter of at least  $1 \mu\text{m}$  to guide the  $\text{HE}_{12}$  mode. In case the unwanted  $\text{HE}_{13}$  mode is also excited in the down-taper, we can cut it off in the waist by choosing the waist diameter below  $1.8 \mu\text{m}$ . All other guided modes are not excited provided that the fibre is rotationally symmetric. (Silica in air,  $850 \text{ nm}$ .)

and bending), some of these modes can be excited as well and contribute to the noise of the interference pattern.

In this particular case (fibre in air,  $850 \text{ nm}$  wavelength), to guide the  $\text{HE}_{12}$  mode, the waist should be at least  $1 \mu\text{m}$  thick. If we do not make the waist thicker than  $1.8 \mu\text{m}$ , the  $\text{HE}_{13}$  mode will not be able to propagate through the waist, even if excited in the down-taper. Thus we end up with the possible range for the waist diameter from  $1$  to  $1.8 \mu\text{m}$ .

Another aspect to consider is the difference between the effective refractive indices  $\Delta n_{\text{eff}}$  of the  $\text{HE}_{11}$  and  $\text{HE}_{12}$  modes. To the first approximation, the larger it is, the more sensitive the interferometer will be to any changes, cf. Eq. (2.12):

$$I \sim 0.5 + 0.5 \cos \left( \frac{2\pi}{\lambda} L \Delta n_{\text{eff}} \right), \quad (2.12)$$

Obviously,  $\Delta n_{\text{eff}}$  is largest close to the  $\text{HE}_{12}$  cut-off, just above  $1 \mu\text{m}$ . At the same time, we should remember that at a different wavelength the mode curves will be shifted (cf. Fig. 2.11), so, to extend the operating wavelength range, we should

stay as far from the cut-off diameters as possible. Therefore, we end up with an optimal waist diameter of about  $1.3 \dots 1.4 \mu\text{m}$ .

To be more precise, the SOMMI sensitivity estimation involves the calculation of  $\partial\phi/\partial L$  for sensitivity to elongation, or  $\partial\phi/\partial n_{\text{out}}$  for sensitivity to the surrounding refractive index, or  $\partial\phi/\partial T$  for sensitivity to temperature, and so on, where  $\phi = 2\pi\Delta n_{\text{eff}}L/\lambda$  (see Eq. (2.12)). However, now I am not interested in obtaining the highest possible sensitivity for any specific experiment. The present goal is simply to make a working interferometer and verify that it works according to the model developed in the previous chapter.

### 3.1.4.2 Waist length

From the same Eq. (2.12), it follows that a longer waist leads to a higher frequency of interference fringes in the spectral interferometry (Fig. 3.3). The lower the frequency, the easier it is to measure the signal. However with too few fringes, the signal is hard to analyse with a good precision.

There is also a purely technical limit: The shortest waist length a pulling

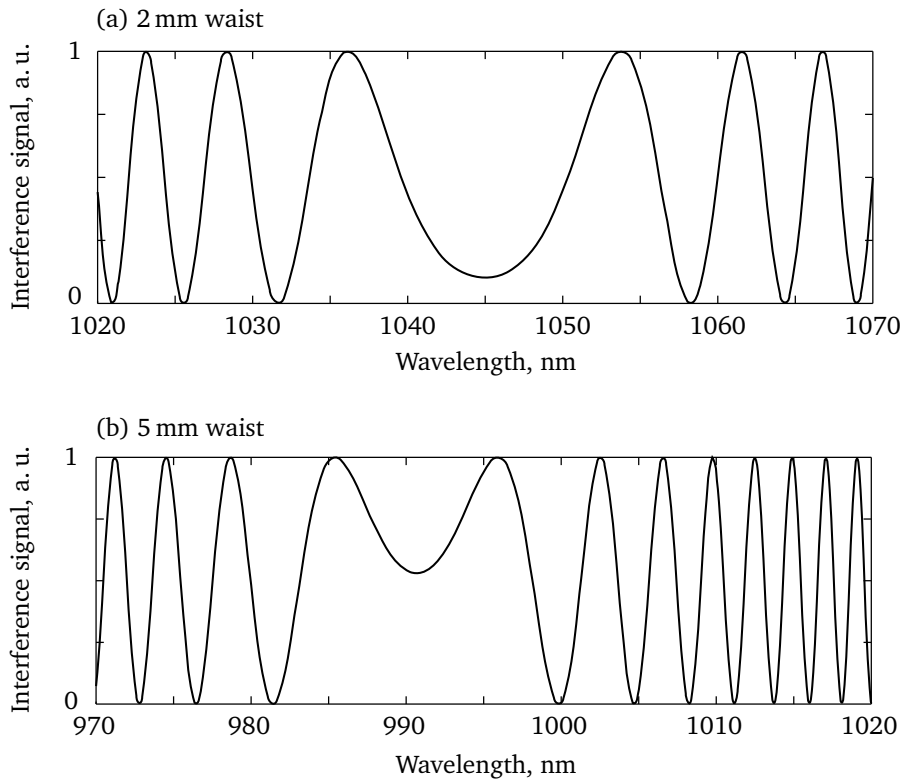


**Figure 3.3:** Simulated spectral interference signal in a SOMMI with 16 mrad taper and (a) 2 mm and (b) 5 mm waist. (Silica in air,  $1.3 \mu\text{m}$  waist diameter.)

machine can produce equals to the effective length\* of the heater (in our case flame) used. Our pulling machine has a heater with the effective flame length of about 1 mm. My samples usually have the waist length of 2...5 mm.

### 3.1.4.3 Taper angle

Tapers are responsible for mode splitting and recombination, and should provide for the  $HE_{11}$  and  $HE_{12}$  modes coupling and minimize coupling to the  $HE_{13}$  mode. The critical angle theory (Sec. 2.3.5) allows to determine if, at a given diameter and for a given slope angle, any two given modes are likely to couple. For modes  $HE_{11}$ ,  $HE_{12}$  and  $HE_{13}$ , four regions should be considered in a taper angle vs. fibre diameter diagram (Fig. 3.4). Region A is above the delineating curves  $HE_{11} \leftrightarrow HE_{12}$  and  $HE_{12} \leftrightarrow HE_{13}$ . Therefore, if the taper crosses this region, the

---

\*Effective length of a heater is the length over which the fibre glass is heated above the glass softening point.

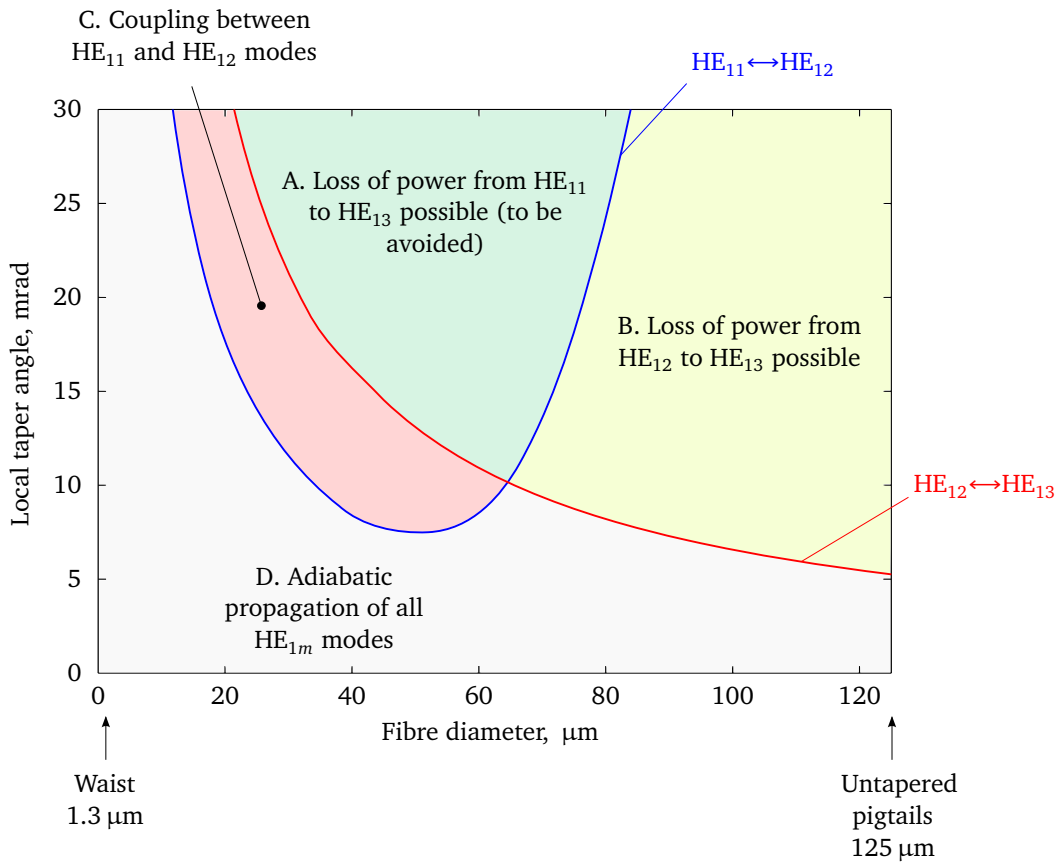


**Figure 3.4:** Zones of coupling and adiabatic mode propagation. Calculated based on the critical angle theory, Sec. 2.3.5. (SM800 fibre in air, 850 nm.)

power can be lost to the  $\text{HE}_{13}$  mode, which is to be avoided. Region B is above the  $\text{HE}_{12} \leftrightarrow \text{HE}_{13}$  delineating curve but below the  $\text{HE}_{11} \leftrightarrow \text{HE}_{12}$  one. Therefore only the power in the  $\text{HE}_{12}$  mode can be lost to  $\text{HE}_{13}$ . However, mode  $\text{HE}_{12}$  is decoupled from  $\text{HE}_{11}$  in this region (it is below the  $\text{HE}_{11} \leftrightarrow \text{HE}_{12}$  curve), therefore this loss does not influence the interference result. Region C is the one where the  $\text{HE}_{11}$  and  $\text{HE}_{12}$  modes are coupled and no coupling occurs with mode  $\text{HE}_{13}$ . This is therefore the target area for mode splitting and recombination. Finally, region D is the area of adiabatic propagation of all modes.

The OMF pigtailed have the diameter of  $125\text{ }\mu\text{m}$ , and thus the down-taper always starts in areas B or D, which is fine. The slope should then be large enough for the  $\Omega(d)$  curve (we call it a *taper trajectory*) to cross area C but not too large, so that it does not get into area A. In the waist, the slope angle is zero, therefore the waist is always in area D, and the two interfering modes propagate adiabatically. The up-taper trajectory should again cross area C to achieve mode recombination. It does not matter in which area—B or D—is the output pigtail: neither mode  $\text{HE}_{12}$  nor mode  $\text{HE}_{13}$  are detected at the output (both are lost because the pigtail is single-mode).

The pulling machine used in this project can only produce symmetric tapers, so the trajectories for the down- and the up-taper are the same. Moreover, during building the pulling machine it was discovered that if the  $\Omega/d$  ratio is too large, the tapers do not exhibit a well defined shape [26]. Therefore the control software of the pulling machine limits the slope to [73]\*

$$\Omega/d = 0.15 \text{ mrad}/\mu\text{m}.$$

In Fig. 3.5, this limit is indicated by the dashed line. At no point can our samples get above this line. Apparently, this line satisfies the above requirements: it starts in area B, crosses area C, gets to the waist, and then returns through C to B. It never crosses the “forbidden” area A. Therefore, for most of my samples I just specified the value of 16 mrad as the desired taper angle, the pulling machine limited it to  $\Omega_{\max} = 0.15d$ , and this trajectory (shown with the thick solid line) worked fine as can be seen from the rest of the thesis.

For comparison, the step-wise line at the bottom of Fig. 3.5 indicates the trajectory often used for our adiabatic samples. Figure 3.6 shows both the 16 mrad and the 3-1-3 mrad taper shapes.

---

\*To be more precise, the limiting factor depends on the effective flame width given to the control software of the machine by the user and is 0.265 for 0.7 mm flame, 0.193 for 1.0 mm, and 0.118 for 1.6 mm. I have found these values by fitting an exponential curve to the design taper shape plotted by the pulling control software [17]. The flame width of course does not change but is not known exactly. Besides, by decreasing this parameter, one can achieve steeper tapers by compromising their smoothness a little; it makes sense when designing a SOMMI: we are more interested in the efficient coupling leading to a higher contrast than in the no-loss propagation. Without loss of generality, I will be using the value of  $0.15 \text{ mrad}/\mu\text{m}$  in this text; the exact values are used in all taper shape-related calculations.

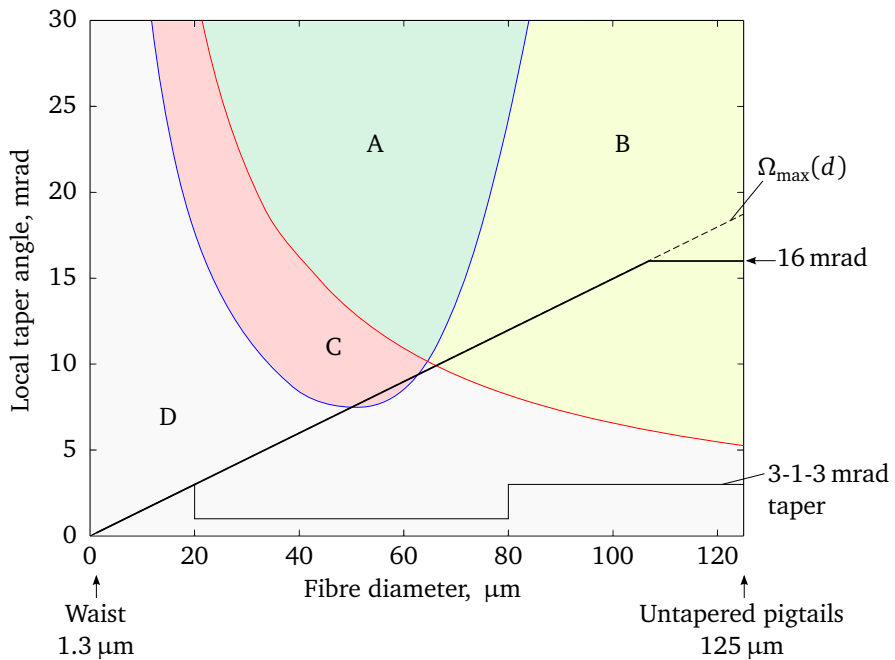


**Figure 3.5:** Taper trajectories. (SM800 fibre in air, 850 nm.)

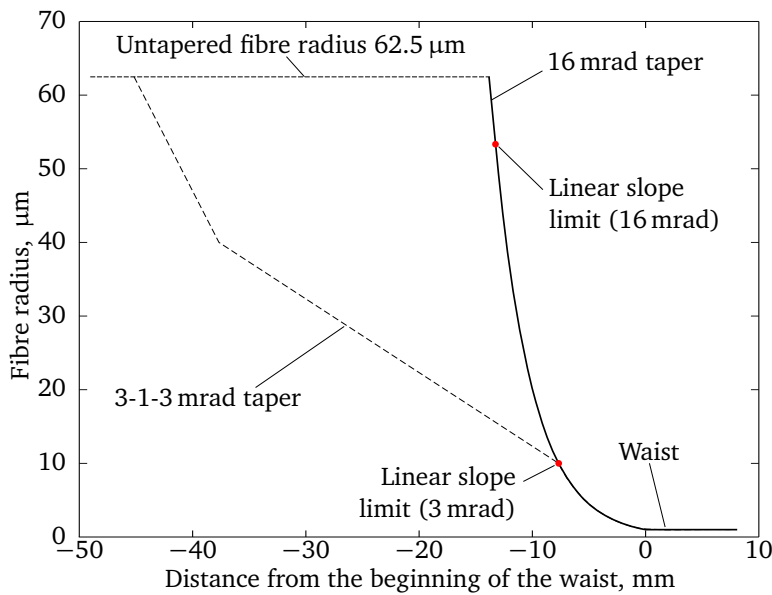


**Figure 3.6:** Non-adiabatic 16 mrad taper (solid line) as well as adiabatic 3-1-3 mrad taper (dashed line) shapes. Due to the software taper slope limit of  $0.15 \text{ mrad}/\mu\text{m}$ , both tapers have the same exponential shape below  $r = d/2 = 10 \mu\text{m}$ .

### 3.1.5 Sample shape verification

To be able to reliably interpret experimental results, it should be checked whether the samples we produce are actually the ones we design. The pulling machine is equipped with a microscope for a visual inspection. However since the samples are very thin, the visual inspection does not provide much information except for some dramatic problems (like broken waist or significant bending). Therefore several other methods have been used during this project.

#### 3.1.5.1 Scanning electron microscopy

Since the sample length is on the order of several centimetres and the diameter range is  $0.5\ldots125\text{ }\mu\text{m}$ , the instrument of obvious choice to characterize our samples is a scanning electron microscope (SEM): The resolution of an SEM on the order of  $1\text{ nm}$  and the achievable accuracy on the order of  $10\text{ nm}^*$  are suitable for our purposes. At the same time, SEM allows measuring larger samples than accessible with a more accurate transmission electron microscope.

**Waist diameter** As far as I know, our group was the first one to reliably measure the microfibre waist diameter with high precision using an SEM. This process requires special handling of the samples and recalibration of the microscope for each series of measurement to obtain the maximum accuracy accessible with SEM. All details can be found in the Diplom work of Pritzkau [74] and, in a shorter form, in [1]. Figure 3.7 shows SEM images of the taper and the waist of one of our submicrometre-diameter samples.

SEM poses some problems when considering our samples. Glass gets charged by the electron beam and deflects electrons from their original trajectory, thus reducing the accuracy of measurement. To prevent this effect, the fibre must be coated with gold. The thickness of the golden layer is not perfectly well defined thus contributing to the overall error of measurement. Besides, a gold-coated sample is of course unusable in optical experiments. Another problem we have faced is that lengthy exposure to the electron beam required to obtain high-quality images results in damaging (burning) the thin sample's waist. A clear disadvantage of the SEM measurements is also the required time—a few hours per sample, provided that the microscope is readily available.

The main advantage over other methods is the high resolution along the fibre axis (below  $1\text{ }\mu\text{m}$ , determined by translation stages of the SEM) allowing to resolve small shape irregularities.

Our SEM results are summarized in Sec. 3.1.5.3 on page 62.

---

\*Usually SEMs are calibrated to  $\pm 5\%$  corresponding to  $\pm 50\text{ nm}$  for a  $1\text{ }\mu\text{m}$  sample. A better accuracy can be achieved by recalibrating the SEM during the measurement using calibration targets.

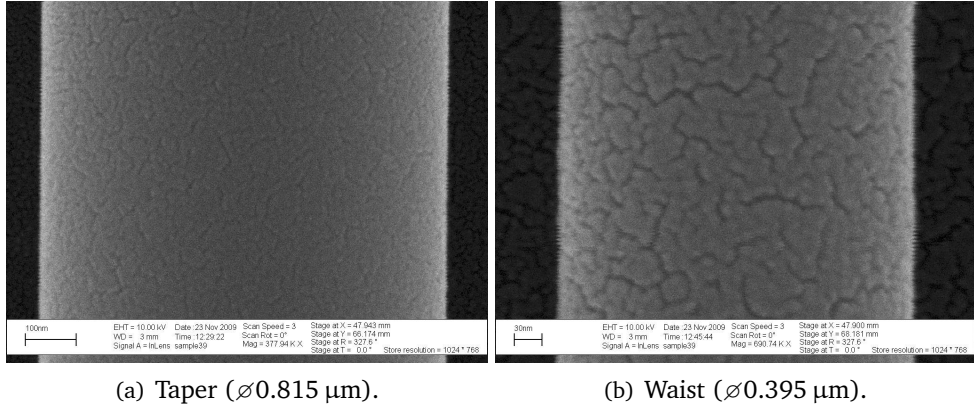


**Figure 3.7:** SEM pictures of our samples. The surface texture is due to clusters of gold sputtered on the fibre to prevent charging.

**Taper shape** While we have measured the diameter of the waist of our samples, our colleagues in Mainz have performed a similar measurement of the tapers produced with the same pulling machine [73]. Their conclusion was that the measurement results coincide (within the SEM error of  $\pm 5\%$ ) with the designed shape of the sample. Only one sample was measured, so reproducibility was not checked.

Being very slow and destructive, SEM is not an optimal choice to characterize OMF samples. Therefore two indirect methods to measure the sample diameter are in use in our group. They are described in the next section and in Sec. 3.1.5.4.

### 3.1.5.2 Harmonic-generation method

The first method we are using was developed by our team [1] and is based on the nonlinear processes in OMFs. When a high-intensity light wave travels through a fibre, it can excite second- and third-harmonic waves [48, 50]. For efficient second- and third-harmonic generation (SHG, THG), the phase-matching condition should be fulfilled:

$$v_{\text{phase},\omega} = v_{\text{phase},2\omega} \quad \text{or} \quad v_{\text{phase},\omega} = v_{\text{phase},3\omega},$$

where  $v_{\text{phase},\omega}$  is the phase velocity of the fundamental (pump) wave,  $v_{\text{phase},2\omega}$  and  $v_{\text{phase},3\omega}$  the phase velocities of the second- and third-harmonic waves. This condition, usually inaccessible in bulk glass due to the material dispersion, can be fulfilled in OMFs due to the strong modal dispersion (see Fig. 2.11 on page 37). The phase-matching condition for a given wavelength is only satisfied at a specific fibre diameter (Sec. 2.4.2). In tapers, where the fibre diameter constantly changes, the phase-matching condition will be fulfilled for any wavelength corresponding to the diameter range  $d_{\text{waist}} \dots 125 \mu\text{m}$ . However, for any given wave-

length, the phase-matching condition will be fulfilled only over a very short fibre length, due to the constantly changing diameter. In the waist, on the contrary, an OMF has the same diameter over a relatively large length, providing for a very efficient harmonic-generation. Thus, knowing the wavelength, at which the peak of the harmonic signal is observed, we can derive the waist diameter. To determine the peak wavelength, we are using a tunable Ti:sapphire laser and change its wavelength until the maximum harmonic generation efficiency is observed. The details are given in [1].

This method offers an excellent resolution: with a typical spectrometric equipment, we can achieve the OMF waist diameter error of about 0.5%. The measurement can also be performed directly in the optics lab and ultimately even during the pulling process without the need to take the sample out of the setup.

### 3.1.5.3 SEM and harmonic-generation measurement results

Using SEM, we have carefully measured 6 samples, for 3 more the diameter was obtained roughly (Tab. 3.2). For samples 24, 28 and 31 (I use our actual sequential sample numbers, see appendix C), no SEM calibration was performed and therefore the error is the  $\pm 5\%$  value specified as the maximum error of our microscope (ZEISS Supra 55). The  $0.007 \mu\text{m}$  error of samples 52 to 71 is determined by the systematic uncertainty of the SEM image analysis ( $0.005 \mu\text{m}$ ), the error of the calibration target used for SEM recalibration ( $0.004 \mu\text{m}$ ) and the variation of the gold coating thickness ( $0.002 \mu\text{m}$ ).

We have also performed one detailed SEM measurement of the waist: the same sample (sample 56) was measured at many points along the whole waist and at different electron beam energies and scanning speeds [1]. This measure-

**Table 3.2:** SEM-measured OMF waist diameters.

Sample number	Diameter, $\mu\text{m}$		
	Design diameter	SEM-measured diameter	Deviation
24	0.478	0.52(3)	0.042(30)
28	0.376	0.47(2)	0.094(20)
31	0.376	0.37(2)	-0.006(20)
52	0.378	0.389(7)	0.011(7)
55	0.404	0.419(7)	0.015(7)
56	0.393	0.414(7)	0.021(7)
59	0.419	0.428(7)	0.009(7)
67	0.460	0.485(7)	0.025(7)
71	0.500	0.511(7)	0.011(7)

Samples 52, 55, 56, 59, 67, and 71 correspond to samples D, E, A, C, B, and F from [1] respectively.

ment has revealed an excellent uniformity of the waist, the diameter variation over the 4 mm length was found to be only  $\pm 3 \text{ nm}$ , i.e.  $\pm 0.7\%$ . High waist uniformity can also be concluded from the high harmonic generation peaks we usually observed.

Using this SEM technique, we have verified our harmonic generation-based measurement [1] and used the latter to measure more of our samples. The result is shown in Fig. 3.8. The SEM-measured diameter values are on the average 5% higher than the design values. The harmonic-measured values are 3% higher than the design ones, so there is a 2% discrepancy. However, for those samples that were measured with both techniques, the harmonic-based values were 2% lower than the SEM-determined values. This indicates that there was a 2% systematic error in our measurements, though we do not know whether it is due to the SEM procedure or the harmonic-method. At the same time, it is obvious that the pulling machine produces slightly larger (within 5%) samples than expected.

All in all, these measurements of the OMFs produced with our pulling machine show a good waist uniformity and the waist and the tapers diameter deviation from the design values is within the RMS-error of  $\pm 5\%$ .

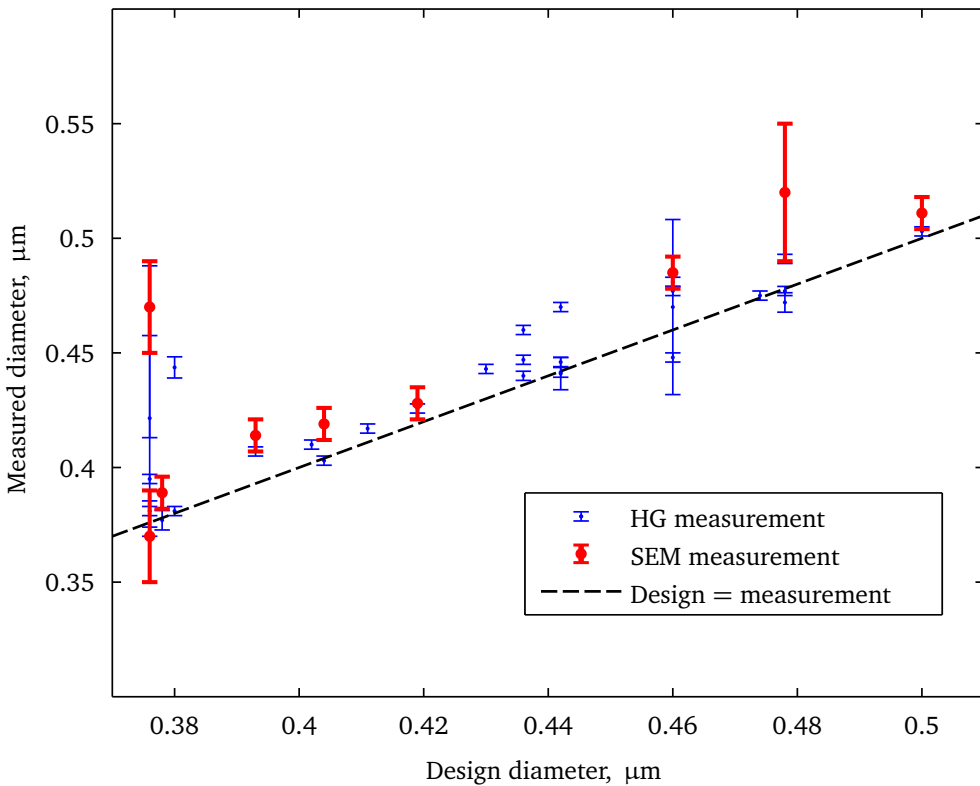


**Figure 3.8:** SEM- and harmonic generation-based diameters of 31 OMF samples.

The harmonic method still has three drawbacks.

1. Firstly, because the wavelength is directly connected to the diameter, measuring a large range of diameters requires a large and often inaccessible wavelength range. As a rule of thumb, the fibre diameter should roughly equal half the wavelength of incident light (see Fig. 2.12 on page 37). Unfortunately, a typical Ti:sapphire laser can not reach wavelengths above approximately 1100 nm [75], making it impossible to measure samples thicker than about 0.5  $\mu\text{m}$ . With a broad-band telecom (1550 nm) laser source, it is possible to measure thicker fibres, with the upper limit around 0.8  $\mu\text{m}$ . Figure 3.9 shows green 520 nm light generated by the THG process with a high-power C-band telecom laser. Ultimately, the limiting factor is the transparency window of fused silica going up to about 2000 nm (diameters up to 1  $\mu\text{m}$ ).\*

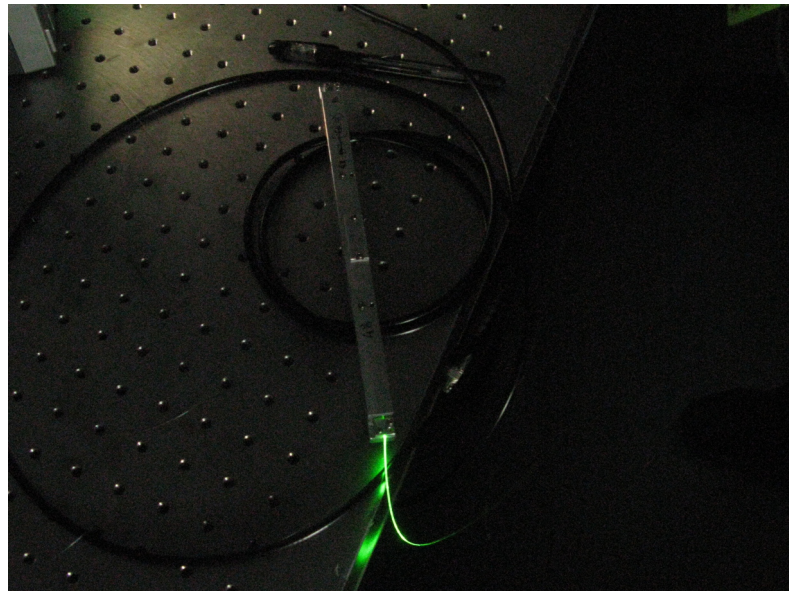


**Figure 3.9:** Third-harmonic generation produces green output from the 1550 nm pump light in an OMF. Scattered light at the output end of the OMF sample. (Initial fibre: SMF-28, OMF waist design diameter 0.78  $\mu\text{m}$ , sample 48.)

---

\*It may be possible to measure larger diameters using phase-matching with other  $3\omega$  modes than those used in our method. Lee et al. have successfully generated third harmonic light using  $\text{HE}_{11}$  phase-matching to  $\text{EH}_{31}$ ,  $\text{EH}_{12}$ ,  $\text{HE}_{32}$  and  $\text{HE}_{13}$  [76]. At 1550 nm it corresponds to fibre diameters around 3.5  $\mu\text{m}$ . However the nonlinear overlap (0.004...0.007) is significantly smaller than for the modes we are using in our method (0.2...0.9 for  $\text{HE}_{11}$  to  $\text{HE}_{31}$  and  $\text{HE}_{12}$ ), so the measurement may be more challenging. With our equipment we have been unable to detect the THG with the overlap of 0.007 ( $\text{HE}_{11}$  to  $\text{EH}_{11}$ ). We have not investigated this opportunity in detail so far.

2. The second problem with the harmonic generation method is the yet unexplained damage of the fibres sometimes observed in our experiments. We have noticed that when the third-harmonic generation UV light is excited in the fibre, a strange bubble-like structure can be later seen on the fibre surface (Fig. 3.10) and the sample transmission decreases, probably due to scattering. Despite discussions with the fibre manufacturer (I visited Fibercore Ltd., Southampton, in 2009), we were unable to determine the reason of this effect. Clearly, if this happens, our method cannot be called strictly nondestructive. However, for thicker samples, in which the third harmonic does not fall into UV, this is not an issue. It is also possible to avoid the generation of UV in the samples by using a narrow-bandwidth pump laser and avoiding the phase-matched wavelength for THG. For most samples, SHG results suffice to exactly determine the fibre diameter.

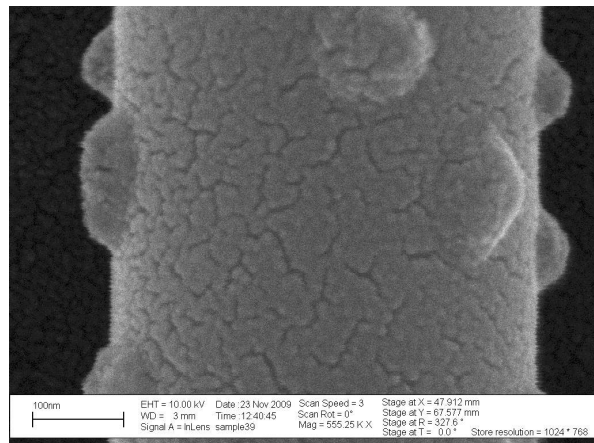


**Figure 3.10:** SEM picture of an OMF part damaged by the UV radiation created by the THG process. The fine surface texture is due to clusters of gold coating.

3. The last and the critical problem for our manufacturing goal—an interferometer fibre—is that this method does not tell us much about the actual shape of the sample, only about the waist diameter. This means we cannot evaluate how well the pulling machine produced the desired taper slope.

#### 3.1.5.4 Scattering measurement

Accurate measurement of the optical fibre diameter is obviously of interest to manufacturers of optical fibres. Telecommunication and specialty optical fibres are drawn from a preform at a speed of meters per second [77, 78] and require continuous and precise diameter monitoring [79]. Clearly, some optical method should be used for such sort of measurement. Interestingly, the appropriate methods were first developed to measure the diameter of insulation [80] and spider [81] fibres.

The method used is based on scattering of a laser beam incident on a fibre perpendicular to its axis (Fig. 3.11). The theory of light scattering on dielectric cylinders dates back to Lord Rayleigh in 1881 [82]. It was written in the usually used form for plane waves by Hulst in 1957 [83] and extended to laser beams by Kozaki in 1982 [84]. The polarization effects were investigated by Abushagur and George in 1985 [85]. The first application of the scattering method to measuring optical fibres was described in the 1970s by Watkins et al. [79, 86]. In 1995, Zimmermann et al. [87] have experimentally verified the Kozaki's theory with optical waves and dielectric cylinders with the diameter of tens of micrometres. (Kozaki used centimetre waves in his experiment.) In 2004, this technique was for the first time used to measure OMFs and verified (using SEM) to be accurate to at least  $0.05 \mu\text{m}$  [88].

The measurement scheme is shown in Fig. 3.11. An OMF sample is illuminated from the side with a laser beam. Behind the fibre, on a screen, the interference pattern is observed (Fig. 3.12). It consists of the bright central maximum and several side maxima and minima. The angular distribution of intensity can be calculated provided that the fibre refractive index and diameter, and the beam size and wavelength are known [89]. Figure 3.13 shows the calculated intensity distribution for a range of fibre diameters. Thus, by comparing the measured and the calculated intensity-vs.-angle distribution, one can deduce the fibre diameter.

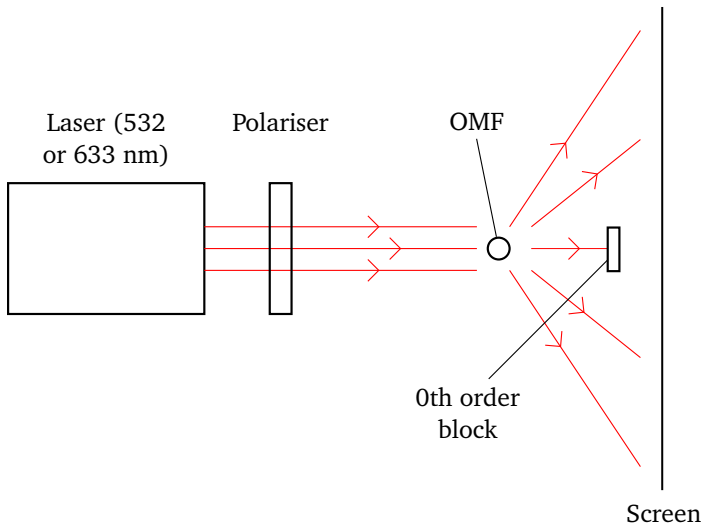


**Figure 3.11:** Scattering measurement setup. I have used a red HeNe 633 nm laser and a green frequency-doubled laser pointer (532 nm). The laser light is polarized parallel or orthogonally to the fibre. The scattering pattern is observed on the screen, the maxima and minima position noted and then analysed. The central maximum is mostly blocked: it is so bright that makes it impossible to note the positions of other extrema. See Fig. 3.21 for the actual setup photo.

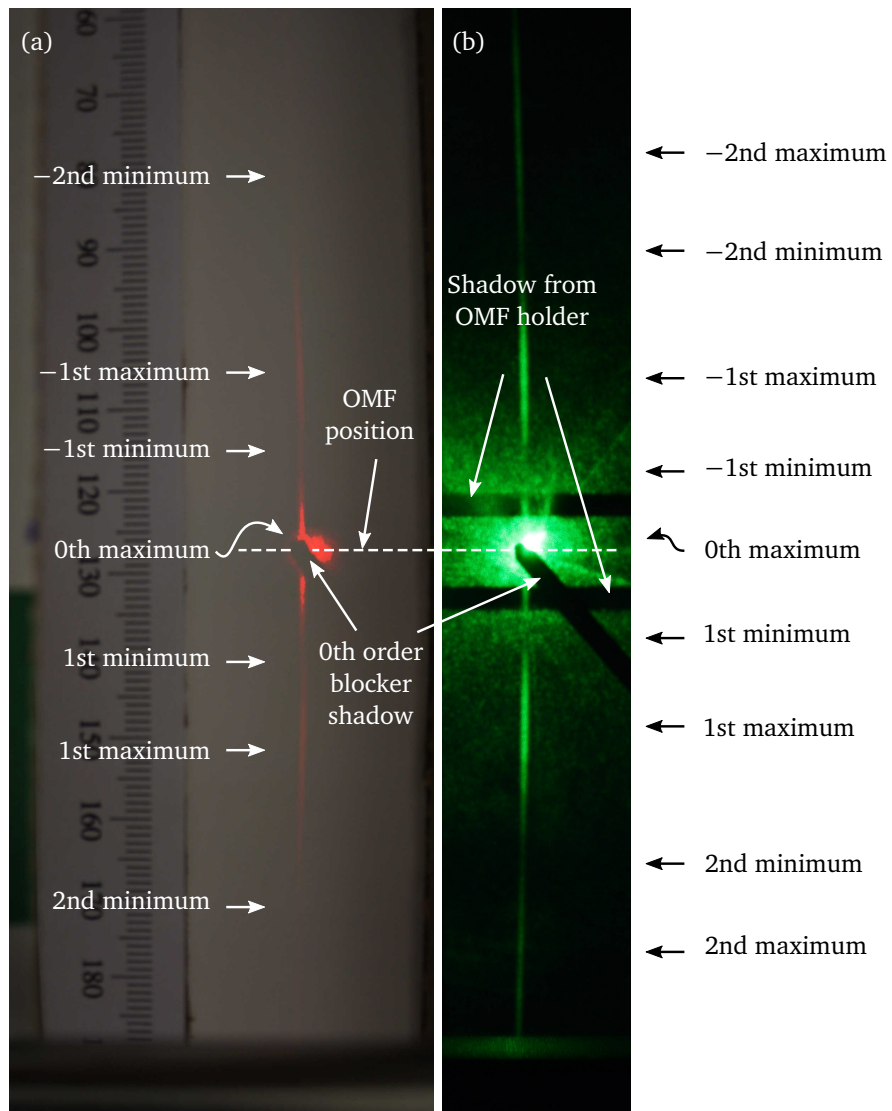


**Figure 3.12:** Diffraction pattern behind the OMF waist. (a) With a red 633 nm laser. Polarization was determined by the laser itself, without any external polarizer. (b) With a green 532 nm laser pointer. It produces almost non-polarized light, so a polarizer was used. Light scattered by scratches on the polarizer can be seen. Polarization was in both cases parallel to the sample. (Sample 168, 1.26(6)  $\mu\text{m}$  waist.)

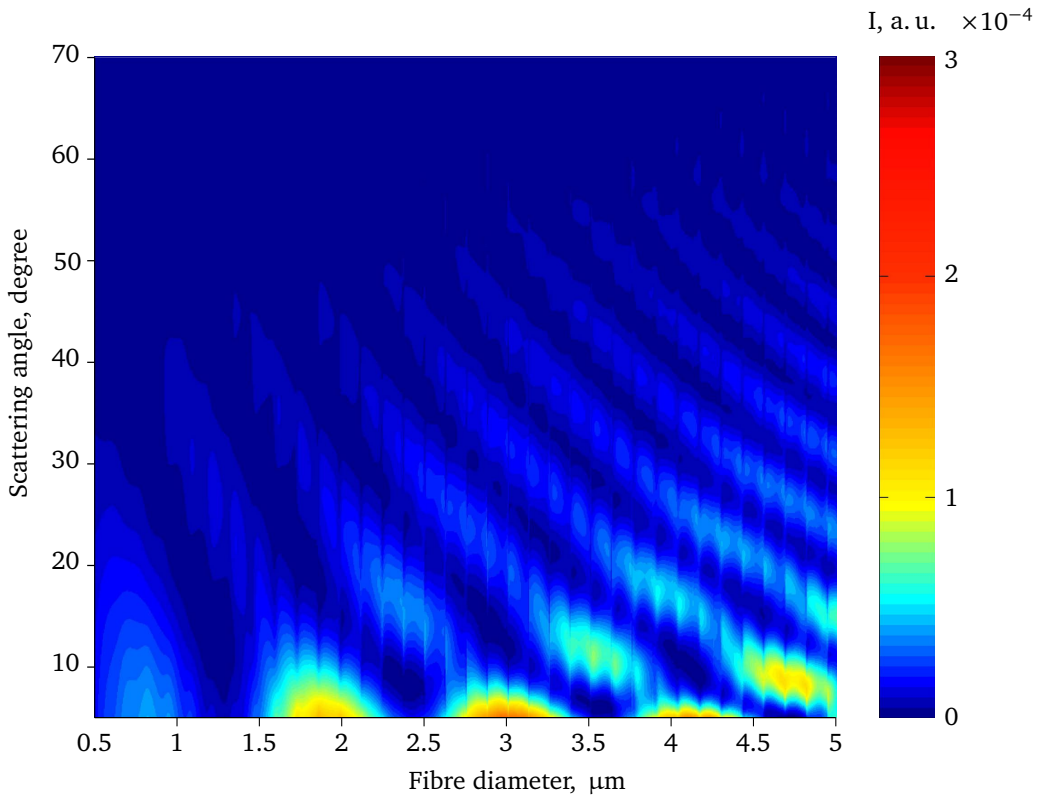


**Figure 3.13:** Calculated diffraction pattern for different OMF diameters. Intensity at the angles below  $5^\circ$  (0th maximum) is not shown: it is so high that the rest of the distribution would not be visible. Periodic vertical artefacts are explained by Mie resonances [88]. Polarization: parallel to the sample. (Silica rod in air, 532 nm.)

Obviously, this is the most promising measurement method. It is fully non-destructive and non-contact, which means that it also minimizes the risk of destroying a sample accidentally while handling it. It can be automated and made very fast. It requires only inexpensive equipment. And, unlike the harmonic generation method, it can measure the OMF diameter along the sample. In [88], the error of this method is estimated to be on the order of  $0.05\text{ }\mu\text{m}$ . This is less than 5% for a SOMMI designed for operation in air (diameter about  $1.5\text{ }\mu\text{m}$ ) and less than 3% for a SOMMI in liquid (diameter  $> 2\text{ }\mu\text{m}$ ). This is still about 10 times worse than what we get with the harmonic generation-based method.

We did not perform many measurements using the scattering method to draw any conclusion about our samples in general. Although the method is promising, it should first be fully developed (both in terms of hardware and software); now it requires too many manual operations and is therefore very slow and prone to mistakes. For those samples that were measured, a smaller or larger deviation from the design diameter was observed (see later sections).

## 3.2 Stretch-interferometry

A very different approach to testing a SOMMI sample, in comparison to measuring its shape, is to actually observe interference with it. For this, light from a laser diode can be coupled into the one OMF pigtail and the output power measured at the other pigtail. If the sample is stretched a little (using the translation stages that were used for producing the sample), one can observe interference fringes—output power variation (as shown theoretically in Fig. 2.15 on page 44). By measuring the maximum observed signal and the contrast of the fringes, it is possible to evaluate the quality of the sample.

### 3.2.1 Setup

The setup for the stretch interferometry is shown in Fig. 3.14. It is basically the pulling setup (Fig. 3.1), only the burner is not used. Light from a free running single-mode 852 nm laser diode is coupled into the input pigtail of the sample. The output pigtail is connected to a photodiode, and the signal is measured with a digital oscilloscope. The stretcher stage is usually moved at the speed of  $1 \mu\text{m/s}$  so that the oscilloscope signal can be directly converted to elongation in microns.

### 3.2.2 Experiment

My SOMMI samples normally have the waist length of 2...5 mm. After pulling, the waist exhibits a small sag caused by the flow of gas in the flame (because,

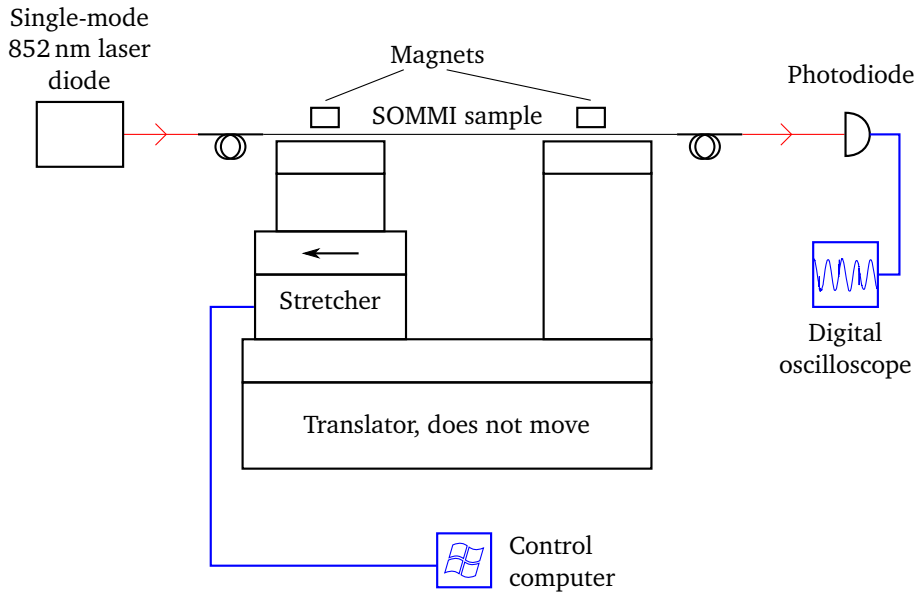


**Figure 3.14:** Stretch-interferometry setup.

during tapering, the fibre is pulled a little more than just by the stages). The thinner the waist, the larger is this sag. To straighten the samples, we stretch them a little after switching the burner off. As long as the waist is sagging, the stages can be moved apart without actual elongation of the fibre, therefore the photodiode signal remains constant. A movement of 20...30  $\mu\text{m}$  is usually enough to straighten the waist. As soon as the sag disappears, further movement of the stretcher results in the actual elongation of the sample, which can be immediately seen as the variation of the output power according to Eq. (2.12):

$$I(\Delta L) \sim A + B \cos \left( \frac{2\pi}{\lambda} (L + \Delta L) \Delta n_{\text{eff}} \right),$$

where  $\Delta L$  is the fibre elongation. The photodiode response recorded during stretching is shown in Fig. 3.15.

We discovered experimentally that the samples, which have the waist length of 2...5 mm, can be stretched by approximately 400...500  $\mu\text{m}$  before they tear. The oscillation period is about 5  $\mu\text{m}$ . Therefore, to perform the stretch-interferometry, I usually elongated the fibre by 50...100  $\mu\text{m}$ , which was not more than 5 % of the waist length and less than 0.2 % of the total sample length. Therefore it is safe to assume that the elongation is elastic.

To check the last assumption, I also performed multiple stretch-destretch cycles and verified that the harmonic signal fully reproduced itself in the de-stretching measurement. Of course, there may be a long-term influence on the fibre, which cannot be detected using this method. Therefore I always de-stretched the fibre to the original straight state before fixing it in the fibre holder.

### 3.2.3 Results and analysis

Figure 3.15 shows the stretch-signal for one of our samples. By fitting a sine wave to this curve, a fringe period of 3.95  $\mu\text{m}$  is obtained. This particular sample was designed to have a waist of 1.3  $\mu\text{m}$  diameter, 2 mm waist length, and 16 mrad tapers. Simulation for this shape according to Sec. 2.5.4 gives the fringe period of 4.1  $\mu\text{m}$  (4 % deviation from the measured value).

Table 3.3 shows the result of analysis of 12 samples pulled with almost the same parameters: 16 mrad tapers and 1.3  $\mu\text{m}$  waist diameter. In all cases but one the simulated result is within the error-bar of the measured one.

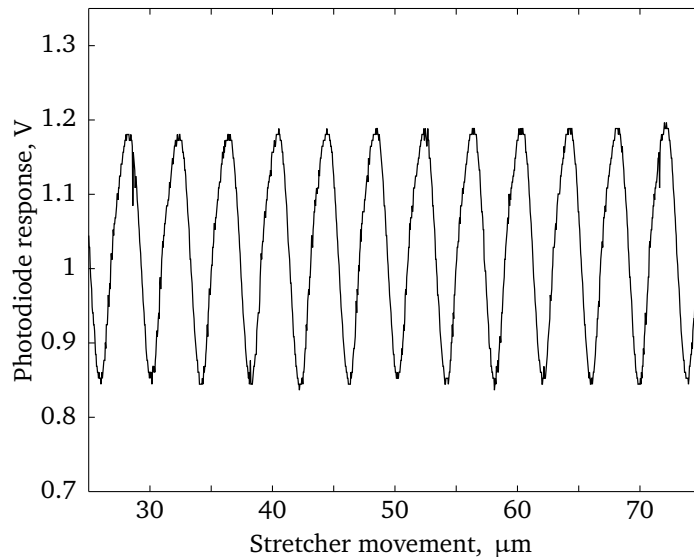


**Figure 3.15:** Stretch signal for sample 166 (waist length 2 mm, flame width 1 mm). Wavelength 852 nm. Spikes are due to mode hops of the free-running diode laser.

**Table 3.3:** Stretch-interferometry fringe period: experiment vs. simulation. Tapers: 16 mrad, waist: 1.3  $\mu\text{m}$ . Flame width (second column) is the value used to program the pulling machine. Simulated for silica in air. Fibre used in experiment: SM800.

Waist length, mm	Flame width, mm	Measured period, $\mu\text{m}$	Number of samples	Simulated period, $\mu\text{m}$
2	1.0	4.0(1)	2	4.1
3	0.7	3.9(3)	6	3.8
3	1.0	3.9(1)	1	4.0
5	0.7	3.3(1)	1	3.7
5	1.0	3.8(1)	2	3.8

Let's also consider a different matter. Figure 3.16 shows a measured stretch-interferometry signal of three of our samples pulled with the same program: 16 mrad taper, waist of  $\varnothing 1.3 \mu\text{m} \times 2 \text{ mm}$ , flame width 1 mm. Figure 3.16(a) corresponds to Fig. 3.15. The signal is almost perfectly harmonic. The contrast, defined as  $(\max - \min)/(\max + \min)$ , is not very high, about 16 %.

In Fig. 3.16(b) (sample 167), the maximum contrast is very high, about 90 %. However the signal is strongly distorted. The fringe period— $7.4 \mu\text{m}$ —is completely different from samples 166 and 168 ( $3.95$  and  $3.84 \mu\text{m}$  respectively). Note also the change of the vertical scale: the maximum transmission of this sample is about three times lower than for the two other samples (the initial—before pulling—signal in all three cases was the same, 1.4 V). This sample was not considered in Tab. 3.3.

Finally, sample 168 (Fig. 3.16c) exhibits intermediate performance. This comparison shows that, despite trying to produce the same samples, I received three quite different ones. Most probably, in sample 168 (Fig. 3.16c), some unwanted modes were excited due to the fibre misalignment. The fringe period for this sample ( $3.84 \mu\text{m}$ ) is very close to the expected one ( $3.8 \mu\text{m}$ ), therefore the diameter cannot be very wrong.

With sample 167 (Fig. 3.16c), the period is much larger, indicating a smaller  $\Delta n_{\text{eff}}$  and thus a larger waist diameter. This can also explain the strong presence of other modes, resulting in the signal distortion. The general conclusion from this test is that the pulling machine is not always performing as expected, but the stretch-measurement allows to identify bad samples immediately after the production.

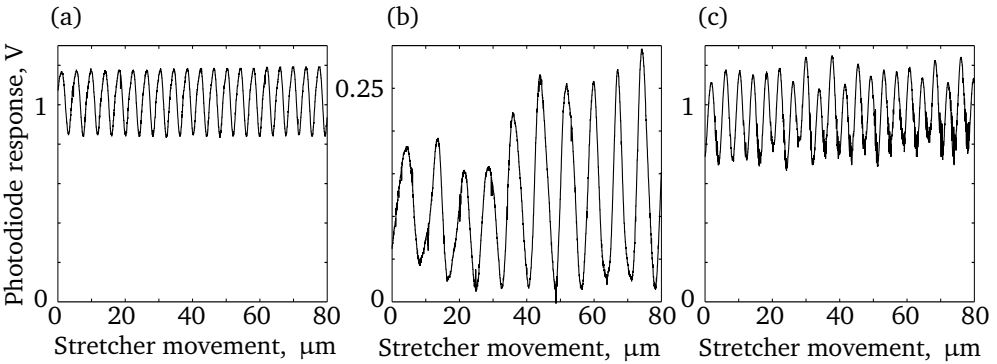


**Figure 3.16:** Stretch signal for samples 166 (a), 167 (b), and 168 (c).

### 3.3 Handling

Since OMF samples exhibit a strong evanescent field, they should be protected from uncontrolled contact with other objects. Also, to function as described in this work, an OMF should be straight and suspended in air.\* Therefore, right after pulling, we fix our samples to a rigid frame at two points outside the tapered region.

For experiments carried out in our group, the samples should be accessible for:

- measurement in a scanning electron microscope [74];
- putting into a hot vacuum chamber with caesium [91];
- depositing molecules onto the waist from the crucible underneath the fibre and with the drops of solution from above [92];
- submersion into a bath with liquids (Chap. 4);
- cleaning the fibre by immersion in piranha solution [93] and dripping organic solvents on the fibre waist and tapers;
- side-illumination for scattering measurement (Sec. 3.1.5.4).

To prevent destruction of samples, a fibre holder should also be easy to handle, both when fixing the sample in the holder after pulling and during the experiments.

As already mentioned, the pulling machine was moved from Bonn in 2007 and has since then been in use in the research group of Arno Rauschenbeutel, first in Mainz and then in Vienna. This has created two specific requirements to the sample handling procedure. First, since we could not rely on manufacturing the samples as we need them, we had to make sure that our samples can be stored for weeks and even months after manufacturing. Second, the samples should be transportable by train and airplane.

---

\*This is not always the case; for example, G. Brambilla and colleagues are working with OMFs, coiled into microresonators and coated with Teflon for protection [90].

### 3.3.1 Fibre holder design

To meet the above requirements, I developed a special fibre holder. It evolved in the course of the project; figure 3.17 shows the current design, version 4.5. The holder consists of a frame, to which the sample is fixed, a complex-shaped cover, and three lids, bottom, side, and top. Besides protecting the fibre sample, the cover keeps the fragile stripped parts of the fibre straight and fixed (via clamping of the coated fibre). Thus, only the coated, protected fibre extends at both ends of the closed holder. In addition, the cover adds stability to a relatively thin-walled frame during transportation. The cover and the frame are designed in such a way

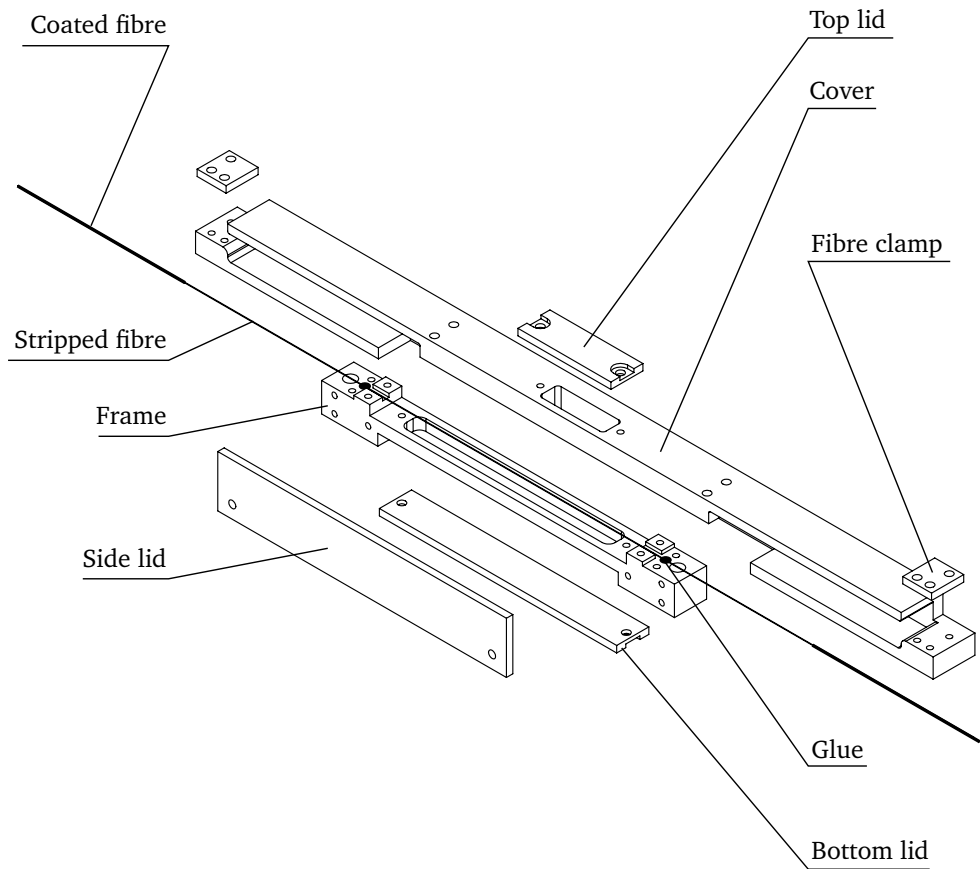


**Figure 3.17:** Microfibre holder. The untapered ( $125\text{ }\mu\text{m}$ ) stripped pigtails are glued or clamped to the ends of the frame. The micrometre-diameter waist is suspended above the centre of the frame. After the sample is fixed to the frame, it is removed from the pulling machine and closed from all sides with a cover and three lids. Each of these elements can be later removed in the lab for experiments with the sample. Finally, the coated parts of the fibre are clamped to the cover ends, for safer transportation and storage.

as to prevent accidental destruction of the sample while closing and opening the holder.

The top opening in the cover is provided for visual inspection of the sample without removing the cover (and thus exposing the sample to mechanical risks and dust). We have also used it to detect light scattered from the waist.

The frame is shown in Fig. 3.18. It is designed to be compatible with all our experiments, both in its shape and in how it is made. For example, to make it vacuum-compatible, there are no trapped volumes, even when the lids or the covers are mounted, to avoid virtual leaks. Also, unlike most parts produced by our workshop, the frame is not sand-blasted, to keep the surface smooth for easier cleaning and faster vacuum chamber evacuation. For illustration of its use in experiment, see Fig. 4.10 on page 91.

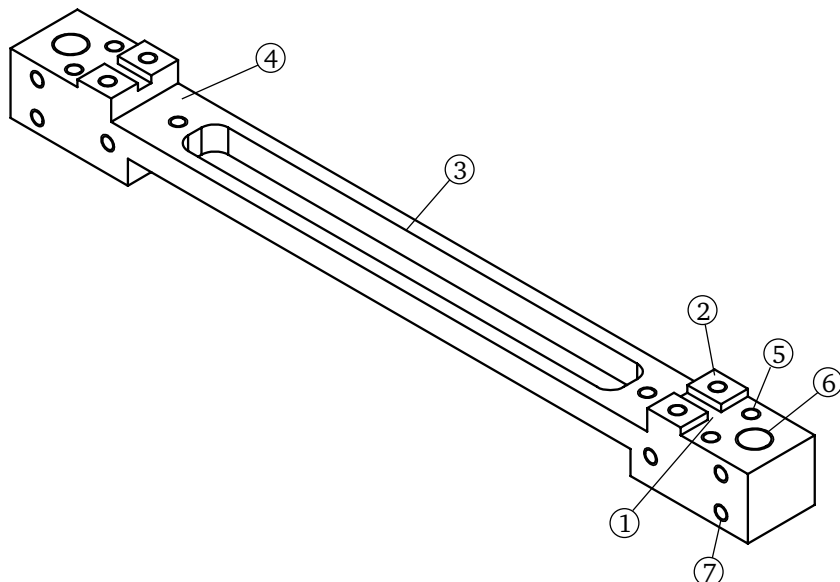


**Figure 3.18:** OMF-holding frame. Surface (1), to which the fibre is glued, is 1 mm below the topmost surface (2), thereby protecting the fibre when the cover is being removed or fixed. Large hole (3) in the frame provides access to the waist and most of the taper from below, even with the cover closed. Most of the frame (4) is 2 mm lower than the sample surface (1), allowing access to the fibre from all four sides when the cover is removed. The sample can be either glued to the frame surface (1) or clamped to it (two M2 holes are provided for it at each end, pos. 5). Two M4 holes (6), which are always accessible from the bottom, are provided to fix the holder in the pulling machine, on an optical table using standard optomechanical components and posts, and in the vacuum chamber. M2 holes (7) are provided to fix additional support elements for strongly bent samples in the vacuum chamber. The frame is vacuum compatible: there are no trapped volumes, even with all lids and the cover mounted.

Figure 3.19 shows the closed holder. In comparison to the holders used in some other OMF groups (Brambilla, SOTON, UK; Rauschenbeutel, TU Vienna, Austria; Pinto, Aveiro, Portugal), ours, when closed, is almost completely sealed from the outside environment, providing both mechanical and dust protection.

Some fine details on sample fixation in the holder and our OMF transportation experience are given in appendix D.

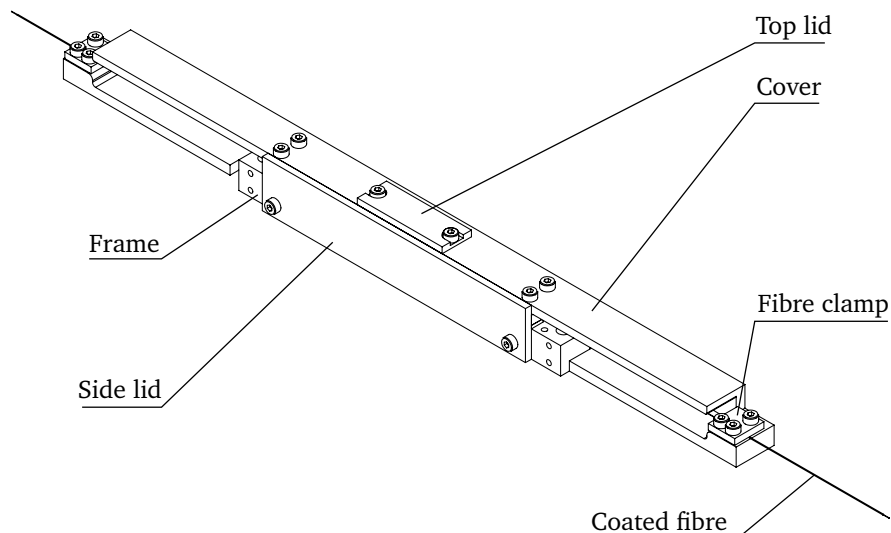


**Figure 3.19:** Closed fibre holder. The side, top and bottom (invisible) lids can be removed for partial access to the sample. If needed, the clamps can be loosened and the whole cover removed.

### 3.3.2 Using samples in experiments

#### 3.3.2.1 On optical table

Depending on the experiment, the fibre holder with a sample can be used completely closed or with the cover and/or some lids removed. For example, Fig. 3.20 shows scattered blue-light, produced by the second harmonic generation, observed through the top opening in the cover. The frame has an M4 hole at each end, accessible from the bottom, for fixing the holder to a pedestal post or other optomechanical components.

#### 3.3.2.2 With liquids

To immerse a sample into a liquid, the frame with the sample, without any lids or cover, is fixed to a 3D translation stage and a specially-designed Teflon bath is fixed underneath on a 3D tilt-rotate stage. The frame is then lowered so that the sample gets into the bath. This experiment is described in chapter 4.

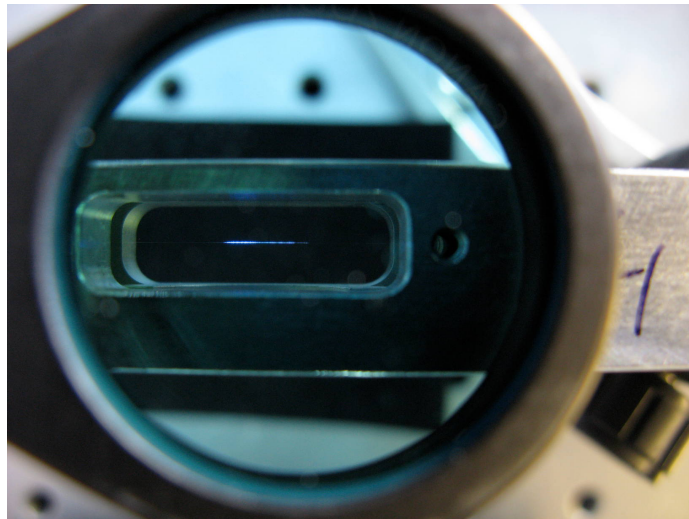


**Figure 3.20:** Blue SHG light scattered in the OMF waist and observed through the top opening of the fibre holder through an IR-block filter (photocamera is sensitive to the IR pump light). The bottom opening (this is version 2 of the fibre holder, with the bottom opening as large as the top one) is also open, to have a black background for the waist.

### 3.3.2.3 For scattering measurement

The scattering measurement (Sec. 3.1.5.4) requires that the sample be illuminated from one side, perpendicularly to the fibre, and the scattered light be observed on a screen on the other side from the fibre. To achieve high measurement accuracy, as large scattering angle as possible should be accessible for observation.

For this, we fix the frame, with the cover and the lids removed, on a 2D translation stage such that the laser beam is incident horizontally and hits the fibre through the bottom opening in the frame (Fig. 3.21). The 2D stage is used to align the sample to the laser beam and to scan along the sample. The open frame offers more than  $\pm 90^\circ$  scatter angle observation.

### 3.3.2.4 In vacuum chamber

In the vacuum chamber, depending on the exact experiment, the samples are fixed either completely open (with a bare frame) or with some lids left on (to control the incidence of evaporated material onto the sample or to facilitate mounting several samples at once). The frame is fixed in the chamber using a special mount. Since one pigtail should be significantly bent to exit the chamber, we are using a special frame extension, which fixes the fragile bare fibre and prevents its breakage inside the chamber [91].

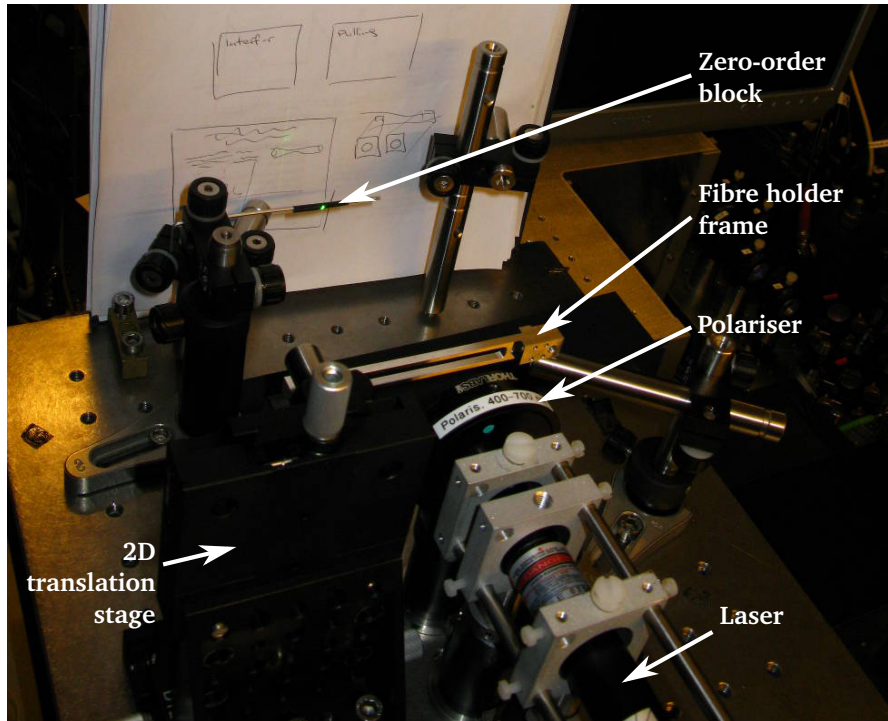


**Figure 3.21:** Fibre holder frame in the scattering measurement setup. The screen is not shown here, it will be placed in the position of the white paper sheet in this figure. See Fig. 3.12 for what can be seen from behind the screen and Fig. 3.11 on page 66 for the setup scheme.

### 3.4 Conclusions

The SOMMI idea, described in chapters 1 and 2, indeed works. The signal-to-noise ratio and the contrast are more than sufficient for data extraction. Some irreproducibility in the manufacturing procedure was observed. Interferometer samples seems to be more sensitive to manufacturing imperfections than our spectroscopic and other adiabatic samples, and could be used to test and optimize the pulling machine in the future. The contrast should be increased; for this, the precise mode coupling calculation should be implemented.

To characterize the samples, several techniques were employed. For non-interferometric samples with the waist diameter about  $0.5 \mu\text{m}$ , the newly developed harmonic generation-based method turned out to be very efficient. For thicker samples, the scattering method seems to be an optimal choice. It should still be further developed so that the whole sample shape could be measured. The stretch-test makes it possible to check the sample performance right after manufacturing, and is therefore suitable for post-production testing. However it reveals little information about the sample shape. For most samples, the results of the stretch-interferometry agree with the simulation results, thereby partly

confirming the theory developed in chapter 2.

Finally, a reliable sample handling procedure was developed. A special multipurpose fibre holder was designed, and proved to work well throughout the sample lifetime, from manufacturing to transporting to experiments in various setups and environments.



# 4

## CHAPTER

# Spectral interferometry

In this chapter, I describe the spectroscopic measurements I have performed with my samples. The goal of these measurements was to verify the model developed in chapter 2 and to develop the experimental routine for handling OMF samples in liquids.

## 4.1 Optical setup

The setup I used in my experiments is shown in Fig. 4.1. It consists of a fibre-coupled white-light source, an OMF sample, and a fibre-coupled spectrometer. As the light source, I used the Avantes AvaLight-HAL or Ocean Optics LS-1 lamps. The Avantes lamp couples at least twice more light into the same fibre (on the order of 100 nW in the range of 700...1000 nm for the SM800 fibre) than the one from Ocean Optics, but was not always available. As the detector, I used an Avantes AvaSpec-ULS2048x16-USB2 spectrometer with UA grating (200–1160 nm) without the entrance slit or a scanning optical spectrum analyser (OSA) Ando AQ-6315A. The OSA offers superior sensitivity and resolution

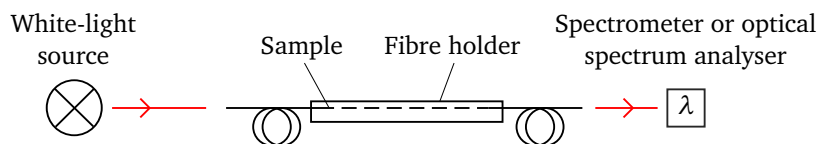


**Figure 4.1:** Setup for spectral interferometry. The light source and the detector are fibre-coupled, so no additional optics is needed. The fibre holder is mounted on the optical table using standard optomechanical components.

but is much slower than the spectrometer. One measurement (obtaining one spectrum) with the OSA was several seconds to several dozens of minutes long. In liquids, due to the strong dependence of their refractive index on temperature, unavoidable small temperature fluctuations resulted in significant changes of measured spectra. Therefore OSA could not be used for in-liquid measurements and was used only for in-air measurements in a temperature-stabilized lab room (temperature fluctuation was measured and did not influence the signal significantly). For the in-liquid measurements, I used the spectrometer, which allowed practically real-time measurements (several spectra per second).

Both the light source and the spectrometer are designed to be directly fibre-connected using the standard SMA (white-light lamps) and FC (spectrometer and OSA) fibre connectors. Since our samples have non-terminated pigtails, we use bare fibre adapters (Newport F-AM-SMA for SMA and F-AS-FC for FC connections). The sample pigtails were always 8-degree cleaved (using an Ilsintech MAX CI-08 angled cleaver) before connecting to the instruments, to minimize noise due to reflections from the fibre ends.

## 4.2 Automated spectrum acquisition

To minimize the influence of ambient condition changes and to be able to estimate the random measurement errors, I recorded multiple spectra for each measurement. With the spectrometer, such recording could be done automatically, using the built-in functionality of the control software. To read the recorded binary spectra files, a special program was written [94].

The OSA was connected to our institute Ethernet network using a Prologix GPIB-Ethernet adapter and could be controlled directly from Matlab. To protect the instrument from possible hacker attacks over the network, a hardware firewall (D-Link DIR-100) was used.

## 4.3 Spectrum analysis

### 4.3.1 Characteristic shape: simulation

In Fig. 4.2, the dotted line corresponds to the spectral response of a SOMMI, calculated according to the model developed in chapter 2. It exhibits two characteristic features: a zero-dispersion point and a non-linear chirp. To quantitatively compare the results of simulation and experiment, we should extract numbers from these features.

The spectrum in Fig. 4.2 can be approximated by a function

$$\begin{aligned} I_{\text{theor}} &= 0.5 + 0.5 \cos(\phi) \\ &= 0.5 + 0.5 \cos \left( c_0 + \frac{c_1}{2}(\lambda - \lambda_0)^2 + \frac{c_2}{3}(\lambda - \lambda_0)^3 + \dots \right), \end{aligned} \quad (4.1)$$

so that the fringe frequency is

$$f(\lambda) = \frac{\partial \phi}{\partial \lambda} = c_1(\lambda - \lambda_0) + c_2(\lambda - \lambda_0)^2 + c_3(\lambda - \lambda_0)^3 + \dots \quad (4.2)$$

Thus the zero-dispersion wavelength (ZDW)  $\lambda_0$ , the chirp coefficients  $c_i$ , and the phase-offset  $c_0$  are sufficient to describe the simulated spectrum. I find these parameters by RMS-fitting the  $I = 0.5 + 0.5 \cos(\phi(\lambda))$  function to the simulated spectrum using the `fminsearch` function of Matlab [95], which is an implementation of the Nelder-Mead simplex search method [96]. In practice, the 4th order chirp (with non-zero coefficients  $c_1$  to  $c_4$ ) is sufficient to obtain the RMS error of the fit less than 1 %, but I used the 5th order chirp for an even smaller error. In Fig. 4.2, the solid line shows the fit obtained using the 3rd order chirp.

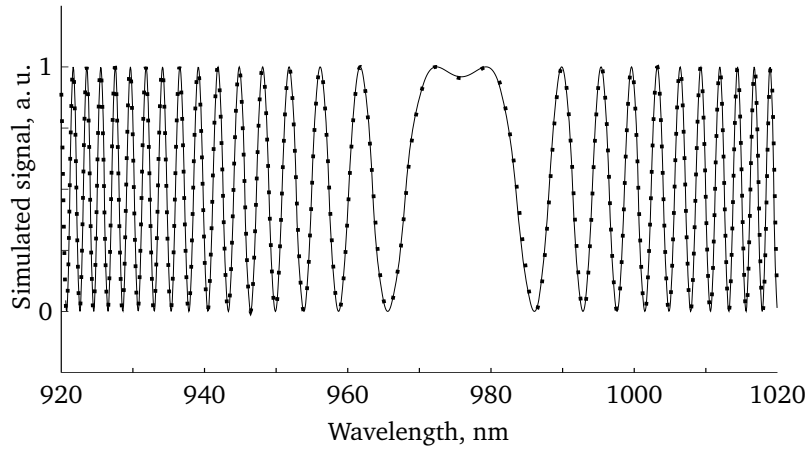


**Figure 4.2:** Calculated spectral interferometer response of a silica SOMMI with a  $\varnothing 1.23 \mu\text{m} \times 2 \text{ mm}$  waist in air (dotted line) and a 3rd order chirp fit (solid line).

### 4.3.2 Characteristic shape: experiment

Figure 4.3 shows a sample 168 spectrum measured with the OSA. Interference fringes can be observed between about 920 and 1020 nm. The shape of this signal differs from the simulated signal in Fig. 4.2 in that it has a lower contrast, is slightly tilted, the contrast is not constant, and there is some noise. Lower contrast is due to not 1:1 splitting of the interference modes, already known from chapter 3. The tilt is the result of the non-uniform spectrum of the light source mainly. The contrast variation is due to the finite resolution of the OSA.

To extract useful data from this measurement, I again perform the fitting. For this, a few parameters are added to Eq. (4.1): the offset, the amplitude, and the tilt:

$$I_{\text{exp}} = \text{offset} + \text{tilt} \times (\lambda - \lambda_0) + \text{amp} \times \cos \left( c_0 + \sum_i \frac{c_i}{i+1} (\lambda - \lambda_0)^{i+1} \right). \quad (4.3)$$

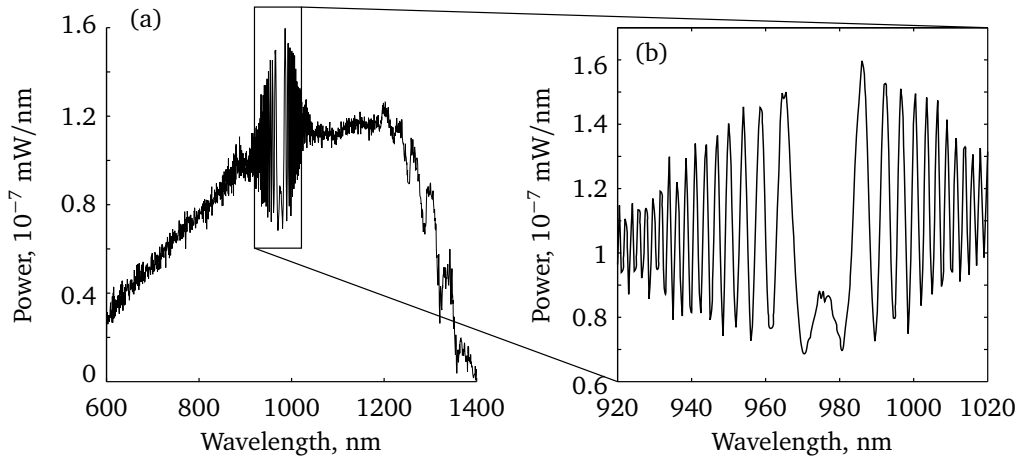


**Figure 4.3:** Measured spectral response of sample 168. Measured with OSA, scan time 2 minutes.

Figure 4.4(a) shows such function (dashed line) fitted to the experimental spectrum (solid line). Note that due to the noisiness of the experimental signal, it does not make sense to use as many chirp parameters here as for the simulated signal. Depending on the signal-to-noise ratio, three or four  $c_i$  parameters (not counting  $c_0$ ) are enough. For example, the measured spectra of sample 168 were fitted with four parameters (Tab. 4.1), while those of sample 165—with only three, and still the third one was determined with a large error (Tab. 4.4).

The limited contrast of the experimental curve at high frequency stems from the finite resolution of the spectrometric instrument. It is easier to explain for the spectrometer. The physical limiting factor there is the number of pixels in its linear CCD detector. When the signal frequency gets too high, there are not enough detector points to properly sample the varying intensity, and the contrast decreases. Theoretically, when the number of points reaches one per oscillation, the contrast becomes zero. The same happens in the OSA, but the discretization there is due to a step-scanning over wavelengths.

To properly simulate this situation, I convolve the function of Eq. (4.3) with a rect-function, so that the fitting function becomes

$$I_{\text{exp, limited}} = [I_{\text{exp}} * \text{rect}](\lambda).$$

The width of the rect-function should, in principle, be directly determinable from the resolution of the spectrometric instrument. However, since I do not exactly know how the nominal resolution is defined in the OSA and in the spectrometer, I have just found this width empirically, by adjusting it until a good fit was obtained for several spectra. Note that this is not a fit parameter, since it remains constant for all spectra taken with the same resolution setting of the instrument. Figure 4.4(b) shows the fit with a filtered function, with the rect-width of 1.5 nm.

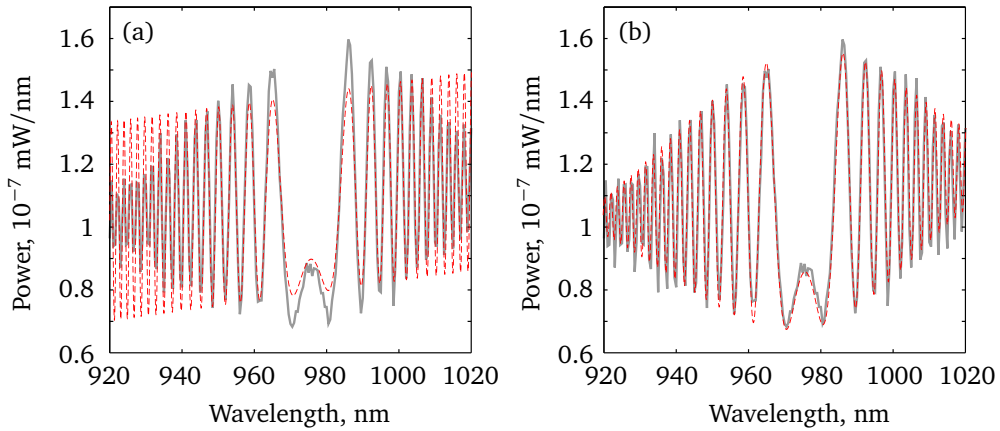


**Figure 4.4:** Measured spectrum of sample 168 (solid line; same as in Fig. 4.3b) and the fitted curve (dashed line). (a) With tilt, offset, and corrected amplitude. (b) With additional filtering to take limited resolution into account (convolved with a rect-function of 1.5 nm width).

#### 4.3.3 Data processing

Figure 4.5 illustrates the data analysis process after the spectra have been recorded. In this particular measurement, 15 spectra were taken one after another.

Small variations in the ambient temperature lead to changes in the refractive index of glass and air and to small fluctuations in the fibre holder length. A large change would shift the whole signal and change the chirp, however small residual changes only influence the zero-dispersion point phase  $c_0$  (Fig. 4.5a). Phase fluctuations make it impossible to use spectrum averaging. Instead, the above-described fitting procedure is applied to each taken spectrum individually, and the parameters  $\lambda_0$  and  $c_1, c_2$ , etc. are obtained. Figure 4.5(b) shows the

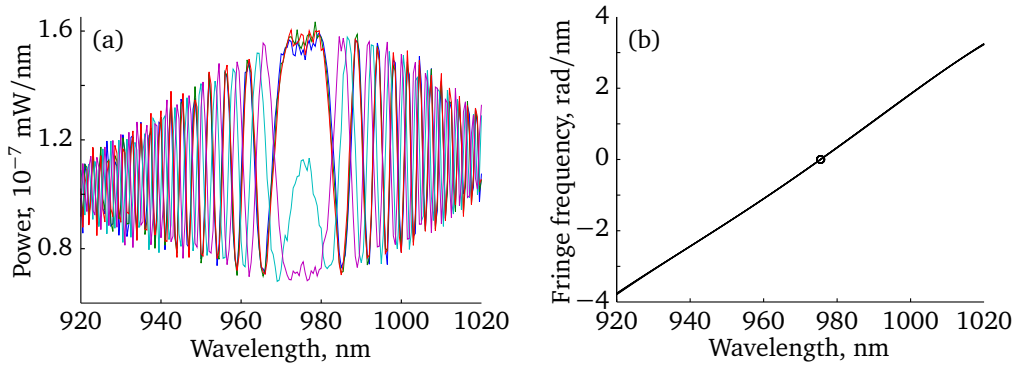


**Figure 4.5:** (a) Raw scans of sample 168 (5 out of 15 spectra shown). (b) Chirp fitting result (4th order chirp, 1.5 nm filtering). All 15  $f(\lambda)$  curves are shown (overlapping), with the circles marking the zero-dispersion point at 975.49(8) nm.

**Table 4.1:** Fit parameters for spectral interferometry signal of sample 168 in air. 4th-order chirp and 1.5 nm filtering were used for fitting.

Fit parameter	Value
$\lambda_0$	975.49(8) nm
$c_1$	0.073(1)*
$c_2$	$1.23(4) \times 10^{-4}$
$c_3$	$-1.4(1) \times 10^{-6}$
$c_4$	$-3.6(3) \times 10^{-8}$

\* According to Eq. (4.2), the units of  $c_i$  are [rad·nm $^{-(i+1)}$ ]. I omit them in the following.

$f(\lambda)$  curves, calculated according to Eq. (4.2) and plotted for all 15 spectra. Obviously, the curves lie very close to each other, which indicates that, despite somewhat noisy spectra, this method works well. It also confirms that small ambient fluctuations lead primarily to changes in the phase and do not influence the chirp significantly. The obtained zero-dispersion wavelength and the chirp parameters are given in Tab. 4.1.

#### 4.3.4 Use of zero-dispersion point for diameter determination

The zero-dispersion wavelength (ZDW) varies significantly with the sample waist diameter (Fig. 4.6). Therefore, unless the sample diameter is known precisely, it makes no sense to compare the ZDW between the experiment and the simulation. For example, the waist diameter of sample 168 was measured with the scattering method to be 1.26(6)  $\mu\text{m}$ . The 0.06  $\mu\text{m}$  error (which is close to the 0.05  $\mu\text{m}$  value determined for this method in [88]) corresponds to the error of 47 nm in the ZDW. Taking into account the precision, with which the ZDW can be determined experimentally (see Tab. 4.1), it makes sense to use it to verify the sample diameter.

The experimental ZDW for sample 168 is 975.49(8) nm (Tab. 4.1), which corresponds to the diameter of 1.2294(1)  $\mu\text{m}$  (Fig. 4.6). One should approach this excellent precision with care, because other unknown parameters, such as the taper shape and the waist length, also influence the ZDW. However, of these parameters, the ZDW is by far most sensitive to the waist diameter. By changing the diameter just a little, within the error-bars of other measurements, one can satisfy the measured ZDW. That's why I suggest that ZDW can be used, even if with some care, to determine or at least cross-check information about the sample diameter.

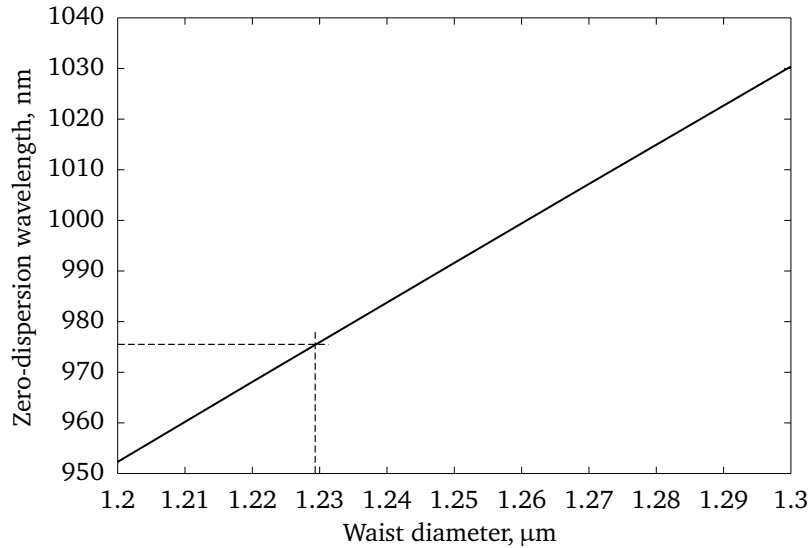


**Figure 4.6:** Zero-dispersion wavelength of simulated interference signal vs. OMF waist diameter. The average slope of this curve in this plot is 783 nm/μm. The dashed lines mark the zero-dispersion point derived for sample 168.

**Table 4.2:** Comparison of design and measured diameter for sample 168.

Diameter, μm	
Design	1.3
ZDW-derived	1.2294(1)
Stretch-derived	1.25(5)
Scattering-measured	1.26(6)

## 4.4 Spectral interferometry in air

The waist diameter values obtained using the stretch-, scattering-, and ZDW-based methods for sample 168 are listed in Tab. 4.2. Figure 4.7 compares the chirp of the experimentally measured signal (Fig. 4.5a) and of the simulated interference spectrum (Fig. 4.2). For the simulation, I assumed the diameter of the sample to be 1.23 μm, determined based on the ZDW.

The error-bars of all chirp parameters (Tab. 4.1) are too small to be seen in Fig. 4.7. On the other hand, the error between the theoretical and experimental chirp is apparently quite large: the  $c_1$  parameter values are 0.067 in theory and 0.073 in experiment. Also, sample 168 was tested using stretch-interferometry. The fringe period was found to be 3.8 rad/μm, while the theoretical value for 1.23 μm waist diameter is 4.12 rad/μm. From this I conclude that it is not the diameter of the waist alone that is not known exactly, but also, probably, the taper shape or the waist length. Although it could be measured with the scattering

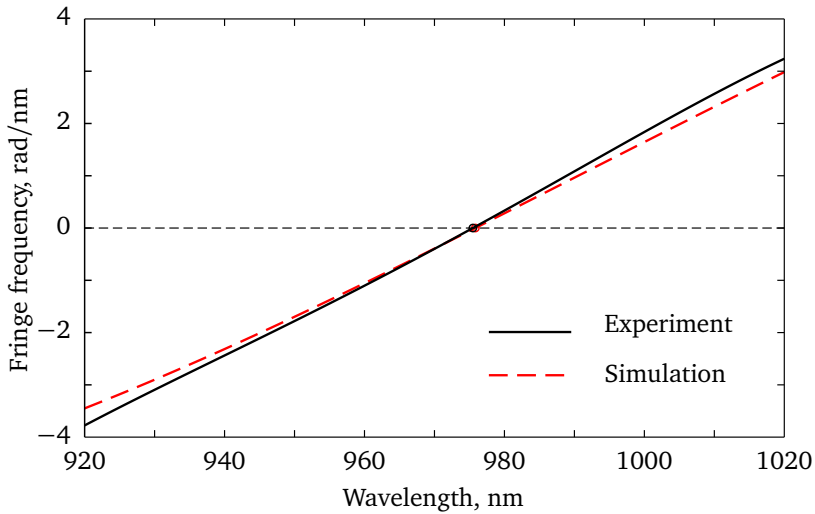


**Figure 4.7:** Spectral interference fringe frequency. Experimental curves (solid; all 15 curves are shown, overlapping) for sample 168. Simulated curve (dashed) is obtained for a sample with  $\phi 1.23 \mu\text{m} \times 2 \text{ mm}$  waist, 16 mrad tapers, silica in air (like sample 168, but with thinner waist, see text).

method, it requires taking and processing a large amount of data and can only be reasonably done with an automated setup. This should still be built.

I have measured spectral interference for 15 samples in total, however only one more sample—165—was also measured with the scattering method and tested with stretch-interferometry. For this sample, the design diameter and the diameter values obtained with different methods lie quite close to each other (Tab. 4.3). However, the chirp curve still has significantly different slope values  $c_1$  in the simulation and measurements (Fig. 4.8(b), Tab. 4.4). This to some extent confirms the suggestion made for sample 168, that the whole sample shape influences the spectra. Note that the spectra obtained with this sample were very noisy: compare Fig. 4.5(a) and Fig. 4.8(a). Nevertheless, the ZDW was again determined with a very small error of 0.07 nm.

The other 13 samples, designed for interferometry in air, show a similar behaviour but their diameter was not measured using the scattering method. The

**Table 4.3:** Comparison of design and measured diameter for sample 165.

	Diameter, $\mu\text{m}$
Design	1.3
ZDW-derived	1.2827(1)
Stretch-derived	1.25(5)
Scattering-measured	1.27(1)

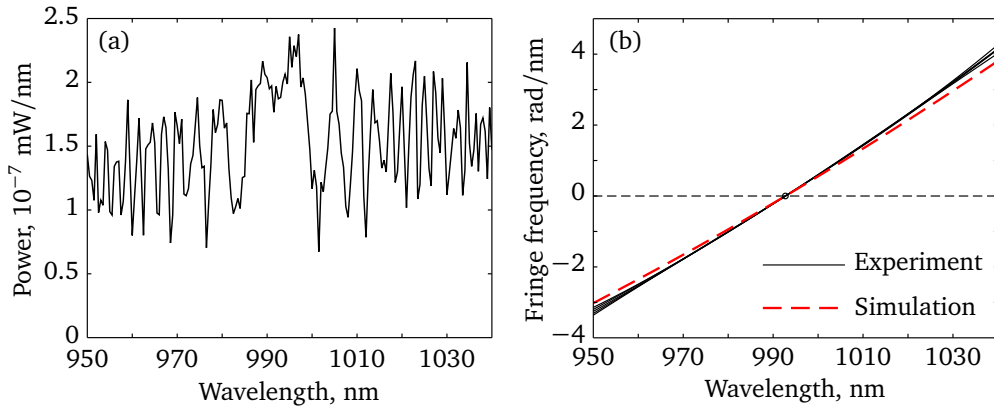


**Figure 4.8:** (a) Experimental spectrum taken with sample 165. Due to its noisiness (cf. Fig. 4.5), only one spectrum is shown. (b) Fringe frequency analysis of sample 165. Note that despite noisiness of the spectra, the fitting algorithm quite well determines the ZDW and the first chirp coefficients (cf. Tab. 4.4).

**Table 4.4:** Frequency chirp parameters for sample 165.

Fit parameter	Simulation	Measurement
$\lambda_0$		992.76(7) nm
$c_1$	0.0754	0.0811(6)
$c_2$	$1.13 \times 10^{-4}$	$1.3(1) \times 10^{-4}$
$c_3$	$9 \times 10^{-8}$	$9(86) \times 10^{-8}$

ZDW-determined diameter values are within  $\pm 5\%$  from  $1.3 \mu\text{m}$ , as expected from the pulling machine characterisation (Sec. 3.1.5.3, page 62).

## 4.5 Interferometry in liquids

The in-air interferometry results have confirmed the validity of the developed spectral-interference model, at least to the degree to which the shape of the OMF is known. However, its high sensitivity to shape errors makes it impossible to do a better analysis: Even if only the ZDW was considered, its value obtained in the spectral measurements could only be cross-checked but not really verified with any other method. One possible approach to further validate the model is to perform measurements with the same sample but a different external refractive index. Then the sample diameter could be derived from the ZDW measurement with one  $n_{\text{out}}$ , and this value could be used for all other simulations. For this, a sample can be immersed into different liquids.

Such experiment is also interesting from the practical point of view: it requires to develop the handling procedure for OMF samples in liquids, and can be beneficial, for example, for microfluidics.

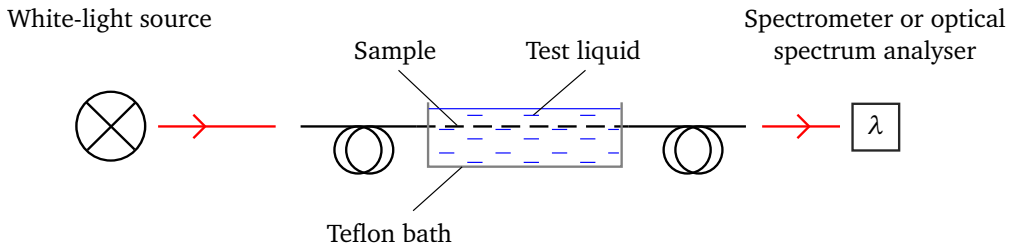


**Figure 4.9:** In-liquid interferometry setup.

#### 4.5.1 Setup

The setup I used for this experiment is shown in Fig. 4.9 and 4.10. It is equivalent to the in-air setup but contains additionally a bath, into which the central part of the sample (including the waist and the tapers) can be immersed. The bath is made from polytetrafluoroethylene (Teflon). It is inert towards organic solvents, which we use for cleaning. Besides, the well-known non-stickiness of Teflon makes it easier to blow dust particles from the bath (highly clean and high pressure Chemtronics UltraJet duster was used) as well as minimizes chances to break a sample if it accidentally touches the bath wall. The bath has slits at both ends, which are large enough for the fibre to pass through it but too small for liquids to drip out.\*

The bath is fixed on a 3D tilt-rotate stage and can be aligned under the fibre holder (see Fig. 4.10b). The fibre holder is fixed to a 3D translation stage, so that the sample can be positioned above the slits and lowered into the bath.

After the measurement, the sample is lifted from the bath and moved away from it. The bath is emptied, washed, dried, and filled with a new liquid. The sample is also washed by dripping acetone and ethanol onto it, and dried. Thus I could make sure that in each measurement the sample was immersed into a chosen liquid. It was also possible to refill the bath without lifting the sample from it, which was used for quickly evaporating liquids.

**Sample destruction prevention** Working with OMF in the bath requires special care. The Teflon baths were produced by milling. Tiny hairs of Teflon could be observed in the bath, especially in the end slits. When the sample is moved up and down, it can be hooked by these hairs and broken. After breaking a few samples, I have flame-processed the end-slits of the baths with a small gas torch so that most of the hairs were removed (checked under microscope).

---

\*The bath was initially designed for use with organic solvents. The slit width of 0.7 mm was experimentally found for the combination of Teflon and these liquids. Eventually, due to the high uncertainty of the solvents dispersion and their quick evaporation, I switched to Cargille liquids. For them, the 0.7 mm slit width was too large. Still, the measurements could be performed with a small amount of liquid at the bottom of the bath.

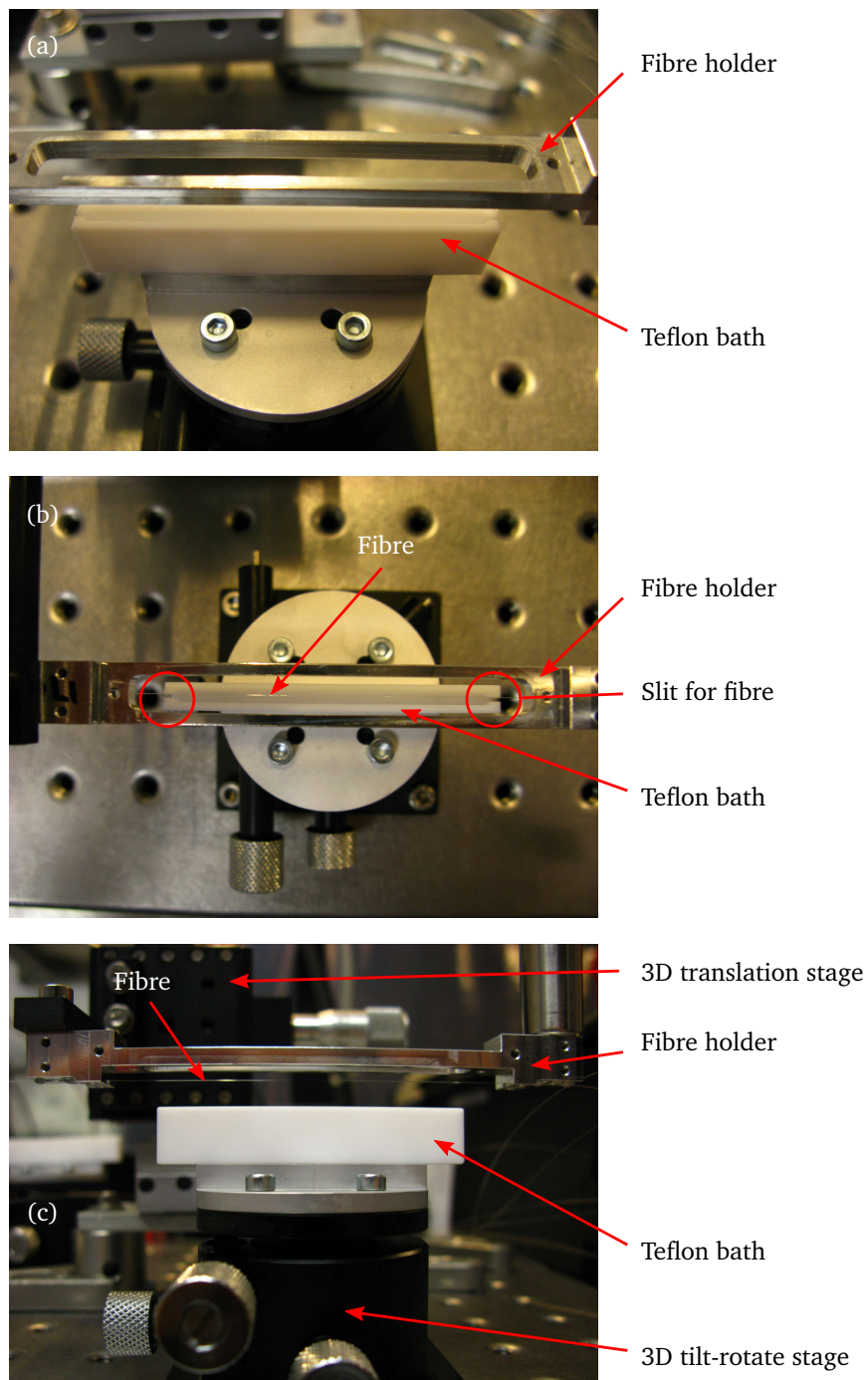


**Figure 4.10:** Setup for spectral interferometry in liquids. (a) General view. The holder is fixed to a 3D translation stage upside down (cf. Fig. 3.18 on p. 75). (b) Top view. The bath and the fibre holder are aligned using the rotation and translation stages. The sample can be immersed into the bath due to the narrow slits at the ends of the bath. (c) Front view. The fibre can be seen under the holder.

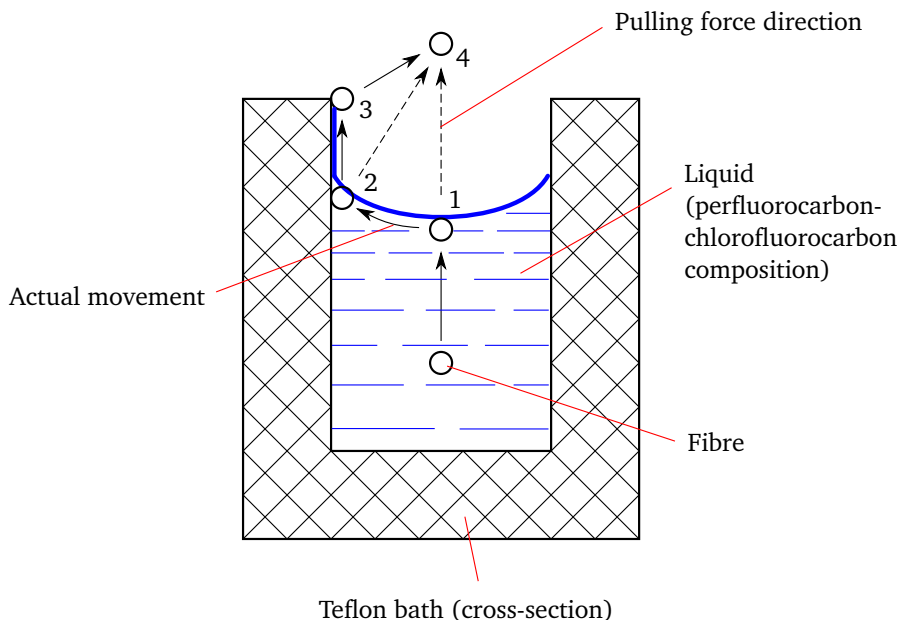


**Figure 4.11:** Lifting OMF from the bath with a liquid. The liquid composition is very similar to Teflon, therefore it wets the bath walls. The OMF is continuously pulled upwards at its ends. However, upon reaching the liquid surface (1), it tends to follow the meniscus and is guided to the wall (2). Still pulled up, the fibre pulls a small amount of liquid up, and the surface tension still presses it to the wall (3). At the top edge, the fibre finally rips off the wall and gets out of the bath (4).

The second problem that I faced was due to the surface tension of liquids. When a sample is lifted from the bath with a liquid, it tends to follow the liquid surface and gets attracted to the bath wall (Fig. 4.11). During further lifting, it slips along the wall and actually pulls the liquid upwards. Eventually, it has to be ripped from the wall edge. One should be very careful and control the stages in such a manner that the fibre is not stressed too much. While learning it, several samples were destroyed.

#### 4.5.2 Test liquids

For my experiments, I first tried to use spectroscopy-grade organic solvents (acetone, ethanol, methanol, heptane) and water. Organic solvents proved to be a suboptimal choice. Firstly, they quickly evaporated. I had to always check if the sample was still in the liquid or just touching its surface. Secondly, due to this evaporation, the whole setup was being cooled down and the refractive index of both the fibre and the liquid was changing significantly. (A cooling of about 2 K was measured, corresponding to the ZDW shift of about 2 nm.) Thirdly, what was somewhat a surprise to me, the dispersion of solvents was not so well defined, despite their wide use.

Water has a very strong surface tension and was therefore hard to work with: Samples were sticking to the water surface so strongly that several of them were destroyed before I could do a single measurement. I therefore stopped working with water.

For the actual measurements, I used the Cargille refractive index liquids [97]. Each of them is a composition of perfluorocarbon and chlorofluorocarbon, and is non-volatile, inert, with a very small surface tension (18 dynes/cm at 25 °C, compare to ~ 23 for organic solvents and 58 for water). They are normally used as the calibration liquids for refractometers, therefore their dispersion is well-defined (to 4 digits) in the range of 365 to 10648 nm. Cargille offers them with various nominal refractive indices. I used set AAA-1/2, which contained 10 liquids with refractive indices from 1.30 to 1.39. (For comparison, the refractive index of water and ethanol at 830 nm is 1.33 and 1.36, respectively.) The dispersion data provided by Cargille (the Cauchy's equation coefficients) was entered into the Optical Fibre Toolbox, so that it was possible to accurately calculate the refractive index of both the fibre and the surrounding liquid at any wavelength and at any temperature.

#### 4.5.3 Temperature variation

The setup was not temperature-stabilized. The ambient temperature and the temperature of the liquid in the bath were monitored with the precision of 0.1 K using a 4-channel Voltcraft K204 temperature logger. (Note that a 0.1 K temperature change leads to approximately 0.1 nm in the ZDW.) The liquids were kept near the setup, to speed-up the temperature stabilisation once the liquid is in the bath. Before each measurement, after filling the bath with a liquid, I was waiting until the temperature in the bath stabilized to the ambient value.

#### 4.5.4 Sample design

For this experiment, I used the same sample design as described in chapter 3 for the in-air interferometers, the only difference being the waist diameter. Recall that for in-air samples, the waist diameter was chosen to guide the HE<sub>11</sub> and HE<sub>12</sub> modes reliably and to cut off the HE<sub>13</sub> mode (Sec. 3.1.4). In liquids, the situation is slightly more complex. Because each liquid has a different refractive index, the cut-off diameters of the HE<sub>12</sub> and HE<sub>13</sub> modes are also different in each liquid (Fig. 4.12). For example, at 850 nm (solid curves), the HE<sub>12</sub> mode will be guided in all the liquids, provided that the waist diameter is greater than 2.4 μm; the HE<sub>13</sub> mode will be cut off at 2.9 μm or larger diameter. Thus the design waist diameter for these liquids at 850 nm is between 2.4 and 2.9 nm. At 1000 nm (dashed curves), the values are shifted towards larger diameters. As the result, the HE<sub>12</sub> mode cut-off at 1000 nm occurs in the  $n = 1.39$  liquid at about the same diameter as the HE<sub>13</sub> mode cut-off at 850 nm in the  $n = 1.30$  liquid, making it impossible to find an optimal diameter for all liquids simultaneously

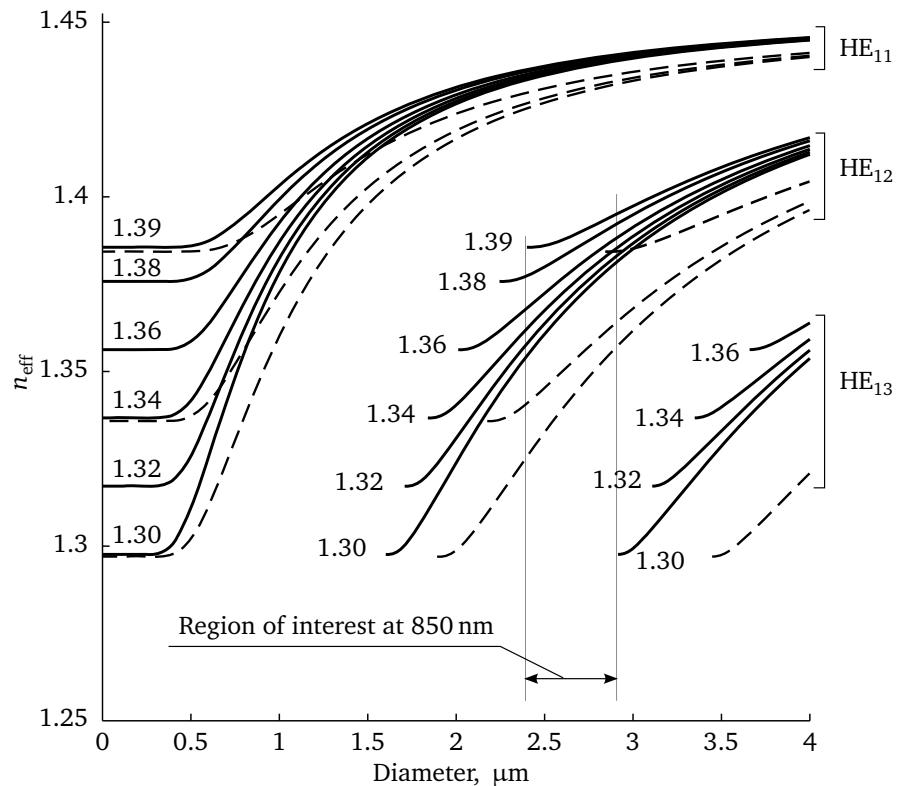


**Figure 4.12:** First three  $HE_{1m}$  modes of SM800 fibre in different Cargille liquids (nominal refractive index  $n_d$  is shown next to each curve). Solid lines: 850 nm. Dashed lines: 1000 nm. The cutoff of mode  $HE_{12}$  in the 1.39 liquid at 850 nm is at  $d = 2.4 \mu\text{m}$ . The cutoff of mode  $HE_{13}$  in the 1.30 liquid at 850 nm is at  $d = 2.9 \mu\text{m}$ .

at 850 and 1000 nm. Since I wanted to perform the stretch-test and the pulling machine was equipped with a 852 nm laser, I decided to go for 850 nm as the design wavelength, and chose the design waist diameter of  $d = 2.6 \mu\text{m}$ . The closest value the pulling machine software could do was  $2.55 \mu\text{m}$ . This was the design diameter I used for my in-liquid samples.

With the samples designed for in-liquid experiments, the post-production stretch-testing is more sensitive to manufacturing errors than for in-air samples. In the pulling machine, the sample is surrounded by air and therefore the waist

**Table 4.5:** In-liquid samples target (design) shape.

Waist diameter	$2.55 \mu\text{m}$
Waist length	3 mm
Programmed taper angle	16 mrad
Flame width	0.7 mm

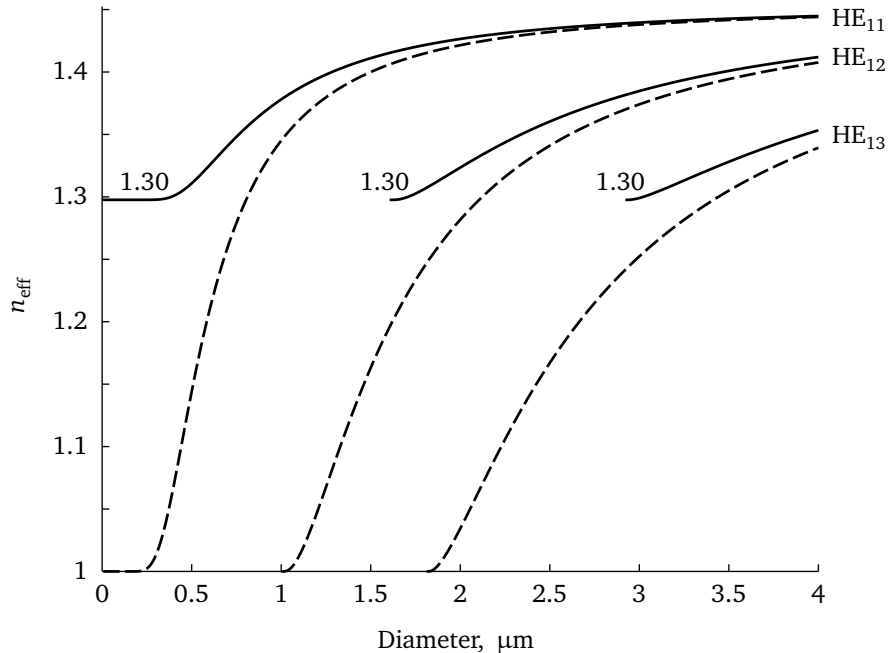


**Figure 4.13:** HE<sub>11</sub>, HE<sub>12</sub>, and HE<sub>13</sub> modes in Cargille 1.30 (solid curves) and in air (dashed curves). For the waist diameter of  $d = 2.55 \mu\text{m}$ , the HE<sub>13</sub> mode is cut-off in liquid but is still guided in air. (Calculated for  $\lambda = 852 \text{ nm}$ .)

can guide the HE<sub>13</sub> mode, which should be cut off in liquids (see Fig. 4.13). Therefore, if the mode coupling is not completely confined to HE<sub>11</sub>↔HE<sub>12</sub>, the HE<sub>13</sub> mode will show up in the test.

#### 4.5.5 Results and analysis

In total, 16 samples were produced for in-liquid measurements. Actual measurements in several liquids followed by a scattering-based diameter measurement was performed with samples 204 and 218. However, sample 218 was destroyed before being measured in all available liquids. The results obtained with this sample are similar to those with sample 204 and do not provide additional information. Therefore I do not show them here.

**Sample diameter** Figure 4.14 shows the stretch-interference signal measured with sample 204. The signal is almost perfectly harmonic, indicating that in this sample mode coupling in tapers works indeed as designed (no coupling to HE<sub>13</sub> mode). However the period of this signal corresponds to the waist diameter of 1.98  $\mu\text{m}$ , which is more than 0.5  $\mu\text{m}$  less than the design diameter of 2.55  $\mu\text{m}$ . Note that at 1.98  $\mu\text{m}$  the HE<sub>13</sub> mode is still not cut-off in air (Fig. 4.13), so the decreased diameter alone cannot explain the clean stretch-signal.

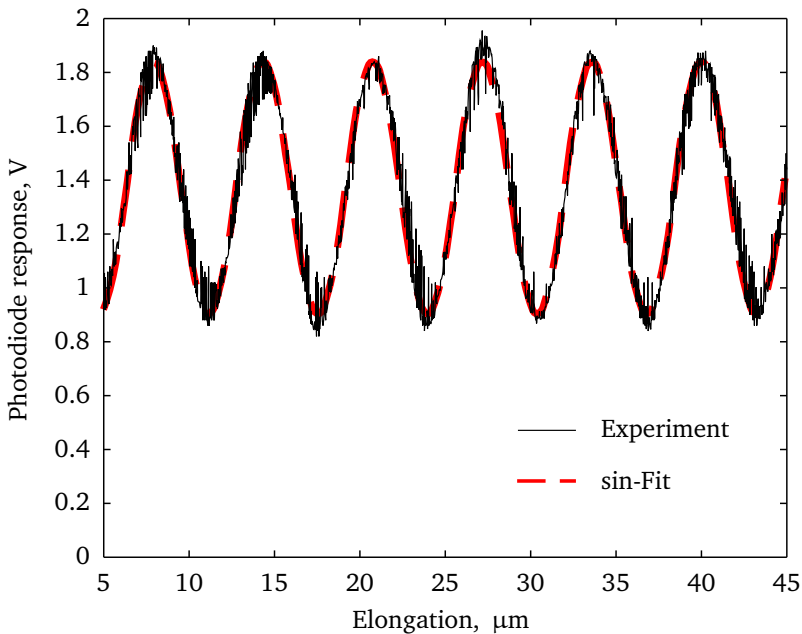


**Figure 4.14:** Stretch-interference signal of sample 204. Note that, apart from mode hops of the non-temperature stabilized laser diode, the signal is almost perfectly harmonic.

To make sure the stretch-signal, indicating a very wrong diameter, was not due to some taper shape problem, I measured this sample with the scattering and the ZDW methods. In the scattering measurement, the result was  $2.03(1)\text{ }\mu\text{m}$ . The reference ZDW measurement was performed in the Cargille 1.32 liquid and the diameter of  $2.02\text{ }\mu\text{m}$  was derived. Therefore I conclude that the sample indeed has a diameter of about  $2\text{ }\mu\text{m}$ , significantly below the design value. I do not have enough data to explain this deviation. However, I know from other people working with this pulling machine that they occasionally observed the diameter deviation as high as 100 % of the design value. Note that sample 167 (page 72) also indicated a possible significant increase of the waist diameter. It might be due to some occasional error in the control software. The diameter values for sample 204 are listed in Tab. 4.6.

**Table 4.6:** Comparison of design and measured diameter for sample 204.

	Diameter, $\mu\text{m}$
Design	2.55
ZDW-derived	$2.02(0)$
Stretch-derived	$1.98(0)$
Scattering-measured	$2.03(1)$

**Results** Measurement with sample 204 was performed in all available Cargille liquids. The detailed results are given in appendix E. In most cases, the simulated  $c_1$  parameter is about 5 ... 8% off the measured value (for two measurements, in liquids 1.38 and 1.39, the simulation result is within the error-bar of the measurement), so again, as with the in-air measurements, additional information about the sample should be obtained by a full shape measurement.

The ZDW values are shown in Fig. 4.15(a), while the difference between the experimental and the simulated results can be seen in Fig. 4.15(b). Just for two measurements—in liquids 1.32 and 1.39—the expected value is within the error-bar of the measured one. The value in the 1.32 liquid was used to determine the diameter using the ZDW method; therefore it is not surprising that here the simulation and the experiment match each other (the small residual error comes from the fact that I used only three digits for the diameter: 2.02  $\mu\text{m}$ ). For other liquids, the discrepancy ranges between  $-2.8$  and  $1.5$  nm, and I do not have any convincing explanation for it. I do not think that the sample shape uncertainty could be responsible for such fluctuations, because they do not look systematic. One possible reason could be mistakes in the temperature measurement, although I do not see now what they could be. The error of 2.8 nm should correspond to a temperature error of almost 3 K, which I find improbable. The measurements were performed before the full OMF software model was created, therefore I could not notice this rather small discrepancy while still working in the lab. With the new pulling machine and the sample measurement method these questions can, hopefully, be answered.

The experimental value for sensitivity of sample 204 to the external refractive index ranges between 2900 and 4100 nm per refractive index unit. It is one of the highest values observed for similar fibre-based sensors. For comparison, sensitivities of up to 2000 nm/RIU were reported in [51, 98–100]. In [23], the sensitivity is as high as 19 000 nm/RIU; however the sensor is based on a birefringent OMF, which requires polishing and makes manufacturing much more complicated.

## 4.6 Conclusions

The performed spectral interference measurements have mostly confirmed the validity of the model developed in chapter 2 and one of its main conclusions—the high sensitivity of a SOMMI-based sensor to external refractive index. The developed spectrum acquisition and analysis procedure proved to work well even with noisy spectra. The error values however are not very uniform, so the procedure should still be refined.

The main difficulty during my experiments was the uncertainty in the sample shape. At the same time, the obtained results to a large extent confirm the applicability of the scattering-based method, though it should still be properly implemented to measure the full shape of a sample.

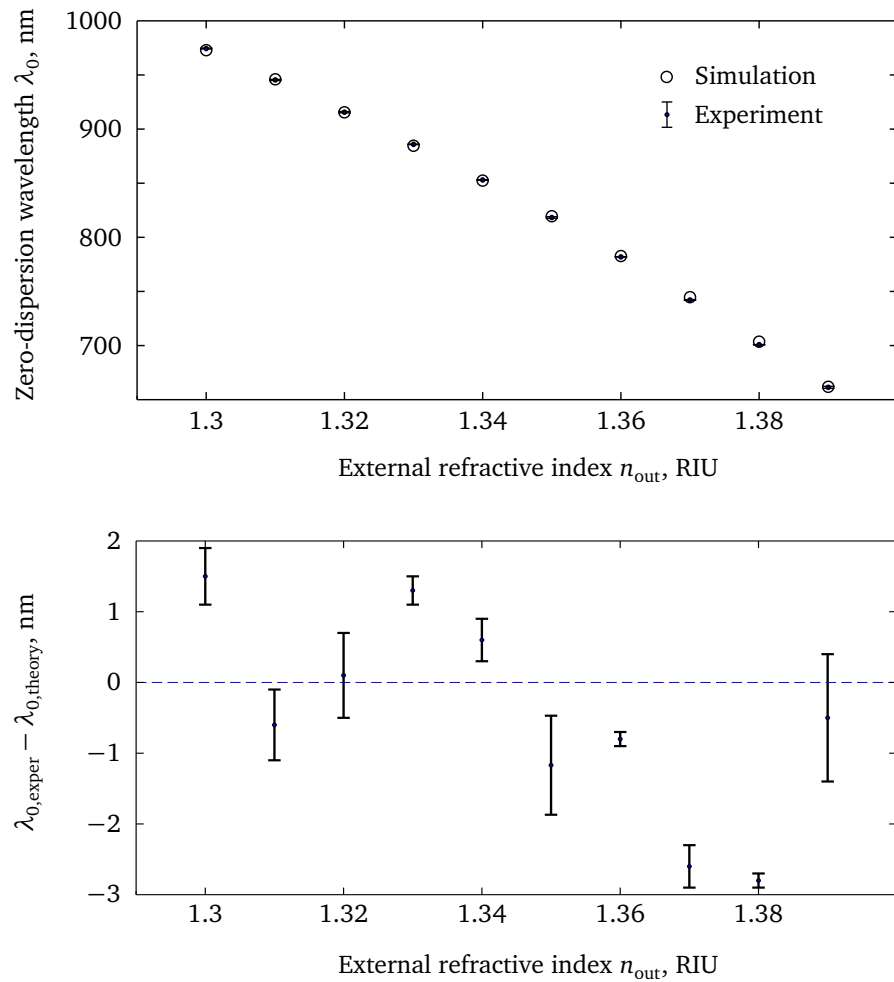


**Figure 4.15:** Zero-dispersion wavelength for sample 204 in Cargille liquids. (a) ZDW. The error bars are almost invisible. (b) Difference between the measurement and the simulation.

# 5

## CHAPTER

# Summary and outlook

The results presented in this thesis provide the basis for optical microfibre (OMF)-based interferometry. For the first time, experimental and theoretical investigations of single OMF modal interferometers (SOMMIs) were performed at such level of detail. Many practical techniques had to be developed to reliably transport and handle the fragile OMF samples, clean them, put them into an electron microscope, a vacuum chamber, and bathes with liquids, and to perform reproducible measurements in these different setups. The high sensitivity of SOMMIs to variation of ambient conditions made it important to take such variations into account, both in experiment and in theoretical model. An almost real-time spectral measurement technique was implemented, and an appropriate data extraction algorithm was developed for automated processing of hundreds of spectra taken within each measurement. This algorithm proved to be surprisingly stable ( $< 1 \text{ nm}$ ) even for very noisy measured spectra. At the same time, it provided excellent data extraction precision (down to  $0.03 \text{ nm}$  with a spectrometer resolution of  $1.5 \text{ nm}$ ) for high-quality spectra. Various approaches were employed to maximize the signal-to-noise ratio in all measurements.

Detailed understanding of mode propagation and phase-matching in OMFs allowed to create a novel optical harmonic generation-based method for OMF waist-diameter measurement [1]. It is non-destructive, quite fast, and allows determination of the sub-micrometre OMF waist diameter with the absolute precision of 0.5 %—the best value for OMFs to date. To verify this method, scanning electron microscopy measurements were performed. Again, to achieve high precision and obtain detailed information about the diameter variation along the OMF, numerous images had to be taken in automated mode. A special image analysis algorithm was developed to extract information about the sample shape from them [74].

The harmonic method was used to characterize the pulling machine, with which our samples were produced. However, the SOMMI samples themselves

could not be measured with this method due to a very different diameter range. Therefore, two other methods were developed to verify the produced SOMMI samples: a stretch-interference test and a zero-dispersion wavelength method. Being fast and non-destructive, these could be performed for each produced sample.

To theoretically analyse light guidance in OMFs and obtain physically meaningful information from measured data, a special software tool—Optical fibre toolbox for Matlab (OFT)—was created [2]. To the best of my knowledge, this is the only software code with such functionality today. While the existing software usually specializes on either thick telecom fibres or microoptical devices and therefore cannot accommodate the large diameter variation in OMFs, OFT combines different models for calculation of mode propagation through the whole tapered OMF. Its characteristic feature is the automatic search for guided modes and their tracing for varying wavelength and diameter. Due to this feature, the harmonic generation effect in OMFs could be turned into a practical measurement method. It also allowed me to model in detail the behaviour of SOMMIs in various liquids in detail, with full consideration of the sample shape, the material dispersion of glass and liquids, and temperature effects. In the stretch interference simulation, I successfully calculated the SOMMI response, taking into account the Poisson, the photoelastic and the induced birefringence effects.

For possible practical applications it is of interest that SOMMIs exhibit the highest sensitivity among similar fibre-based sensors so far—about 3000 to 4000 nm per refractive index unit in the present measurements, which is only exceeded by devices based on rectangular fibres.

Several directions for further work can be suggested.

## 5.1 Pulling machine

During this project, experimental samples were produced using the pulling machine in the group of Arno Rauschenbeutel (Mainz/Vienna). For practical reasons, it would be beneficial to have easy access to an OMF pulling machine, because destruction of samples and the inability to experiment with the sample shape were some of the main technical problems during this work. Therefore, a new pulling machine is currently being built in our group.

The stretch-experiment has revealed significant shape variation from sample to sample with the current pulling machine. It is important to analyse and eliminate this effect. We mainly suspect problems with the fibre fixation in the machine. I have therefore designed a new clamping mechanism, which has been built and is now awaiting first tests.

In addition, it is necessary to improve the pulling control software, so that the target shape of the fibre is determined more precisely (for example, by not using the rectangular flame approximation). The control software should also be improved in terms of interaction with the user, to notify her of any implicit

changes applied to the design shape of the sample as well as of any problems possibly occurring during pulling.

## 5.2 Sample shape

The developed simulation software was already used to design OMF samples for harmonic generation at various wavelengths and SOMMI samples for interferometry in air and in liquids. Future possible applications might include the design of samples with maximized sensitivity to and increased working range of the external refractive index and minimization of the taper length for more compact samples.

The most important next step, however, would be an implementation of a robust and reliable sample shape measurement procedure. This can be based on the scattering-measurement technique that was used in this work. The technique was shown before to be applicable to the OMF measurement and provide an error within  $0.05 \mu\text{m}$  [88]. The method can be further improved, as shown in this work, by using more than just one wavelength for the same sample. I have already used two lasers, at 633 and 532 nm; between them, the error for some samples was within  $0.02 \mu\text{m}$ . At different wavelengths, the scattering patterns are significantly different, which minimizes statistical and systematic errors. Therefore, it seems beneficial to extend the wavelength range to near-infrared and blue.

To obtain the sample shape and not just the waist diameter (as done in this work), it is necessary to implement a setup with automatic scanning along the sample and simultaneous image analysis. Scanning can be easily realized if the measurement is done in the same pulling machine where the sample is produced. Similarly to the stretch-test described in this work, such measurement could then be performed for each sample right after pulling, and provide the detailed information about its shape.

Verification could be performed using the same SEM-based technique as we used to verify the harmonic generation-based results [1, 74]. Another approach would be to measure the waist diameter using the harmonic method and then determine the relative variation of the diameter using the whispering gallery modes method [101].

The ongoing development of the theoretical model during this project was lagging behind the experiment, and the full stretch- and spectral-interference models, capable of taking into account the real sample shape, were realized only in the recent months, after the completion of the experimental work. As a result, the samples were measured with lower precision than simulation is now allowing. This explains the noticeable difference between the experimental and simulation results for spectral and stretch interferometry. Once the full shape measurement procedure is implemented, verification of the models developed in this work should be repeated.

### 5.3 Dispersion measurement of atoms and molecules

It would be interesting to apply the SOMMI to the dispersive detection of an atomic gas (for example, caesium) around the sample. A similar interferometric measurement without fibres is known as the hook method [102]. Within the scope of this work, it was not possible to perform such measurements, due to the problems with OMF samples in the vacuum chamber with caesium vapour [91, 93]. However, these problems were rather technical than physical, some other groups having succeeded in putting OMF samples into dense alkali vapour [103].

It would also be of interest to combine a SOMMI with photochromic molecules, where the molecule absorption (and hence the dispersion) can be controlled with light. Switching of molecules on an OMF surface was successfully demonstrated in our group [92]. However, a quick attempt to measure interference response did not show any result (i.e. molecule switching was not detected interferometrically). This could be due to a sub-optimal combination of the SOMMI sample and the molecules, the latter being absorbing in the ultraviolet and visible range, and the SOMMI having been designed for the infrared.

For the improvement and analysis of such measurements, it is also important to be able to simulate dispersion and absorption with atoms and molecules around the OMF. Theoretically, it is straightforward to do using a complex material refractive index of such surrounding materials [104]:

$$n(\omega) = \sqrt{1 + 4\pi\chi^{(1)}(\omega)},$$

where  $\omega = 2\pi\nu = 2\pi c/\lambda$  is the angular frequency of light wave and  $\chi^{(1)}$  the complex linear susceptibility. With the present implementation of the software, one cannot perform such calculations due to a fundamental reason: The algorithm is based on a very efficient routine to find the roots of the eigenvalue equations. However, this routine is unable to work with complex numbers. For this particular task, another algorithm could be implemented in the future.

### 5.4 Simulation

A calculation still missing in OFT is the full mode coupling analysis. Replacing the critical angle theory, it would allow more precise design of SOMMI samples, e.g. for maximized interference contrast. For non-interferometric OMFs, it could be used to design complex tapers for shorter samples.

The exciting aspect of science is that it never comes to an end.

# APPENDIX A

## Guided mode solutions

In this appendix I provide references for the equations needed to calculate the guided modes (propagation constant and field distribution) in an OMF. These equations are quite complex and hence

- it is almost impossible to avoid typos in their reproduction (proven by numerous typos in published papers);
- they provide little insight in physics of modes.

Therefore, instead of retyping them from the original papers and textbooks, I reference the sources themselves, indicating where necessary the found typos. Many of these equations have also been implemented in Matlab code in our Optical fibre toolbox (OFT) [2]. If you want to implement them in the code yourself, I recommend to copy them directly from OFT or to use the functions of OFT as a reference to verify your own code. In appropriate places I reference the corresponding OFT functions. In the end, a table with all models per OMF region is provided (Tab. A.1).

### A.1 Two-layer waveguide

#### A.1.1 Scalar approximation (LP modes)

Can be used for input and output pigtails of OMFs or for usual telecom fibres.

##### A.1.1.1 Eigenvalue equation

This EVE is referenced in many sources. I have taken it from [31], Eq. (3.3-26). In OFT it is implemented in file `eve2LS.m`.

### A.1.1.2 Field equations

The field equations can be also taken from [31]: Eq. (3.3-24) and (3.3-25). OFT file: modeFieldLP.m.

### A.1.2 Vector solution

Can be used instead of two-layer LP modes and for OMF waist far from the core-cladding guidance transition point ( $n_{\text{eff}} \ll n_{\text{clad}}$ ).

#### A.1.2.1 Eigenvalue equation

EVE is taken from [31], Eqs. (B-11), (B-17a), and (B17b) for HE/EH, TE and TM modes respectively. Note a typo in Eq. (B-11): argument of function  $K$  and its derivative  $K'$  should be  $(qa)$  instead of  $(ha)$ . OFT file: eve2LS.m.

#### A.1.2.2 Field equations

Field equations are given in [30, p. 250]. OFT file: modeField.m.

## A.2 Three-layer fibre

These models are required for simulation of modes in OMF tapers.

### A.2.1 Scalar approximation (LP modes)

Three-layer LP modes is a valid approximation for large diameters, where the cladding-surrounding boundary does not play a significant role.

#### A.2.1.1 Eigenvalue equation

This is nicely and without typos given in [38]. The eigenvalue equations are Eq. (3) for cladding-guided modes ( $n_{\text{out}} \ll n_{\text{eff}} \leq n_{\text{clad}}$ ) and Eq. (4) for core-guided modes ( $n_{\text{clad}} \leq n_{\text{eff}} < n_{\text{core}}$ ). OFT file: eve3LS.m.

#### A.2.1.2 Field equations

Field equations can be found in [25], Eqs. (29)–(31), and in [38], Eqs. (1)–(2). The field coefficients are defined in Appendix I in [38].

### A.2.2 Vector solution

This is the most correct description of OMF modes, however it is also the slowest to calculate. Therefore it can be recommended to use simpler models where possible, see Tab. A.1 on page 106.

### A.2.2.1 Eigenvalue equation

For HE/EH modes, EVE is Eqs. (5)–(7) in [41]. Note that only the cladding-guidance solution was derived by Erdogan and used in this thesis. There are some typos in Eq. (7), corrected in [42]. For TE and TM modes, EVEs are Eqs. (7) and (8) from [39]. OFT file: `eve3LS.m`.

### A.2.2.2 Field equations

For HE/EH modes, all equations are given in [41], with some corrections provided (under the same numbers) in [42]. Electric and magnetic fields are defined:

- in the core: by Eqs. (20)–(25);
- in the cladding: Eqs. (A1)–(A6);
- in the surrounding: Eqs. (A9)–(A14).

Equations (23), (A3), (A12), and (A13) contain typos in [41] and should be taken from [42]. Still, an imaginary unity  $i$  is missing in Eq. (A13) in [42] after  $G_3$ . It can be verified by numerically checking the boundary conditions for magnetic field and by analogy with Eq. (A12).

OFT file: `modeFieldErogan.m`.

Within the scope of this work I did not need and therefore have not checked any field equations for three-layer TE and TM modes. All three-layer equations (also the EVE) are given in [43]. However the first attempt to implement them resulted in the same problem as the Tsao HE/EH solution—no roots could be found numerically. Therefore I cannot comment on the correctness of this paper.

## A.3 Anisotropic fibre

Solution in anisotropic fibres is needed for stretch-simulation. For two-layer modes, it is derived in [57], with EVE being Eq. (35). OFT file: `tonning.m` with photoelastic effect calculated in `photoelastic.m`.

For a three-layer system with axial stretch, the solution is given in [43]. See the last remark in the previous section.

## A.4 Model applicability

Table A.1 reviews the model applicability by OMF region.

**Table A.1:** Model applicability by region in an OMF

Region	Hybrid				TE				TM			
	2L LP	2L HE/EH	Monerie	Erdogan	2L LP	2L TE	Tsao TE	Monerie	2L LP	2L TM	Tsao TM	Monerie
$d \ll d_{\text{tr}}$	—	✓	—	✓	✓	✓	✓	✓	—	✓	✓	—
$d \approx d_{\text{tr}},$ $n_{\text{eff}} \leq n_{\text{clad}}$	—	—	✓	✓	—	—	✓	✓	—	—	✓	✓
$d \approx d_{\text{tr}},$ $n_{\text{eff}} \geq n_{\text{clad}}$	—	—	✓	—	—	—	✓	✓	—	—	✓	✓
$d = 125 \mu\text{m}$	✓	✓	✓	—	✓	✓	✓	✓	✓	✓	✓	✓

Here “2L” denotes two-layer models,  $d_{\text{tr}}$  is the transition diameter where  $n_{\text{eff}} = n_{\text{clad}}$  and the cladding guidance changes into the core guidance (or vice versa).

How to use this table: (1) Determine your region of interest in terms of diameter and  $n_{\text{eff}}$ . (2) Determine which modes you are interested in. For example, the SOMMI modes are  $\text{HE}_{11}$  and  $\text{HE}_{12}$  (hybrid). (3) Find the applicable model, taking into account that the 2-layer calculation is in general faster than the 3-layer one, and the scalar models (LP and Monerie) are faster than the vector ones.

# B

## APPENDIX

# Algorithm description

## B.1 Search for guided modes

The algorithm I have developed first finds the guided modes of a particular type (hybrid, TE or TM) in the region of interest (ROI). ROI is the range of diameters or wavelengths (depending on the task), for which the dispersion curves are to be calculated. For example, let's consider the dispersion plot  $n_{\text{eff}}(d)$ .

To find the guided modes, the program calculates the value of the left part of Eq. (2.3) (for the hybrid modes; equations (2.4) and (2.5) are used for TE and TM modes) for each  $n_{\text{eff}}$  along the diagonal line shown in Fig. B.1. (The effective refractive index  $n_{\text{eff}}$  equals  $\beta\lambda/2\pi$ , see Eq. (2.2), and can therefore be found from the EVEs for  $\beta$ .) The number of points taken along this line is  $N_p = 10\,000$ . This particular line is chosen because *all* dispersion curves guided in the ROI intersect it and because, due to the shape of the curves, the distance between them along this line is larger than if we'd take, for example, a vertical line  $d = \text{const}$ .

If we write the EVE as  $F(d) = 0$ , the points  $d$  where  $F = 0$  will belong to the modal curves. To find these values numerically, we find among all  $N_p$  calculated points those points  $F_j(d_j)$ , where the function changes its sign:

$$\text{sgn}(F_j) \neq \text{sgn}(F_{j+1})$$

and then apply the standard `fzero` function in Matlab [105] in the range  $[d_j, d_{j+1}]$  to find the exact (within the numerical tolerance) position of the roots.

Having found all roots, we compare their number to  $N_p$ . If the number of roots found is larger than  $N_p/100$ , the program increases  $N_p$  and repeats the whole procedure. This is done in order to prevent missing any modes when the curves get very close to each other.

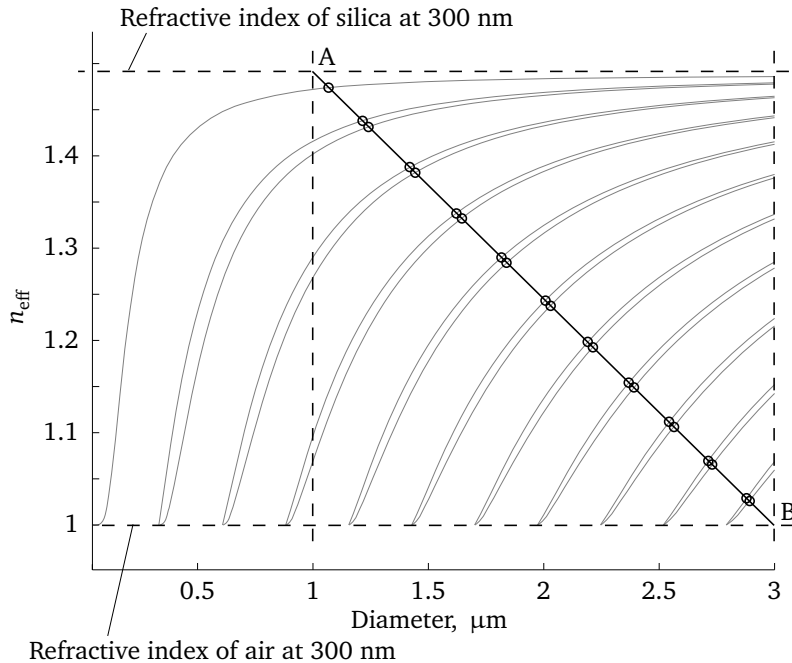


**Figure B.1:** Region-of-interest ( $d = 1 \dots 3 \mu\text{m}$ ,  $n_{\text{eff}} = n_{\text{air}} \dots n_{\text{silica}}$ ) and the diagonal line AB. Circles mark the roots of the eigenvalue equation (2.3) along line AB. Grey lines indicate the actual modal curves, which can be traced starting from the discovered roots.

## B.2 Tracing the dispersion curve

After one point from each dispersion curve has been found, the curve is numerically traced by the program, i. e. each new point is found near the previous one. Each of the requested modes (e. g.  $\text{HE}_{11}$ ,  $\text{TM}_{02}$ ) is traced independently.

The algorithm I have implemented is trying to perform this tracing as quickly as possible at the same time trying to avoid the “mode jumps”. A mode jump is a mistake the algorithm can make by finding a point belonging to another dispersion curve. For example, a user asked the program to trace the dispersion curve  $n_{\text{eff}}(d)$  for mode  $\text{HE}_{11}$ . Each point of this curve is a solution of the eigenvalue equation (2.3). However a point belonging to mode  $\text{HE}_{12}$  is also a valid solution of this equation. Therefore the program cannot distinguish between the points belonging to modes  $\text{HE}_{11}$  and  $\text{HE}_{12}$ . The algorithm is designed in such a way as to minimize the probability of such mistakes. If they still occur, they are easy to detect: mode jumps break the smoothness of the dispersion curves. If a mode jump has been detected, the program re-traces the curve going in smaller steps.

# C APPENDIX

## OMF samples

The design parameters of all samples, mentioned in this thesis, are listed here. We use sequential numbering for our samples, therefore the SOMMI samples are mixed with the samples for other experiments. The SOMMI project was started 2.5 years after the beginning of our work and the first SOMMI sample had number 108.

**Table C.1:** Design parameters of OMF samples.

Sample number	Waist $\phi$ , $\mu\text{m}$	Waist length, mm	Trajectory, slope, mrad	Trajectory, diameters, $\mu\text{m}$	Flame width, mm	Designed for	Results, pages
24	0.478	5	3-2-3	125-80-20	1	HG	62
28	0.376	5	3-2-3	125-80-20	1	HG	62
31	0.376	5	3-2-3	125-80-20	1	HG	62
48	0.777	5	3-2-3	125-80-20	1	HG @ 1550 nm	64
52	0.376	5	3-2-3	125-80-20	1	HG	62
55	0.404	5	3-2-0.01	125-80-20	1	HG	62
56	0.393	5	3-2-3	125-80-20	1	HG	62
59	0.419	5	3-2-3	125-80-20	1	HG	62
67	0.460	3	3-2-3	125-80-20	1	HG	62
71	0.500	5	3-2-3	125-80-20	1	HG	62
108	1.302	5	3-6-3	125-80-20	1	In-air	109
165	1.302	3	3-16-3	125-80-20	1	In-air	89
166	1.302	2	3-16-3	125-80-20	1	In-air	72
167	1.302	2	3-16-3	125-80-20	1	In-air	72
168	1.302	2	3-16-3	125-80-20	1	In-air	67, 72, 84–88
204	2.552	3	16-16-16	125-80-20	0.7	In-liquids	96–98
218	2.445	3	16-16-16	125-80-20	0.7	In-liquids	95

Here HG stands for harmonic generation, in-air and in-liquids relate to SOMMI experiments.



# D

## APPENDIX

# Fibre holder

## D.1 Fixing a sample in the holder

After the sample has been produced in the pulling machine, while it is still clamped to the translation stages, the frame (with the bottom lid mounted) is inserted under it (Fig. D.1) using a 4D tilt-translate stage (Fig. D.2). To put the frame just beneath the sample, we illuminate the fibre from above with a usual torch lamp and observe the fibre and its shadow of the untapered fibre on the holder surface. When the frame surface approaches the fibre, the fibre approaches its shadow. The fibre is either glued to the frame using a UV cured glue or clamped using two small clamps (not shown, screwed to the frame at the glueing point in Fig. 3.17). The clamping option was designed for the case that outgassing of the glue posed any problems in the vacuum chamber; we have never used it so far.

Once the sample is fixed to the frame, it is unclamped from the translation stages. The frame is then removed from the pulling machine (but still kept under the flow box of the pulling machine). The cover (with the top lid mounted) is then screwed to the frame and the coated ends of the sample clamped at the ends of the cover. Finally, the side lid is mounted. At this moment, the sample is closed from all sides and mechanically fixed. It can be removed from under the flowbox and packed for transportation or stored.

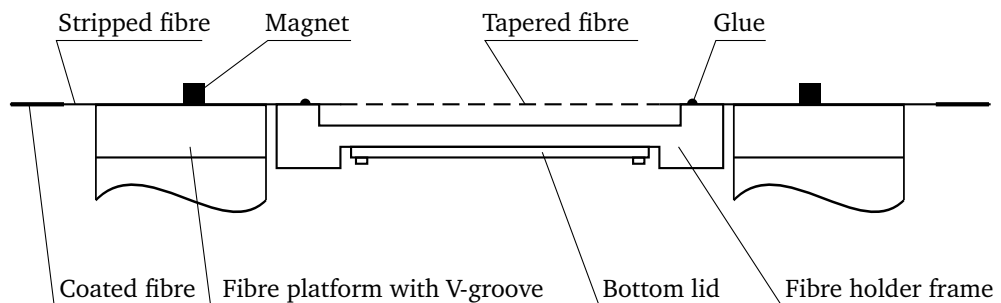


**Figure D.1:** Fixing OMF after pulling. Fibre holder frame is positioned under the fibre between the fibre-clamping platforms on top of the translation stages of the pulling machine (cf. Fig. 3.1 on p. 53). The fibre is glued to it at the stripped but untapered parts with a UV cured glue. Afterwards, the magnets holding the sample in the pulling machine are removed and the holder frame with the fibre is removed too and closed from all sides to protect the sample.

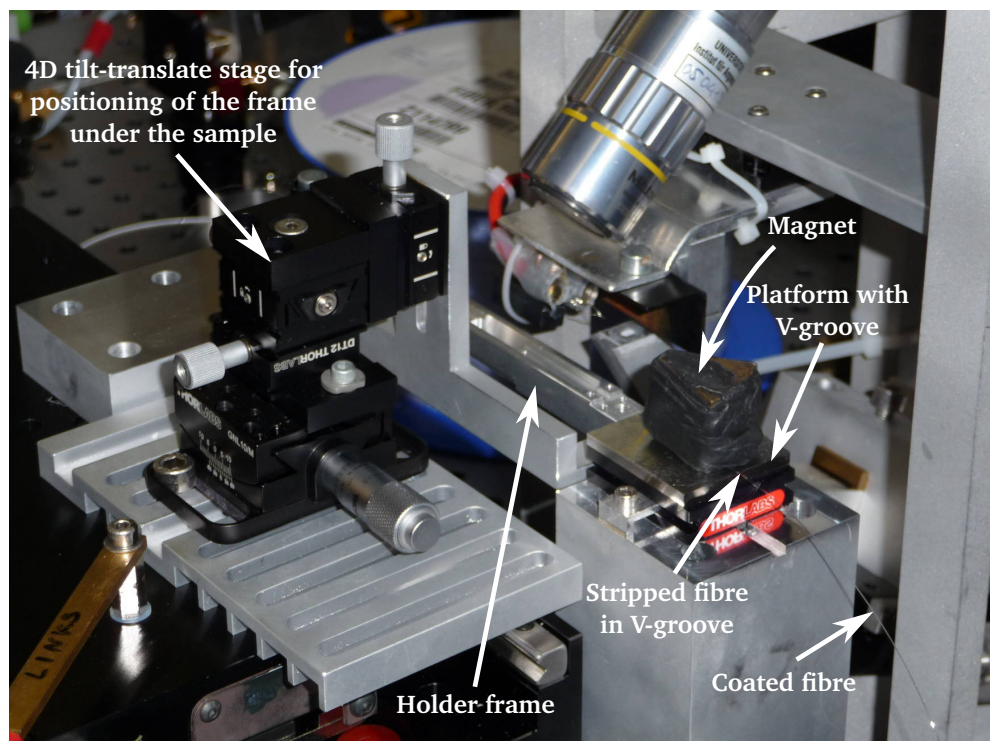


**Figure D.2:** Positioning of the holder frame (version 2 is shown here) under the tapered fibre in the pulling machine using a 4D tilt-translate stage.

## D.2 Transportation and storage

As already mentioned, the pulling machine we were using was located first in Mainz and later in Vienna. We thus had to bring the samples to Bonn, by train or by plane. Two samples were also once taken to England, to perform some experiments in the group of G. Brambilla, University of Southampton.

We have developed a simple routine which has worked fine over four years of our project. After the sample has been fixed in the holder, the fibre pigtails (about 1 m long) are rolled and fixed to the cover using an antistatic (ESD) adhesive tape. The holder is then put into a plastic ESD (pink) zipper bag.\* Ideally, this should be done under the flowbox of the pulling machine. We normally put two samples in each bag.

So packed, the samples can be stored in a usual room for months and reused many times.

For transportation, all sample bags are stacked on top of each other in a notebook computer bag (which offers mechanical protection), with a bubble film under and above this stack. Finally, this sandwich is fixed in the notebook bag with a strap. The remaining space in the bag can be used for a notebook or any other stuff.

It is worth mentioning that the airport security is normally interested in the contents of this bag: on an X-ray screen, the stack of holders with fibres looks like several metal boxes with a clutter of wires around them. For this very reason, we have never tried to check it in. The security officer should be informed that these are fragile research samples so that she doesn't open the bag herself or at least does it very carefully; the bag can then be opened, the bubble film unwrapped and the top samples shown to the officer without being removed from the ESD bag. We have transported samples by plane three times, and everything went smoothly. We have not tried to fly with these holders to or from Israel so far.

Out of more than 200 samples produced and brought to Bonn over four years of use of these holders, not a single one was broken or damaged during transportation or storage.

---

\*We are using ESD-compatible packaging for better protection of the samples against dust. We have not done any tests as to whether it actually has any benefit or not. However we know that OMFs are extremely sensitive to dust: Left open outside a flowbox, they loose transmission over 2–3 days. Under a chemistry fume hood (which sucks outside air into the hood), the transmission is lost within approximately half an hour.



# E

## APPENDIX

### Sample 204 in Cargille liquids

The following table lists the fit parameters for measured and simulated spectra corresponding to Sec. 4.5.5.

Liquid	$\lambda_0$ , nm	$c_1$	$c_2$	$c_3$	$t$ , °C
1.30	974.4(4)	0.0229(2)	$1.07(7) \times 10^{-4}$	$0.5(1) \times 10^{-6}$	22.4
Simulation	972.9	0.0249	$1.08 \times 10^{-4}$	$0.26 \times 10^{-6}$	
1.31	945.4(5)	0.0233(2)	$-0.1(5) \times 10^{-4}$	$-3(1.4) \times 10^{-6}$	22.5
Simulation	946.0	0.0251	$1.22 \times 10^{-4}$	$0.61 \times 10^{-6}$	
1.32	915.6(6)	0.0239(2)	$1.34(4) \times 10^{-4}$	$0.90(16) \times 10^{-6}$	22.5
Simulation	915.5	0.0259	$1.32 \times 10^{-4}$	$0.69 \times 10^{-6}$	
1.33	885.9(2)	0.0254(1)	$1.24(1) \times 10^{-4}$	$0.47(1) \times 10^{-6}$	22.5
Simulation	884.6	0.0268	$1.37 \times 10^{-4}$	$0.55 \times 10^{-6}$	
1.34	853.0(3)	0.02649(2)	$1.308(6) \times 10^{-4}$	$0.460(7) \times 10^{-6}$	22.5
Simulation	852.4	0.02764	$1.579 \times 10^{-4}$	$0.878 \times 10^{-6}$	
1.35	818.33(7)	0.0275(1)	$1.53(1) \times 10^{-4}$	$0.73(1) \times 10^{-6}$	23.3
Simulation	819.5	0.0287	$1.70 \times 10^{-4}$	$0.93 \times 10^{-6}$	
1.36	781.9(1)	0.02903(2)	$1.61(1) \times 10^{-4}$	$0.64(1) \times 10^{-6}$	22.5
Simulation	782.7	0.03005	$1.92 \times 10^{-4}$	1.06	
1.37	742.10(3)	0.03064(2)	$1.91(1) \times 10^{-4}$	$0.95(3) \times 10^{-6}$	22.5
Simulation	744.7	0.03145	$2.15 \times 10^{-5}$	$1.32 \times 10^{-6}$	
1.38	700.8(1)	0.034(1)	$2.8(1) \times 10^{-4}$	$-0.7(1.3) \times 10^{-6}$	22.2
Simulation	703.6	0.0333	$2.45 \times 10^{-4}$	$1.4 \times 10^{-6}$	
1.39	661.4(9) <sup>†</sup>	0.036(1)	$2(1) \times 10^{-4}$	$1(4) \times 10^{-6}$	23.4
Simulation	661.9	0.0354	$2.8 \times 10^{-4}$	$1.7 \times 10^{-6}$	

<sup>†</sup> At this wavelength, the input and output OMF pigtails are not single-mode any more (see Tab. 3.1), therefore the spectra are very noisy.



# Bibliography

1. Wiedemann, U., Karapetyan, K., Dan, C., Pritzkau, D., Alt, W., Irsen, S. & Meschede, D. Measurement of submicrometre diameters of tapered optical fibres using harmonic generation. *Optics Express* **18**, 7693 (2010).
2. Karapetyan, K., Alt, W. & Meschede, D. *Optical fibre toolbox for Matlab, version 2.1* [[www.mathworks.com/matlabcentral/fileexchange/27819](http://www.mathworks.com/matlabcentral/fileexchange/27819)] (2011).
3. Garcia-Fernandez, R., Alt, W., Bruse, F., Dan, C., Karapetyan, K., Rehband, O., Stiebeiner, A., Wiedemann, U., Meschede, D. & Rauschenbeutel, A. Optical nanofibers and spectroscopy. *Appl. Phys. B* **105**, 3–15 (2011).
4. Kimura, T., Nambu, Y., Hatanaka, T., Tomita, A., Kosaka, H. & Nakamura, K. Single-photon Interference over 150 km Transmission Using Silica-based Integrated-optic Interferometers for Quantum Cryptography. *Japanese Journal of Applied Physics* **43**, L1217–L1219 (2004).
5. Fischer, J., Ergin, T. & Wegener, M. Three-dimensional polarization-independent visible-frequency carpet invisibility cloak. *Optics Letters* **36**, 2059 (2011).
6. Van Heel, A. C. S. A New Method of transporting Optical Images without Aberrations. *Nature* **173**, 39 (1954).
7. Kao, K. & Hockham, G. Dielectric-fibre surface waveguides for optical frequencies. *Proceedings IEE* **133**, 1151 (1966).
8. Ozeki, T. & Kawasaki, B. S. Optical directional coupler using tapered sections in multimode fibers. *Applied Physics Letters* **28**, 528 (1976).
9. Brambilla, G., Finazzi, V. & Richardson, D. J. Ultra-low-loss optical fiber nanotapers. *Optics Express* **12**, 2258 (2004).
10. Grubsky, V. & Savchenko, A. Glass micro-fibers for efficient third harmonic generation. *Optics Express* **13**, 6798 (2005).
11. Leon-Saval, S., Birks, T., Wadsworth, W., St J Russell, P. & Mason, M. Supercontinuum generation in submicron fibre waveguides. *Optics Express* **12**, 2864–9 (2004).
12. Gattass, R. R., Svacha, G. T., Tong, L. & Mazur, E. Supercontinuum generation in submicrometer diameter silica fibers. *Optics Express* **14**, 9408 (2006).

13. Paschotta, R. *Tapered Fibers* [[http://www.rp-photonics.com/tapered\\_fibers.html](http://www.rp-photonics.com/tapered_fibers.html)] (visited on 06/25/2012).
14. Brambilla, G., Xu, F., Horak, P., Jung, Y., Koizumi, F., Sessions, N. P., Koukharenko, E., Feng, X., Murugan, G. S., Wilkinson, J. S. & Richardson, D. J. Optical fiber nanowires and microwires: fabrication and applications. *Advances in Optics and Photonics* **1**, 107 (2009).
15. Nayak, K. P., Melentiev, P. N., Morinaga, M., Kien, F. L., Balykin, V. I. & Hakuta, K. Optical nanofiber as an efficient tool for manipulating and probing atomic Fluorescence. *Optics Express* **15**, 5431 (2007).
16. Sagué, G., Vetsch, E., Alt, W., Meschede, D. & Rauschenbeutel, A. Cold-Atom Physics Using Ultrathin Optical Fibers: Light-Induced Dipole Forces and Surface Interactions. *Physical Review Letters* **99**, 1–4 (2007).
17. Warken, F., Vetsch, E., Meschede, D., Sokolowski, M. & Rauschenbeutel, a. Ultra-sensitive surface absorption spectroscopy using sub-wavelength diameter optical fibers. *Optics Express* **15**, 11952 (2007).
18. Lou, J., Tong, L. & Ye, Z. Modeling of silica nanowires for optical sensing. *Optics Express* **13**, 2135–2140 (2005).
19. Li, Y. & Tong, L. Mach-Zehnder interferometers assembled with optical microfibers or nanofibers. *Optics Letters* **33**, 303–305 (2008).
20. Lacroix, S., Gonthier, F., Black, R. J. & Bures, J. Tapered-fiber interferometric wavelength response: the achromatic fringe. *Optics Letters* **13**, 395 (1988).
21. Villatoro, J., Minkovich, V. & Monzón-Hernández, D. Compact modal interferometer built with tapered microstructured optical fiber. *Photonics Technology Letters, IEEE* **18**, 1258–1260 (2006).
22. Jung, Y., Brambilla, G. & Richardson, D. J. Polarization-maintaining optical microfiber. *Optics Letters* **35**, 2034 (2010).
23. Li, J., Sun, L.-P., Gao, S., Quan, Z., Chang, Y.-L., Ran, Y., Jin, L. & Guan, B.-O. Ultrasensitive refractive-index sensors based on rectangular silica microfibers. *Optics Letters* **36**, 3593 (2011).
24. *Private communication with John Wooler, Fibercore Ltd.: Refractive index of SM800* (2009).
25. Love, J. D., Henry, W. M., Stewart, W. J., Black, R. J., Lacroix, S. & Gonthier, F. Tapered single-mode fibres and devices. I. Adiabaticity criteria. *IEE Proceedings J.* **138**, 343–354 (1991).
26. Warken, F. *Ultradünne Glasfasern als Werkzeug zur Kopplung von Licht und Materie* PhD thesis (2007).
27. Bures, J. *Guided Optics: Optical Fibers and All-fiber Components* 368 (2008).

28. Paschotta, R. *V-number* [[http://www.rp-photonics.com/v\\_number.html](http://www.rp-photonics.com/v_number.html)] (visited on 06/24/2012).
29. Black, R. J., Lacroix, S., Gonthier, F. & Love, J. Tapered single-mode fibres and devices. Pt. 2: experimental and theoretical quantification. *IEE Proceedings J.* **138**, 355–364 (1991).
30. Snyder, A. & Love, J. *Optical waveguide theory* (Chapman & Hall, London, 1983).
31. Yariv, A. & Yeh, P. *Photonics: Optical Electronics in Modern Communications* 836 (2007).
32. Fibercore Ltd. *Singlemode Optical Fiber* [<http://www.fibercore.com/Products/SMSeries/tabid/89/agentType/View/PropertyID/259/Default.aspx>] (visited on 08/23/2011).
33. Yariv, A. *Optical Electronics in Modern Communications* 5th, 768 (Oxford University Press, USA, 1997).
34. *Private communication with Peter Horak* (2009).
35. *Private communication with Limin Tong* (2011).
36. *Private communication with Gilberto Brambilla* (2009).
37. Belanov, A. S., Dianov, E. M., Ezhov, G. I. & Prokhorov, A. M. Propagation of normal modes in multilayer optical waveguides I. Component fields and dispersion characteristics. *Soviet Journal of Quantum Electronics* **6**, 43–50 (1976).
38. Monerie, M. Propagation in doubly clad single-mode fibers. *IEEE Journal of Quantum Electronics* **18**, 535–542 (1982).
39. Tsao, C., Payne, D. & Gambling, W. Modal characteristics of three-layered optical fiber waveguides: a modified approach. *Journal of the Optical Society of America A* **6**, 555–563 (1989).
40. Henry, W. M. An investigation of coated tapered optical fibres. *Sensors and Actuators B: Chemical* **22**, 101–107 (1994).
41. Erdogan, T. Cladding-mode resonances in short- and long-period fiber grating filters. *Journal of the Optical Society of America A* **14**, 1760 (1997).
42. Erdogan, T. Cladding-mode resonances in short- and long-period fiber grating filters: errata. *Journal of the Optical Society of America A* **17**, 2113 (2000).
43. Zhang, Z.-j. & Shi, W.-k. Eigenvalue and field equations of three-layered uniaxial fibers and their applications to the characteristics of long-period fiber gratings with applied axial strain. *Journal of the Optical Society of America A* **22**, 2516 (2005).

44. Linslal, C. L., S. Mohan, P. M., Halder, a. & Gangopadhyay, T. K. Eigenvalue equation and core-mode cutoff of weakly guiding tapered fiber as three layer optical waveguide and used as biochemical sensor. *Applied Optics* **51**, 3445 (2012).
45. *Private communication with Timothy Lee* (2010).
46. *Private communication with David Payne* (2011).
47. Love, J. & Henry, W. Quantifying loss minimisation in single-mode fibre tapers. *Electronics Letters* **22**, 912 (1986).
48. Agrawal, G. P. *Nonlinear Fiber Optics* 3rd, 467 (Academic Press, 2001).
49. Terhune, R. W. & Weinberger, D. a. Second-harmonic generation in fibers. *Journal of the Optical Society of America B* **4**, 661 (1987).
50. Simmons, J. H. & Potter, K. S. *Optical materials* (2000).
51. Liao, C., Wang, D., He, X. & Yang, M. in *Proceedings of SPIE* **23** (2011), 77534I–77534I–4. doi:10.1117/12.885826.
52. Bertholds, A & Dändliker, R. High-resolution photoelastic pressure sensor using low-birefringence fiber. *Applied Optics* **25**, 340 (1986).
53. Bamber, M. J., Cooke, K. E., Mann, A. B. & Derby, B. Accurate determination of Young's modulus and Poisson's ratio of thin films by a combination of acoustic microscopy and nanoindentation. *Thin Solid Films* **399**, 299–305 (2001).
54. Gianino, P. D. & Bendow, B. Calculations of stress-induced changes in the transverse refractive-index profile of optical fibers. *Applied Optics* **20**, 430 (1981).
55. Hocker, G. B. Fiber-optic sensing of pressure and temperature. *Applied Optics* **18**, 1445 (1979).
56. Butter, C. D. & Hocker, G. B. Fiber optics strain gauge. *Applied Optics* **17**, 2867 (1978).
57. Tonning, A. Circularly Symmetric Optical Waveguide with Strong Anisotropy. *IEEE Transactions on Microwave Theory and Techniques* **30**, 790–794 (1982).
58. Stiebeiner, A, Garcia-Fernandez, R. & Rauschenbeutel, A. Design and optimization of broadband tapered optical fibers with a nanofiber waist. *Optics Express* **18**, 22677–22685 (2010).
59. Karapetyan, K., Wiedemann, U., Bruse, F., Alt, W., Pritzkau, D., Dan, C. & Meschede, D. *Optical fibre toolbox for Matlab and Octave* [<http://www.mathworks.com/matlabcentral/fileexchange/27819>] (2010).
60. Boys, C. V. On the Production, Properties, and some suggested Uses of the Finest Threads. *Proceedings of the Physical Society of London* **9**, 8–19 (1887).

61. Threlfall, R. *On laboratory arts* (MACMILLAN and CO., LTD., 1898).
62. Cassidy, D. T., Johnson, D. C. & Hill, K. O. Wavelength-dependent transmission of monomode optical fiber tapers. *Applied Optics* **24**, 945 (1985).
63. Gonthier, F., Lapierre, J., Veilleux, C., Lacroix, S. & Bures, J. Investigation of power oscillations along tapered monomode fibers. *Applied Optics* **26**, 444 (1987).
64. Bilodeau, F., Hill, K., Faucher, S. & Johnson, D. Low-loss highly overcoupled fused couplers: fabrication and sensitivity to external pressure. *Journal of Lightwave Technology* **6**, 1476–1482 (1988).
65. Kenny, R., Birks, T. & Oakley, K. Control of optical fibre taper shape. *Electronics Letters* **27**, 1654 (1991).
66. Birks, T. A. & Li, Y. W. The shape of fiber tapers. *Journal of Lightwave Technology* **10**, 432–438 (1992).
67. Tong, L., Gattass, R. R., Ashcom, J. B., He, S., Lou, J., Shen, M., Maxwell, I. & Mazur, E. Subwavelength-diameter silica wires for low-loss optical wave guiding. *Nature* **426**, 816–819 (2003).
68. Lamont, R. G., Hill, K. O. & Johnson, D. C. Tuned-port twin biconical-taper fiber splitters: fabrication from dissimilar low-mode-number fibers. *Optics Letters* **10**, 46 (1985).
69. Sorin, W., Jackson, K. & Shaw, H. Evanescent amplification in a single-mode optical fibre. *Electronics Letters* **19**, 820 (1983).
70. Henry, W. Evanescent field devices: a comparison between tapered optical fibres and polished or D-fibres. *Optical and Quantum Electronics* **26**, S261–S272 (1994).
71. Corning Inc. *Corning SMF-28 ULL Optical Fiber* 1–2 (2011).
72. Corning Inc. *Corning SMF-28e+ Photonic Optical Fiber* 1–4 (2010).
73. Stiebeiner, A., Garcia-Fernandez, R. & Rauschenbeutel, A. Design and optimization of broadband tapered optical fibers with a nanofiber waist. *Optics Express* **18**, 22677–22685 (2010).
74. Pritzkau, D. *Measurement of submicrometer diameters of tapered optical fibres using scanning electron microscopy*. Diplom thesis (2010).
75. Paschotta, R. *Titanium-sapphire lasers* [[http://www.rp-photonics.com/titanium\\_sapphire\\_lasers.html](http://www.rp-photonics.com/titanium_sapphire_lasers.html)] (visited on 05/19/2012).
76. Lee, T., Jung, Y., Codemard, C. A., Ding, M., Broderick, N. G. R. & Brambilla, G. Broadband third harmonic generation in tapered silica fibres. *Optics Express* **20**, 8503 (2012).
77. Paek, U. High-speed high-strength fiber drawing. *Journal of Lightwave Technology* **4**, 1048–1060 (1986).

78. Wei, Z., Lee, K.-M., Tchikanda, S. W., Zhou, Z. & Hong, S.-P. Free Surface Flow in High Speed Fiber Drawing With Large-Diameter Glass Preforms. *Journal of Heat Transfer* **126**, 713 (2004).
79. Smithgall, D. H., Watkins, L. S. & Frazee, Jr., R. E. High-speed noncontact fiber-diameter measurement using forward light scattering. *Applied Optics* **16**, 2395 (1977).
80. Kerker, M. & Matijevic, E. Scattering of Electromagnetic Waves from Concentric Infinite Cylinders. *Journal of the Optical Society of America* **51**, 506 (1961).
81. Matijevic, E., Ottewill, R. H. & Kerker, M. Light Scattering by Infinite Cylinders Spider Fibers. *Journal of the Optical Society of America* **51**, 115 (1961).
82. Rayleigh, L. XLI. The dispersal of light by a dielectric cylinder. *Philosophical Magazine Series 6* **36**, 365–376 (1918).
83. Van de Hulst, H. C. *Light scattering by small particles* **360**, 470. doi:10.1002/qj.49708436025 (John Wiley & Sons, London, 1957).
84. Kozaki, S. Scattering of a Gaussian beam by a homogeneous dielectric cylinder. *Journal of Applied Physics* **53**, 7195 (1982).
85. Abushagur, M. A. G. & George, N. Polarization and wavelength effects on the scattering from dielectric cylinders. *Applied Optics* **24**, 4141 (1985).
86. Watkins, L. S. Scattering from side-illuminated clad glass fibers for determination of fiber parameters. *Journal of the Optical Society of America* **64**, 767 (1974).
87. Zimmermann, E., Dändliker, R., Souli, N. & Krattiger, B. Scattering of an off-axis Gaussian beam by a dielectric cylinder compared with a rigorous electromagnetic approach. *Journal of the Optical Society of America A* **12**, 398 (1995).
88. Warken, F. & Giessen, H. Fast profile measurement of micrometer-sized tapered fibers with better than 50-nm accuracy. *Optics Letters* **29**, 1727 (2004).
89. Butler, D. J. & Forbes, G. W. Fiber-Diameter Measurement by Occlusion of a Gaussian Beam. *Applied Optics* **37**, 2598 (1998).
90. Brambilla, G., Xu, F., Horak, P., Jung, Y., Koizumi, F., Sessions, N. P., Koukharenko, E., Feng, X., Murugan, G. S., Wilkinson, J. S. & Richardson, D. J. Optical fiber nanowires and microwires: fabrication and applications. *Advances in Optics and Photonics* **1**, 107 (2009).
91. Bruse, F. *Harmonic Generation with Optical Microfibres under Controlled Atmospheres*. Diplom thesis Diplomarbeit (Bonn, 2011), 653.
92. Wiedemann, U. *Nonlinear optics and molecules with microfibres* PhD thesis (2011).

93. Hartung, J. *Optical microfibre surface protection for caesium spectroscopy* MSc thesis (2012).
94. Karapetyan, K. *Matlab toolbox for Avantes data files processing* [<http://www.mathworks.com/matlabcentral/fileexchange/37103>] (2011).
95. Mathworks. *Matlab fminsearch function* [<http://www.mathworks.com/help/techdoc/ref/fminsearch.html>] (2012).
96. Lagarias, J. C., Reeds, J. A., Wright, M. H. & Wright, P. E. Convergence Properties of the Nelder–Mead Simplex Method in Low Dimensions. *SIAM Journal on Optimization* **9**, 112 (1998).
97. Cargille refractive index liquids [<http://www.cargille.com/refractivestandards.shtml>] (visited on 06/19/2012).
98. Xu, F., Brambilla, G. & Lu, Y. A microfluidic refractometric sensor based on gratings in optical fibre microwires. *Optics Express* **17**, 20866–71 (2009).
99. Wang, P., Brambilla, G., Ding, M., Semenova, Y., Wu, Q. & Farrell, G. High-sensitivity, evanescent field refractometric sensor based on a tapered, multimode fiber interference. *Optics Letters* **36**, 2233 (2011).
100. Yang, J., Jiang, L., Wang, S., Li, B., Wang, M., Xiao, H., Lu, Y. & Tsai, H. High sensitivity of taper-based Mach–Zehnder interferometer embedded in a thinned optical fiber for refractive index sensing. *Applied Optics* **50**, 5503 (2011).
101. Birks, T. A., Knight, J. & Dimmick, T. High-resolution measurement of the fiber diameter variations using whispering gallery modes and no optical alignment. *IEEE Photonics Technology Letters* **12**, 182–183 (2000).
102. Bigio, L. Density measurements of Hg(63P0,1,2) in a discharge using saturated laser absorption and hook methods. *Journal of Applied Physics* **63**, 5259 (1988).
103. Hendrickson, S. M., Pittman, T. B. & Franson, J. D. Nonlinear transmission through a tapered fiber in rubidium vapor. *Journal of the Optical Society of America B* **26**, 267 (2009).
104. Boyd, R. *Nonlinear optics* (Academic Press, 1992).
105. Mathworks. *Matlab fzero function* [<http://www.mathworks.de/help/techdoc/ref/fzero.html>] (2011).